University of Bath

PHD

Investigation of High Temperature Superconducting Components for Fully Superconducting Machine

Xing, Dong

Award date:
2020

Awarding institution:
University of Bath

Link to publication

Alternative formats

If you require this document in an alternative format, please contact:
openaccess@bath.ac.uk

Investigation of High Temperature Superconducting Components for Fully Superconducting Machine

Dong Xing

A thesis submitted for the degree of Doctor of Philosophy (PhD)

Department of Electrical and Electronic Engineering

University of Bath

2020

COPYRIGHT

Signature_____   Date_____

Acknowledgement

First of all, I would like to express my gratitude to my supervisor Dr. Min Zhang for her meticulous guidance during my entire PhD study. She has allowed me to explore the research independently, and always being kind to help me to solve tough problems. Without her expert advice and dedicated support, I will not be able to persist my study in a proper way. I would like to thank Dr. Xiaoze Pei for her continuous assistance. She always gives me constructive criticism of my research and is willing to advise me the better way to write a good paper or thesis. I would also like to appreciate Prof. Weijia Yuan for giving me lots of learning guidance on superconductivity.

I am grateful to Dr. Huiming Zhang and Dr. Yawei Wang for providing modelling guidance and valuable discussions on modification of simulation work, Dr. Zhenyu Zhang and Dr. Jie Sheng for giving me experimental support and technical guidance. I want to thank my colleagues and friends in the applied superconductivity group in the department of electrical and electronic engineering at the University of Bath, in no particular order, Dr. Fei Liang, Dr. Jianwei Li, Dr. Xiaojian Li, Mariam Elshiekh, Hamoud Alafnan, Zixuan Zhu, Muhammad Zulfiqar Ali, Sriharsha Venuturumilli, Fangjing Weng, Zhidun Zeng, Jiawen Xi, Boyuan Yin and Monis. The friendship and encouragement have been the most enjoyable and cherished time during my PhD study. I also appreciate Dr. Difan Zhou from the University of Cambridge for his experimental support on pulse-field magnetisation.

Last but not the least, I would like to express my gratitude and love to my families, especially my husband Dr. Qixing Sun. Their support drives me to work hard. Their love gives me the courage to overcome the challenges met during the research. Without them I would never experience such invaluable experience in the entire PhD study.

II

Abstract

The development of various technologies in recent years provides confidence in the ability to create new-generation electric power applications such as full superconducting electric machines. High temperature superconductor (HTS) bulks or stacks of coated conductors (CCs) have emerged as a promising technology to provide extremely strong magnetic fields by trapping persistent currents. HTS coils are great candidates for higher current capacity and lower losses. They can enable more efficient devices with compact volumes and higher energy efficiencies. A prototype machine has been previously created showing that trapped field magnets and coils have superb benefits to be used as field poles on the rotor and as the armature windings of a motor/generator, respectively, for HTS rotating electric machines.

The key issues for the practical application of such HTS stacks or coils in HTS rotating electric machines are providing high trapped field magnets using in-situ magnetisation methods and mitigating the production of alternating current (AC) losses. Pulsed field magnetisation (PFM) is an efficient method to activate and magnetise HTS stacks using pulses in the order of milliseconds with relatively reduced size and expense of facilities. However, the heat generated during the dynamic process limits the trapped field of stacks. Furthermore, using HTS armature windings in time-varying currents and/or magnetic fields gives rise to unavoidable AC losses on account of the movement of magnetic flux vortices in the superconducting material.

This thesis focuses on investigating the magnetic flux dynamics during PFM especially for trapped field magnets (TFMs) of stacks, and the interpretation of AC losses mitigation methods. Both TFM and AC losses will be analysed using numerical simulations and experimental work.

The original achievements of this research and which are presented in this thesis can be summarised as follows:

1. Modelling finite element models (FEMs) in 2D with realistic laminated structures using *H*-formulation and *T-A* formulation. The models of stacks (with and without magnetic substrates) based on commercially available HTS tape were magnetised by PFM in simulations by coupling an electromagnetic model and a thermal model, which were validated by experiments. The results of the *H*-formulation and *T-A* formulation models using zero field cooling (ZFC) magnetisation methods were also compared.

2. Exploring a time-saving 2D thermal-coupled model using *T-A* formulation for laminated-structure model, which is compared with a previous *H*-formulation model in respect to the distribution of magnetic field, current density and temperature variation in different material layers.

3. Effects of related simulated parameters, magnetism and thicknesses of corresponding substrates on the trapped fields of stacks with and without magnetic substrates were analysed for better HTS tape selection.

4. Experimental validation comparing stacks with and without magnetic substrates was completed using vortex-type PFM. The PFM for stacks with different ramp-down times was tested and the results were compared. The PFM involved with temperature monitoring and sensor arrays for a stack with a magnetic substrate was achieved, which helped to comprehend and confirm the thermal-effect magnetisation and magnetic field distribution.

5. Striated (multifilament) and non-striated superconducting coils were wound. Testing and comparing the critical current and transport AC losses of striated and non-striated coils using both experimental and simulated methods was successfully achieved.

Publication

1. D. Xing, J. Patel, Q. Sun, J. Zhu, G. Zhang, F. Liang, W. Yuan, and M. Zhang, "AC loss comparison between multifilament and nonstriated YBCO coils designed for HTS propulsion motors". IEEE Transactions on Applied Superconductivity, vol. 27, no. 4, pp. 1-5, 2017.

2. Q. Sun, D. Xing, Q. Yang, H. Zhang, and J. Patel, "A new design of fuzzy logic control for SMES and battery hybrid storage system," Energy Procedia, vol. 105, pp. 4575-4580, 2017.

3. Z. Zhu, Y. Wang, D. Xing, X. Pei, M. Zhang, and W. Yuan, "Quench of a single-layer ReBCO CORC cable with non-uniform terminal contact resistance," IEEE Transactions on Applied Superconductivity, vol. 29, no. 5, pp. 1-5, 2019.

4. Q. Sun, D. Xing, H. Alafnan, X. Pei, M. Zhang, and W. Yuan, "Design and test of a new two-stage control scheme for SMES-battery hybrid energy storage systems for microgrid applications," Applied Energy, vol. 253, p. 113529, 2019.

Contents

X

List of figures

XVI

List of tables

xx

List of symbols

Symbol	Description
a	Half thickness of slab
A	Magnetic vector potential
A_e	Armature electric loading
b	Parameter related with α
B	Magnetic flux density
B_a	Amplitude of the applied external magnetic flux density
B_{air}	Peak airgap magnetic flux density
B_{app}	An exponential equation related with magnetic flux density
B_p	Complete penetrated magnetic flux density
B_0	Characteristic magnetic flux density which relies on the material
$B_\perp$	Magnetic flux density perpendicular to the flat surface of the superconducting tape
$B_\parallel$	Magnetic flux density parallel to the flat surface of the superconducting tape
$B(r)$	Magnetic flux density at the interface between the normal and superconducting regions
c	Parameter related with α
C_p	Heat capacity
C_{pm}	Heat capacity of the corresponding substrate or stabiliser layer
C_{ps}	Heat capacity of the YBCO layer
d_0	Parameter dependent on the physical microstructure of the material
d_s	Real thickness of YBCO layer, $1\mu m$
E	Electric field
E_0	Critical electric field, $1\mathrm{e}^{-4}\ V/m$

E_x	Electric field in the x direction
E_y	Electric field in the y direction
E_z	Electric field in the z direction
E_θ	Electric field in the azimuthal direction in the cylindrical coordinate system
f	Frequency
H	Magnetic field
H_a	Amplitude of the applied external magnetic field
H_c	Critical magnetic field for a type-I superconductor
H_{c1}	Lower critical magnetic field in a type-II superconductor
H_{c2}	Higher critical magnetic field in a type-II superconductor
H_m	Maximum applied magnetic fields
H_p	Penetration field
H_r	Magnetic field in the r direction
H_x	Magnetic field in the x direction
H_y	Magnetic field in the y direction
H_z	Magnetic field in the z direction
H_0	Magnetic field at equilibrium temperature
h	Vertical undulation range of each strand (total height of the cable)
I	Transport current or total current flowing in the superconductor tape
I_c	Critical current
I_m	Current flowing in metallic layers
I_{rms}	RMS current
I_{su}	Current flowing in the superconducting layer
J	Current density
J_c	Critical current density
J_{c0}	Critical current density under a self field
J_{norm}	Normalized current density
J_x	Current density in the x direction
J_y	Current density in the y direction
J_z	Current density in the z direction
J_θ	Critical current in the azimuthal direction in the cylindrical coordinate system
k	Thermal conductivity
k_m	Thermal conductivity of the corresponding substrate or stabiliser layer

k_s	Thermal conductivity of the YBCO layer
k_0	Anisotropy parameter
L	Length between two voltage taps
l_t	Transposition length
l_f	Length of flat straight section
M	Volume average of the local magnetisation
M_{sat}	Saturation magnetisation
N	Total turns
n	Characteristic parameter named as n value for E-J power law
$\vec{n}$	Normal vector of the domain
n_{c0}	Power index in self field
$n_s(r)$	Superconducting electron density at the interface between the normal and superconducting regions
P	Output electrical power of a rotating device
Q	Power density dissipated by the heat source
Q_{m0}	Power density dissipated by the heat source of the corresponding substrate or stabiliser layer
Q_s	Power density dissipated by the heat source of the YBCO layer
Q_m	AC magnetisation loss
Q_t	AC transport loss
Q_{total}	Total AC loss
r	Radius of a circular cross-section
R_m	Resistance of the metallic layers
R_{su}	Resistance of the superconducting layer
S	Cross section of a single turn

T	Current vector potential or temperature depends on the equation
T_0	Critical temperature under a self field
T_1	Values of T on the left edge
T_2	Values of T on the right edge
T_c	Critical temperature at $B = 0$
T_t	Torque
t	Time
V	Volume enclosed by the airgap
V_k	Voltage of kth stand
V_{mean}	Mean value of voltage
V_{rms}	RMS voltage
w	Half height of slab
w_1	Strand width of straight section
w_2	Strand width of transposition section
w_g	Gap width between strands
x_p	Penetration depth
μ	Permeability
μ_0	Vacuum permeability
μ_r	Relative permeability
λ	Penetration depth
ξ	Coherence length
κ	Ginzburg–Landau parameter
α	Parameter related with the temperature

β Parameters to determine the rapidity of the J_c reduction with the magnetic field

τ Appropriate value for the rise time of the pulse

ω Rotational speed

ρ Density

ρ_m Density of the corresponding substrate or stabiliser layer

$\rho_{metallic}$ Resistivity of the metallic layers

ρ_{copper} Resistivity of the copper stabiliser

List of abbreviations

AC	Alternating current
AMSC	American Superconductor Corporation, MA, USA
BSCCO	Bismuth strontium calcium copper oxide (BiSrCaCuO)
CC	Coated conductor
CMDC	Controlled magnetic density distribution coil
COP	Coefficient of Performance
CSM	Critical state model
DC	Direct current
FEM	Finite element method
FeSC	Iron-based superconductor
FC	Field cooling
FCL	Fault current limiter
GdBCO	Gadolinium barium copper oxide (GdBaCuO)
Gd-123	Melt-growth GdBCO (GdBa$_2$Cu$_3$O$_y$)
HTS	High temperature superconductor
IMRA	Iteratively magnetizing pulsed-field method with reducing amplitude

LaBaCuO	Lanthanum-barium-copper oxide ceramic
LSCO	Lanthanum strontium copper oxide ($La_{2-x}Sr_xCu O_2$)
LTS	Low temperature superconductor
MgB_2	Magnesium diboride
MPSC	Multi-pulse technique with step-wise cooling
MMPSC	Modified multi-pulse technique with step-wise cooling
MRI	Magnetic resonance imaging
Nb_3Sn	Niobium–tin
NbTi	Niobium-titanium
Ni5W	Ni–5at%W alloy
NMR	Nuclear magnetic resonance
PDE	Partial differential equation
PFM	Pulsed field magnetisation
ReBCO	Rare-earth barium copper oxide materials ((RE)BaCuO)
SMES	Superconducting electromagnetic energy storage
SPA	Successive pulsed-field application
TFM	Trapped field magnet
TSMG	Top-seeded melt growth
YBCO	Yttrium barium copper oxide ($YBa_2Cu_3O_{7-\delta}$)
ZFC	Zero-field cooling
1G	First generation
2G	Second generation
2D	Two-dimensional space
3D	Three-dimensional space

Chapter 1   Introduction

1.1 Background

In 1911, a breakthrough was discovered by Heike Kamerlingh Onnes who observed a remarkable phenomenon that the resistance abruptly dropped to approximately zero when he was studying the resistance of solid mercury at 4.2 K using the recently developed helium liquefaction technique. His phenomenal work on a low temperature superconductor resulted in him being awarded the Nobel Prize in Physics in 1913. Following Onnes's work, Meissner and Robert Ochsenfeld discovered in 1933 that superconductors can expel applied magnetic fields, which is known as the "Meissner effect" [1]. Two years later, Fritz and Heinz London showed that the Meissner effect was a consequence of the minimisation of the electromagnetic free energy carried by superconducting current. According to London's equation, there is an exponential decline between the magnetic field and current density with distance x from the surface. It exists only in the thin outer layer of the superconductor with penetrated depth λ. When $x > 5\lambda$, either the magnetic field or current density decreases almost to zero [2, 3]. Since then, abundant theory about superconductivity has been produced, such as Ginzburg-Landau theory [4] and BCS (Bardeen-Cooper-Schrieffer) theory [5], which has increased our awareness and understanding of superconductivity.

Owing to the lower critical magnetic field and limitation of temperature, the growth in the application of superconductors is slow. In 1957, the theoretical paper published by Alexei Alexeyevich Abrikosov accelerate the development of type-II superconductors which have the features of carrying larger current and withstanding higher magnetic fields in comparison with type-I superconductors [6]. Later on, practical low temperature superconductor (LTS) wires and subsequently magnets were then developed. Many years of exploration have been devoted to the development of superconducting materials. The discovery of superconductivity in ceramic materials was found by Muller and Bednorz, who were awarded the Nobel Prize in 1987. It was realised that liquid nitrogen could be used as a refrigerant to keep the temperature

at 77 K. Later on, a great evolution was experienced in the superconductivity industry with the discovery of high-temperature superconductors (HTS). The first generation (1G) HTS material was bismuth strontium calcium copper oxide (BSCCO), which was explored in the early 1990s. It is a good candidate for making superconducting wires. However, the high cost of silver used in its manufacture and lower working temperature urged the development of a second generation (2G) HTS, one of which is made of yttrium barium copper oxide (YBCO). Magnesium diboride (MgB_2) conductors are also being fabricated and applied in low field applications due to its relatively simple structure, isotropic magnetic property, lower cost of cryogen (liquid H_2) and materials. Nevertheless, MgB_2 conductor's current-carrying capacity is still lower than other HTS materials. The thesis pays more emphasis on 2G YBCO tapes.

2G HTS were commercially produced in the early 2000s. Coated conductors (CCs) have become more appealing among commercial HTS wires and tapes. There are plenty of manufacturers developing 2G wire worldwide. Two significant sources for the 2G wire are American Superconductor (AMSC) and SuperPower. The MOD/RABiTS process and IBAD - MgO process are two most common manufacturing processes in practice, which are selected by AMSC and SuperPower, respectively. The architecture of 2G wire is quite different for different manufacturers. "MOD/RABiTS" is the abbreviation of "metal organic deposition (MOD)/rolling assisted biaxially textured substrate (RABiTS)". The lamination of AMSC wire consists of 2G tape sandwiched between thin copper and stainless steel tapes. It also includes a flexible substrate which is nonmagnetic or weakly magnetic metal, typically 50 - μm thick. There is a typically 0.5 - μm thick multifunctional oxide barrier or buffer layer above the substrate as well [7, 8]. As for SuperPower, they adopted the ion beam assisted deposition (IBAD) process for manufacturing 2G conductors and transferred from low - throughput IBAD - YSZ (Yttria – stabilized zirconia) technology to high - throughput IBAD - MgO technology. There are various widths (e.g. 3, 4, 6 and 12 mm), substrate thickness, silver and copper stabilizer thickness, as well as optional insulation of 2G wires in SuperPower market. The stabilizers protects the conductor and produces rounded edges which is beneficial in high - voltage applications [8, 9].

The current carrying capacity and mechanical performance of 2G HTS CCs has grown a lot compared with 1G HTS. Applications of 2G HTS CCs has developed rapidly in recent years. There are plenty of potential markets for HTS CCs in the electric power arena including the high-power industry, ship propulsion motors, full electric aircraft, utility generators, synchronous condensers and wind power plants. With the ability to manufacture longer lengths

of 2G HTS (available since 2005), it has been achievable to use superconductors in power transmission cables [10], transformers [8], large electrical magnets [11], electric machines (motors and generators) [12], superconducting electromagnetic energy storage (SMES) systems [13], and fault current limiters (FCLs) [14], etc.

1.2 Research motivation and challenges

Traditional rotating machines adopt copper windings on rotor and stator. As current flows in these windings, resistive losses will appear, which increase the burden of energy as well as economic resources. As for superconductor-based electric machines, superconductivity represents zero to near - zero resistance features to current flow. Therefore, there is a reduction of energy loss as well as size and weight of power components and apparatus [8]. Fully superconducting rotating electric machines using HTS under direct current (DC) and AC conditions have been a continued, promising topic of research. They utilise the advantages of high magnetic field, high electric loading, reduced weight, high efficiency and high torque density. The elimination of the joule heating resulting from the copper coils and hysteretic and eddy currents losses generated in the ferromagnetic core in conventional machines significantly increases the efficiency of HTS rotating machines. Although there is power needed for the HTS cooling, the enhancement of efficiency can outweigh the waste.

Fully HTS machine protypes have been built in several groups [15-17]. A great number of large-scale projects utilized the excitation of the HTS field windings to build HTS rotating machines. However, compared with HTS windings, the same size of HTS trapped field magnets (TFMs) can trap higher magnetic fluxes, giving rise to persistently higher power densities and reduced size of the rotating machines. HTS TFMs can replace traditional permanent magnets as field poles in the rotor of a superconducting machine to supply constant magnetic flux density, in order to increase power and torque densities. The HTS TFMs are firstly magnetised by excitation coils like copper coils. After magnetisation process, the rotor will be moved into stator for motor operation. As the motor rotates, HTS TFMs create a magnetic field in the armature windings. The magnitude of this field is typically twice that of a conventional motor [8]. The entire rig needs to be immerged into a cooling system to maintain the HTS rotor at cryogenic temperature. For typical HTS TFMs, HTS bulk is suitable to be

used as a permanent magnet after magnetisation since it can sustain a high persistent current and have a large diamagnetic response. The record trapped magnetic field of HTS bulk has been up to 17.6 T at 26 K, which is approximately 10 times more than conventional rare-earth permanent magnets [18]. HTS tapes can be cut and stacked to form composite bulks named 'HTS stacks'. HTS stacks of CCs show great potential for generating magnetic fields as permanent magnets after being activated owing to their ability to maintain magnetic flux. It is a promising TFM technology due to its relatively flexible structure, better mechanical strength compared with HTS bulks. The world record trapped magnetic field for HTS stacks is 17.7 T at 8 K [19]. The metallic stabilisers and substrates contained in HTS tapes provide more stabilisation compared to HTS bulks. It is flexible for HTS tapes to cut and build diverse shapes and configurations. Due to the variety of HTS tapes, the fabrication and composition of stacks are different, which leads to varied trapped field capabilities. The use of exciting coils and magnetisation methods are also significant aspects. The magnetisation procedure should be conducted on HTS stacks in advance of operation in an electric machine. The irreversible magnetisation process of HTS stacks is similar to a ferromagnetic material. Although higher optimal trapped fields can be reached by field cooling (FC) and zero field cooling (ZFC) for a given applied field, the expense of these methods are too high, since huge and expensive exciting coils are required. The pulsed-field magnetisation (PFM) method, which is characterised by reduced weight, high flexibility and lower expense, has more benefits compared to the other types of magnetisation methods.

The inevitable technical challenge for HTS TFMs is that the trapped fields produced by PFM are much lower than those produced by the FC or ZFC method, because the temperature increases greatly during PFM due to fast magnetic flux motion. The emphasis of this research will be stacks of CCs. For a variety of HTS tapes, the performance of HTS stacks trapping magnetic field are not identical, which calls for new measurement techniques, to deeply analyse and improve the trapped field abilities of HTS stacks magnetised by the PFM method.

With the improvement in critical currents and current carrying capacity of HTS conductors, HTS coils have been characterised and tested as AC stator windings [16]. The AC stator windings of an electric machine can be replaced with HTS coils due to their higher current density and lower losses. The field generated by the HTS windings is around 50% stronger compared with a comparable copper winding [16].

The key challenge during the design of HTS stators is the critical current and the prediction of the AC losses of HTS AC windings. The critical current and AC losses determine the current carrying capacity and operating conditions. The requirement of cooling energy of HTS windings correspondingly grows owing to the AC losses. The energy required based on heat generated at a cryogenic temperature is related to Carnot efficiency and practical cryocooler Coefficient of Performance (COP). The COP is the ratio of the heat output of a heat pump to its electrical energy input. As for HTS coils, for instance, it takes approximately 100 watts of input energy to remove one watt of heat from a 20 K environment [20]. Therefore, estimation and measurement of the critical current and AC losses are essential for HTS windings designs. Furthermore, testing, facilities, materials and HTS tapes are also all crucial elements.

The subject analysed in the thesis is the HTS components in the fully HTS machine by using HTS DC permanent magnets, as well as HTS AC armature windings. Higher trapped magnetic fields for HTS TFMs is the main purpose researchers are pursuing in this area. More strategies need to be provided for TFM analysis by means of numerical simulations and experimental validation. Furthermore, the heat dissipation caused by the AC losses and the maximum current carrying capacity of HTS windings are inevitable problems, which also require further analysis. Accurate estimation of the AC losses and their measurement is crucial for HTS windings, to ensure long-lasting operation.

In this research, 2D finite element models were used with realistic laminated structures using both *H*-formulation and *T-A* formulation. Accurate and quick estimation of the distribution of magnetic fields, current density and temperatures of large aspect ratio stacks resulted in an enormous mesh in COMSOL. The computation time for an electromagnetic and thermal coupled model is much longer. Thus, efficient numerical modelling is of vital significance.

1.3 Research purpose and thesis structure

This thesis focuses on the interpretation and improvement of the trapped field ability of HTS stacks and the mitigation of AC losses using multi-filament coils using both numerical and experimental approaches.

The structure of the remainder of the thesis is:

Chapter 2 introduces a review of superconductivity, including basic properties and classifications, relevant critical parameters, critical state models, numerical modelling for analysing electromagnetic behaviour of superconductors and fundamental principles of magnetisation and AC losses.

Chapter 3 provides an introduction to the relevant numerical models in this thesis. It starts by introducing a 2D thermal-coupled *H*-formulation model with the actual structures and material configurations based on commercial HTS tapes. Following this, a 2D electromagnetic-thermal *T-A* formulation model is explored and compared with the *H*-formulation model. Results of trapped fields of stacks with laminated-structure using the ZFC and PFM methods were compared for both of thermal-coupled *H*-formulation and *T-A* formulation models.

Chapter 4 presents the simulation work related to the PFM of HTS stacks. The impact of simulated parameters on the simulation results on the trapped fields of stacks (with and without magnetic substrates) is determined. The effects of magnetic properties and the thicknesses of different substrates on the trapped fields and trapped fluxes are also investigated thoroughly.

Chapter 5 presents the experimental work related to the PFM of HTS stacks (with and without magnetic substrates). Initially, the trapped fields of two 5-layer stacks made from HTS tapes (with and without magnetic substrates) are compared. Then, the effects of pulse duration on the strength of the trapped fields is validated by experiments. Furthermore, single-pulse and multi-pulse magnetisation are achieved for a 20-layer HTS stack with a magnetic substrate. Temperature and trapped field distribution are further validated by experiments.

Chapter 6 investigates the mitigation of the AC losses using multi-filament tape. Experimental work was conducted to investigate the critical current and transport loss of a multi-filament coil and a non-striated coil. The critical current and transport AC loss were also compared in 2D axisymmetric models using *H*-formulation.

Chapter 7 draws a conclusion and summarises the contributions of the thesis and specifies future work.

Chapter 2　Basics of superconductivity

2.1 Introduction of superconductivity

2.1.1 Basic characteristics

2.1.1.1 Zero-resistance characteristic

Superconductivity is widely supposed as zero resistance. It is a phenomenon that the measured voltage of the material suddenly falls to zero when the sample is cooled below its critical temperature. If a current is transported to a superconductor and form a closed loop, the induced "persistent current" could last for several years without obvious decay [3]. The resistivity of a good conventional conductor, for instance copper, is 10^{-10} $\Omega \cdot$m at 4.2 K, which is more than 17 orders of magnitude than that of the superconductor (less than 10^{-27} $\Omega \cdot$m). The comparison of experimental dependence of resistance on temperature in a superconductor and normal conductor is shown in Figure 2.1, in which the resistivity of the superconductor suddenly drops to zero when the temperature reduces to a certain value below the critical temperature T_c [3].
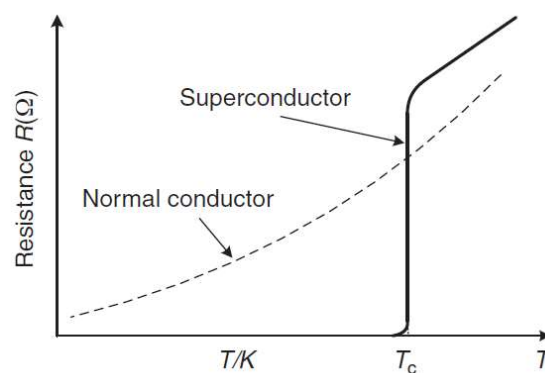
Figure 2.1: Resistance versus temperature curve of superconductors and normal conductors [3].

2.1.1.2 Meissner effect

Although zero-resistance is a straightforward way to describe superconductors, it is not sufficient to explain the superconductivity. The fundamental criterion for superconductivity is the Meissner Effect. The effect was observed by Meissner and Ochsenfeld in 1933 when they cooled a pure tin exposed in the external magnetic field. When the superconductor is in a superconducting state, the magnetic flux is completely expelled from its interior below its superconducting critical temperature, which is so-called ideal diamagnetism. Figure 2.2 (b) presents the situation when the magnetic field within the superconducting material is zero. However, when the superconductor is subjected to a magnetic field after cooling the sample below its critical temperature, the superconductor is in a non-superconducting state. The magnetic field can penetrate the superconductor and the inner magnetic field is not zero in its normal state as shown in Figure 2.2 (a) [3]. It is the so-called ideal conductivity.
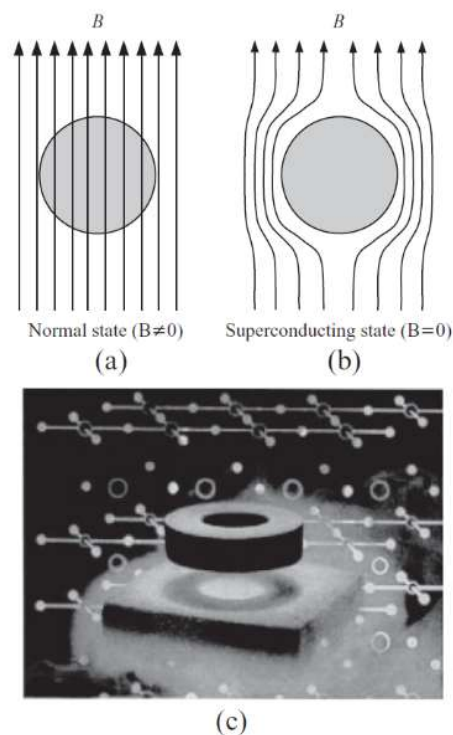
Figure 2.2: Meissner effect (complete diamagnetism) and levitation of superconductor: (a) normal state; (b) Meissner state; (c) YBCO bulk levitation.

According to Lenz's Law, electromotive force (emf) induced in a conductor moving perpendicular to a magnetic field tends to against that motion. A YBCO bulk was put in the presence of a magnetic field produced by conventional permanent magnetic materials (like NdFeB).When the YBCO bulk is in a superconducting state, as shown in Figure 2.2 (c), the current that arises to counter the external change in flux may persist indefinitely. Thus, a superconducting material may act like a strong diamagnet and suspend in the air [21].

2.1.1.3 Critical Parameters

The surrounding physical conditions have a great effect on superconductivity. The critical temperature is the temperature at which the superconductor transfers to a superconducting state from a normal state and is denoted by the critical temperature T_c. On top of the temperature, superconductors can also lose their superconductivity when the magnetic field strength exceeds a certain value in the external magnetic field or the transport current increases above a certain value. The magnetic field strength and current that causes a superconductor to lose its superconductivity are called the critical magnetic field H_c and critical current I_c. In practical applications, current density is widely used than current, so that the corresponding current density is defined as critical current density J_c [3].
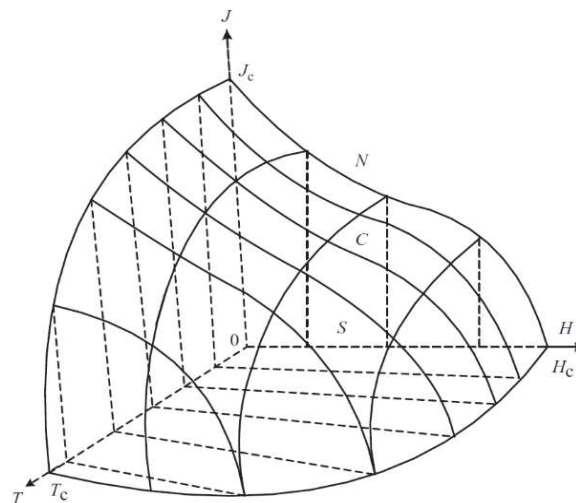
Figure 2.3: Critical parameters and their relationships.

The three basic critical parameters T_c, H_c, and J_c of superconductors are not independent of each other. There is a strong correlation between them. Figure 2.3 shows the relationship

between the three critical parameters. Any point within the volume enclosed by a curved surface (T_c, H_c, J_c) and three planes (T_c, J_c), (J_c, H_c), (H_c, T_c) is in the superconducting state S; any point outside the volume is in the normal state N, and any point on the curved surface with (T_c, H_c, J_c) is at the critical state C [3].

2.1.2 Type-I & type-II superconductors

As mentioned above, the Meissner effect is one of the characteristic features to identify the superconductivity. However, witnessing a rise of the external magnetic field, some superconductors will shift its state from the Meissner state to the normal state and others may change to the mixed state and the normal state, which is the difference between type-I and type-II superconductors as Figure 2.4 shows. The magnetisation versus applied magnetic field is shown in Figure 2.5.

Only one surface boundary of energy occurs in type-I superconductors between the normal and Meissner region in the metal, which is the critical magnetic field H_c. The magnetisation drops suddenly at the critical field $H = H_c$ (Figure 2.5). Silsbee put forward a perspective that the resistance of a superconductor will not remain at zero when the total magnetic field strength exceeds H_c at any point on the surface boundary [22]. The maximum current can pass through the type-I superconductor is given by $I_c = 2\pi r H_c$, where r is the radius of a circular cross-section. And as the current in the superconducting wire is higher than its critical value, the alteration to the normal state is called Silsbee effect [23]. Furthermore, the critical magnetic field is dependent on the temperature: $H_c = H_0 \left(1 - \left(\frac{T}{T_c} \right)^2 \right)$.

There are three regions for type-II superconductors: Meissner state, mixed state and normal state. Two surface boundaries of energy among these regions are lower critical field H_{c1} and upper critical field H_{c2}, respectively. In type II superconductor, penetration of flux was started in the specimen at a field value H_{c1}, which is lower than the critical field $H = H_c$ in type-I superconductors. The magnetic field penetrates partially into the material in the mixed state (like Figure 2.6 (a) shows). The flux lines can go through the normal region inside the superconductor, which is known as the flux vortex area. The shaded areas in Figure 2.6 symbolise normal region (N) through which the magnetic field can pass, while other parts are superconducting regions (S). The unit consisting of normal and superconducting regions in the mixed state was shown in Figure 2.6 (b). The sizes of the normal region and superconducting

region in the centre are related with the coherence length ξ and penetrating depth λ [3]. The flux vortices contain one quantum of flux, which Abrikosov determined as $\Phi_0 = \dfrac{h}{2e} = 2.1 \times 10^{-15}$ Tm². The vortices formed a typically hexagonal lattice called the Abrikosov vortex lattice. The magnetic field gradually reduces until it drops to zero outwards from the central region, that is, the magnetic field is completely screened [3]. When the vortices are pinned or trapped, the resistivity of the superconductor may reduce to zero [24]. The electrical properties in the superconducting state are also seen up to a field H_{c2} which is larger than H_c. As the external field reaches to H_{c2}, the size of the superconducting region between the cores of the flux lines minimise to zero, and the superconductor presents a continuous transition towards the normal state [25].

(a)   (b)
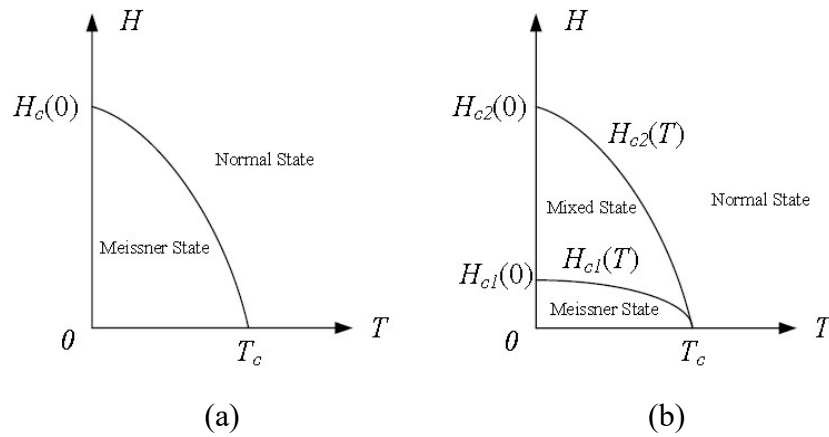
Figure 2.4: Critical magnetic field as a function of temperature for (a) type-I superconductor and (b) type-II superconductor [3].

(a)   (b)
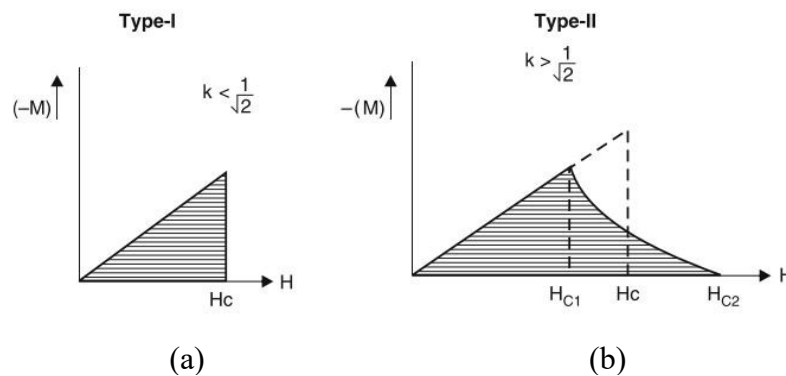
Figure 2.5: Magnetisation versus applied magnetic field for type-I and type-II superconductors [25].

11

(a)   (b)
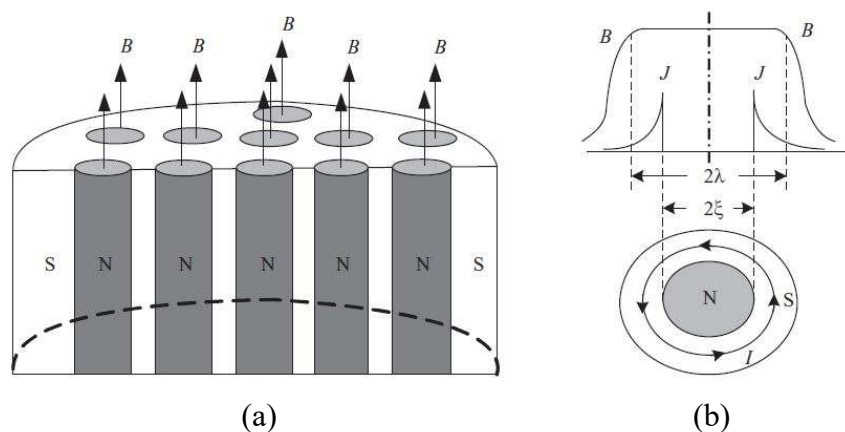
Figure 2.6: Type-II superconductors in the mixed state: (a) mixed state; (b) distribution of magnetic field and current density in a unit consisting of normal and superconducting regions [3].

When there is current flowing in a type-II superconductor, the current will generate its own magnetic field which will pass through the superconductor as a vortex lattice. This will give rise to a Lorentz force on each flux vortex. This force can cause the vortices to move. As a result, it generates an electric field and a non-zero resistivity. Therefore, the flux lattice needs to be 'pinned' for any practical use of the superconductor involving current flow. The pinning forces can impede magnetic fluxes from moving. The higher the pinning force, the higher the current density that can be passed through a sample before its self-field causes flux motion. Such superconductors are also called "hard" type-II superconductors. Thus, flux pinning is an important factor to determine the critical current of type-II superconductors.

The irreversibility field H_{irr} is another defined field for type-II superconductors, which is of practical importance for engineering applications. As long as an applied magnetic field above this value, the vortices begin to move, leading to extra dissipation. For a given temperature, H_{irr} represents the magnetic field limits a superconductor can be exposed to before becoming unusable. The magnitude of H_{irr} is lower than that of H_{c2}. As for YBCO, for example, the irreversibility field is up to 5-6 T (@77 K) [26].

Almost all pure elemental superconductors are type-I. Type-II superconductors are mainly metallic compounds and alloys, as well as low-temperature superconductor (LTS) and HTS. The critical fields for type-I superconductors were normally lower than 120 mT [27]. Comparing with type-I, type-II superconductors can carry larger current in high magnetic fields since H_{c2} can be much higher than H_c. For instance, at a temperature of 4 K, upper critical field

density B_{c2} is 12 T for NbTi, 27 T for Nb$_3$Sn, 15 T for MgB$_2$, and over 100 T for YBCO and Bi-2223 [28]. Another way to classify the type-I and type-II superconductors is dependence on the ratio of penetration depth λ to coherence length ξ according to the Ginzburg–Landau theory. By defining the temperature-dependent Ginzburg–Landau parameter κ as:

$$\kappa = \frac{\lambda(T)}{\xi(T)} \tag{2.1}$$
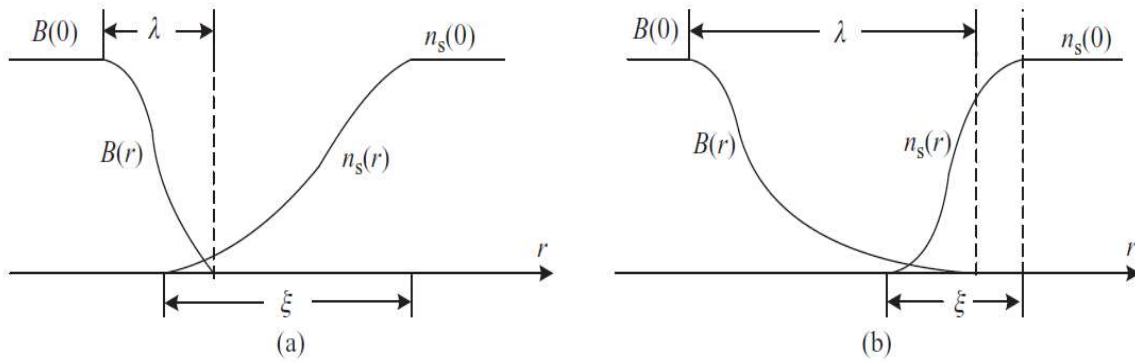
Figure 2.7: Penetration depth and coherence length of superconductors and their interfaces: (a) Type-I superconductor and (b) Type-II superconductor.

If $\kappa < 1/\sqrt{2}$, superconductors have a positive interface of energy and are called type-I superconductors; on the contrary, if $\kappa > 1/\sqrt{2}$, superconductors have a negative interface of energy and are defined as type-II superconductors. Figure 2.7 expresses the relationship of coherence length ξ and penetration depth λ of type-I and type-II superconductors. $n_s(r)$ (the square of the absolute value of the wave function) and $B(r)$ separately refer to the spatial distribution of superconducting electron density and the magnetic flux density at the interface between the normal and superconducting regions. The regions with $B(0)$, $n_s(0)$ correspond to the normal region and superconducting region. The mixed area with a combination of $B(r)$ and $n_s(r)$ denotes the interface of normal and superconducting regions [3].

2.1.3 Low-temperature and high-temperature superconductors

Figure 2.8 presents the history of the discovery of superconducting materials. When superconductors were discovered in the early days, pure metals were used as materials of superconductors. The critical temperature T_c of solid mercury was only 4.2 K. In the next decades, great efforts were devoted to finding suitable superconducting materials. In the late 1950s and early 1960s, for practical applications, conventional LTS are metal-alloys and most known LTS were composed of no more than two elements and were mainly elemental superconductors, alloys, and intermetallics [29]. Niobium-titanium (NbTi) and Niobium–tin (Nb$_3$Sn) are widely used low-temperature superconductors and can be used as high field magnets. Their critical currents are 9 and 18 K, respectively. However, the operating temperature need to be cooled down to 5 K in most applications [8]. Due to the requirement of lower operating temperature, the mostly used coolant for low-temperature superconductors is liquid helium, which is quite costly. On top of that, during the manufacture, silver is an essential element, which also increases the cost.

As for high-temperature superconductors, LSCO (La$_{-x}$Sr$_x$C$_u$O$_2$) was the first high-temperature superconductor created by Bednorz and Muller in 1986. Most of the high-temperature superconductors are copper oxides, such as BiSrCaCuO (BSCCO) and YBa$_2$Cu$_3$O$_7$ (YBCO). The critical temperature T_c for these superconductors are 110 K and 92 K, respectively [30]. There are still some with simple structures, such as MgB$_2$ with T_c of 39 K [31] and iron-based layered superconductors FeSC with T_c up to 58 K [32].

As one of the most popular second generation (2G - the second HTS to be used for manufacturing conducting wires) HTS, YBCO was discovered by Paul C. W. Chu and M-K. Wu in 1986 and 1987, respectively. It was the first material working above 77 K which is the boiling point of liquid nitrogen. Compared with a low-temperature superconductor, the usage of liquid nitrogen significantly reduces the cooling cost, which makes the high-temperature superconductor as a superior choice and boosts the development of practical application.
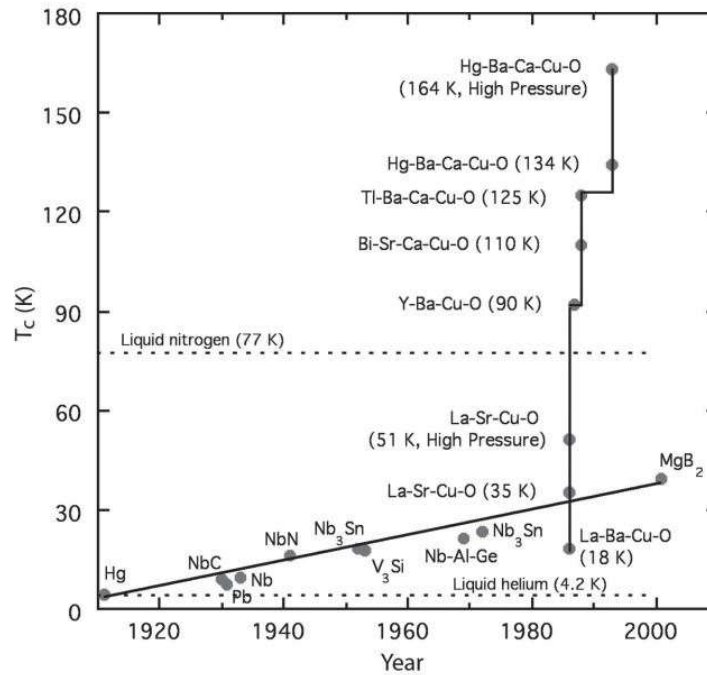
Figure 2.8: History and critical temperature T_c of important superconducting materials [33].

2.2 Critical state models

Critical state models (CSM) are utilised in many cases not only to imitate the macroscopic behaviour of superconducting materials but also to simplify the distribution of magnetic field and current density and calculation of AC losses. They are based on quasi-static conditions that flux vortices are pinned in the superconductor steadfastly and adjusted immediately to another equilibrium state when the external magnetic field alters. For most of the CSM models, they separate the model into two parts. One is the critical state region, and the other is the virgin region (no current or electric field). The critical state always appears at the outer layer of the material when an applied field exceeds the lower critical magnetic field H_{c1} of a type-II superconductor. Magnetic flux vortices with circulating superconducting shielding currents penetrate the material to shield the interior of the material from the applied current or field. The vortices are pinned at locations of defects in the crystal lattice of the material. The penetration depths are associated with the magnitude of the applied current or field [34].

The research on CSM models are quite a lot. The most classical and basic model was introduced by Bean. Then lots of researchers promote his model into a more precise level. This chapter will thoroughly discuss Bean's model and follow on the extended model proposed by Rhyner and Kim.

2.2.1 Bean model

The authentic state in a superconducting strip is quite complicated for us to estimate and calculate. Bean proposed a method to simplify the distribution of magnetic field and current density in the slab by which we can easily analyse the magnetic field, current density, penetrated magnetic flux and AC losses. The Bean model proposes that the magnitude of the actual current density is either zero or J_c (when the direction is included it takes three values, zero and $\pm J_c$). It assumes that a fixed critical current density J_c in the direction of the electric field can be produced by the smallest electric field. If an electric field is applied and then reduced to zero, the current density resists at J_c in its original direction (the current density vanishes only in a virgin material). When the whole superconductor has been penetrated with plus or minus J_c the superconductor is said to be in a critical state [34-36].

Assume a slab with the thickness of *2a* in the *x*-direction, *2w* in the *y*-direction and infinite length in the *z*-direction as shown in Figure 2.9.

The distribution of the magnetic field and current density in a slab of the superconductor is described by Ampere's Law:

$$\nabla \times B = \mu_0 J_c \tag{2.2}$$

The equation can be simplified as:

$$\frac{dB}{dx} = \mu_0 J_c \tag{2.3}$$
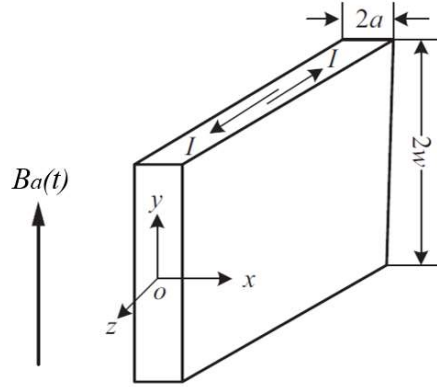
Figure 2.9: Superconducting slab with the width of *2a* with an external magnetic field.

The distribution of the magnetic field inside the superconductors can be obtained by solving:

$$B(x) = B_\mathrm{a} - \mu_0 J_c |x_p| \tag{2.4}$$

The magnetic field inside the slab declines with the penetration depth x_p. B_a is the amplitude of the external magnetic field outside the slab. μ_0 is the vacuum permeability. When the external magnetic field is relatively small, the magnetic field is zero at point x_p, that is:

$$x_p = B_a/(\mu_0 J_c) \tag{2.5}$$

when the magnetic field B_a gradually rises until it just reaches the centre of the slab, that is $B_a = \mu_0 J_c a$. It indicates the magnetic field fully penetrates the slab. The external magnetic field at this time is known as the complete penetrated magnetic field B_p,

$$B_p = \mu_0 J_c a \tag{2.6}$$

where a is the width from the centre to the edge (half thickness of the slab). When the external magnetic field increases, the magnetic field at the centre of the slab also grows. The distribution analysis of the current density and magnetic field of an infinite slab when there is applied magnetic fields or transporting currents can be seen in Figure 2.10 and Figure 2.11.
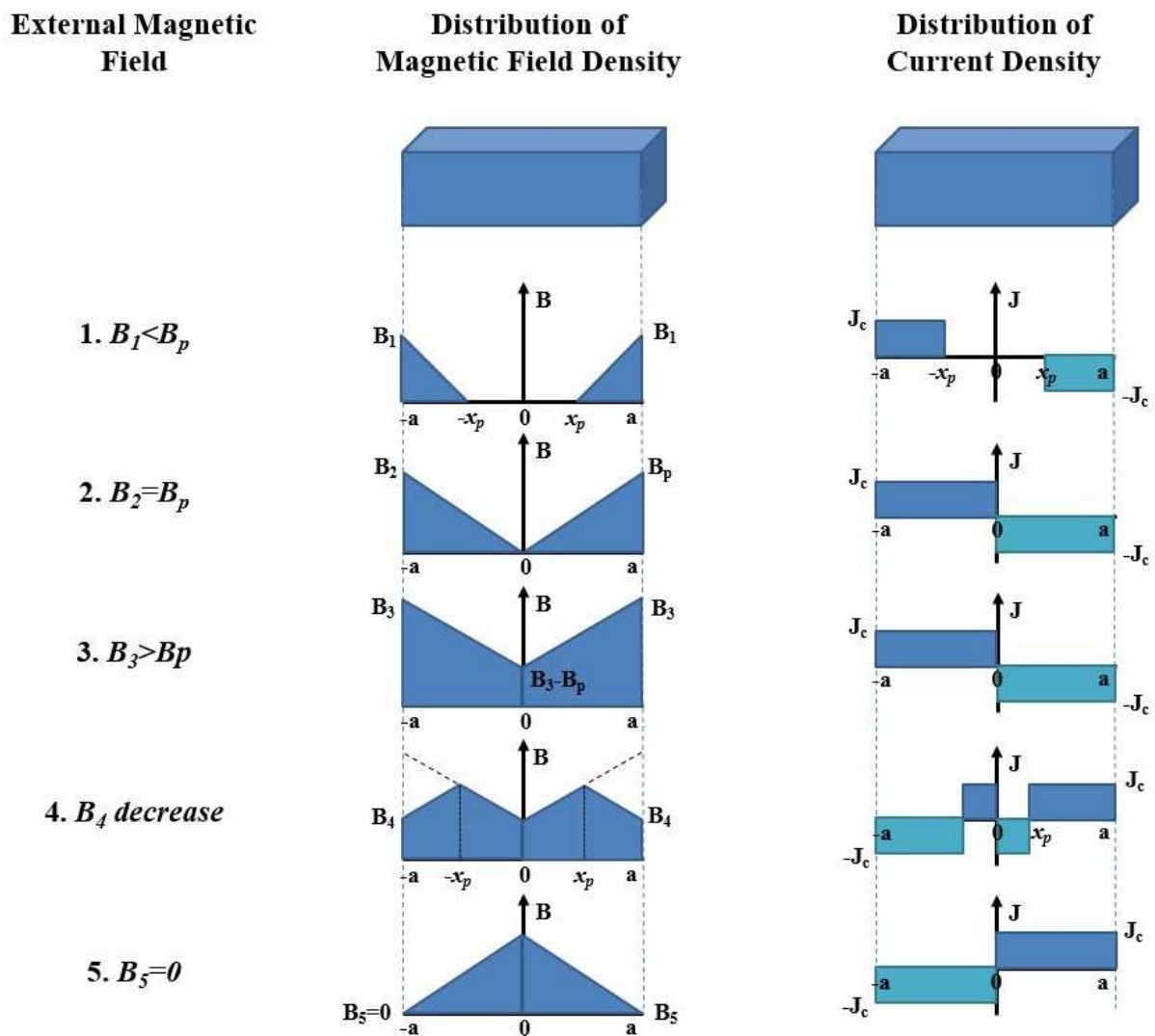
Figure 2.10: Magnetic field and current density distribution with only external magnetic fields, where J_c is the critical current density, B_p is the magnetic field to fully magnetise the slab, x_p is the penetration depth.

.
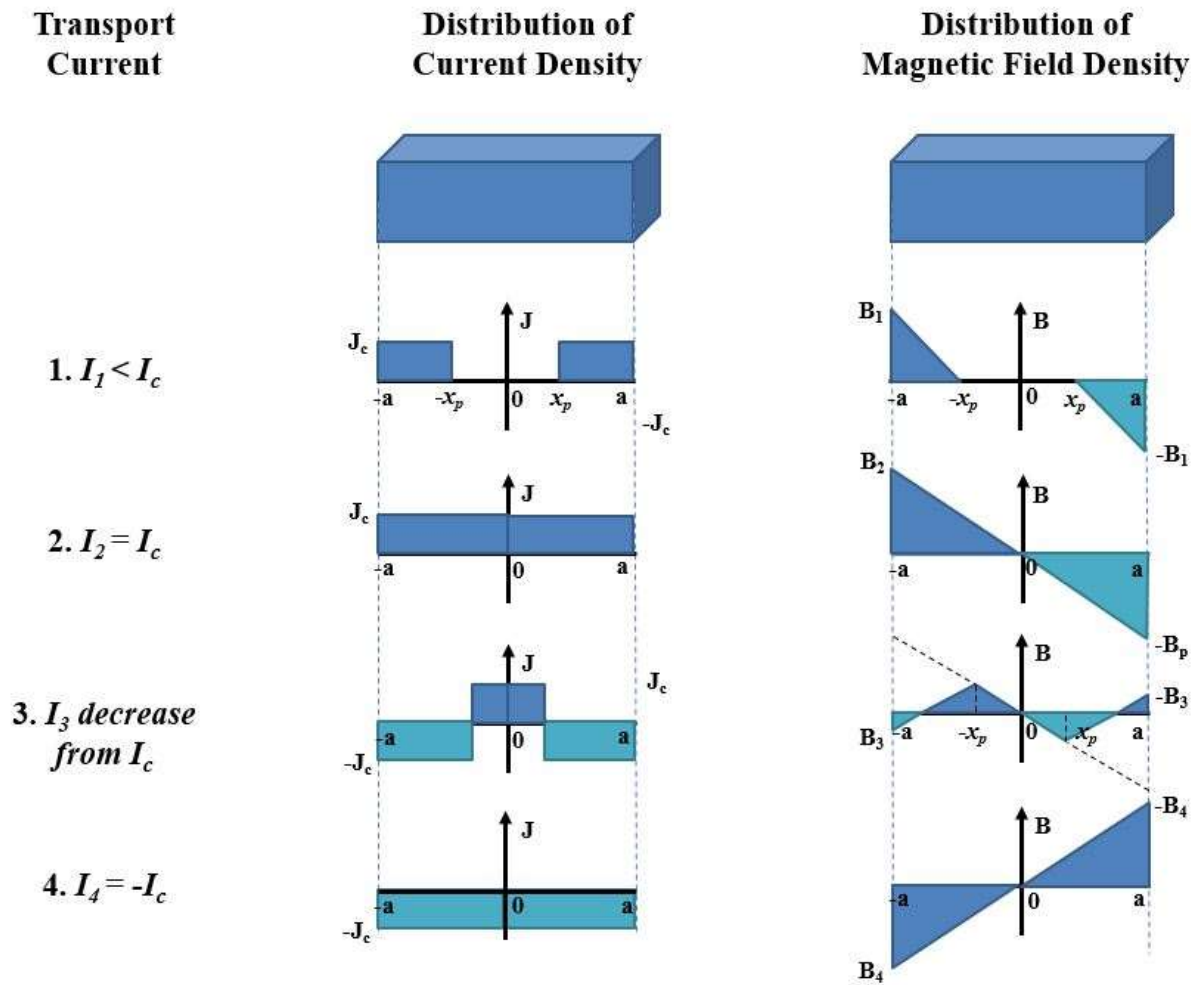
Figure 2.11: Magnetic field and current density distribution with only transport currents, where I_c and J_c are the critical current and critical current density respectively, B_p is the magnetic field to fully magnetise the slab, x_p is the penetration depth.

The Bean model is of significance for two reasons. First of all, it introduces a domain-like structure into the current density and greatly simplifies loss calculations. Secondly, the first attribute seems to be retained even in modified models which allow J_c to depend on the magnetic field [34-36].

2.2.2 E-J power law

According to Bean's model, the relationship between the current density and the electric field needs further analysis. Rhyner stated a function of E-J power law which is widely used to characterise the non-linear behaviour of flux creep and flux flow [37]:

$$E = E_0 \left(\frac{J}{J_c}\right)^n \tag{2.7}$$
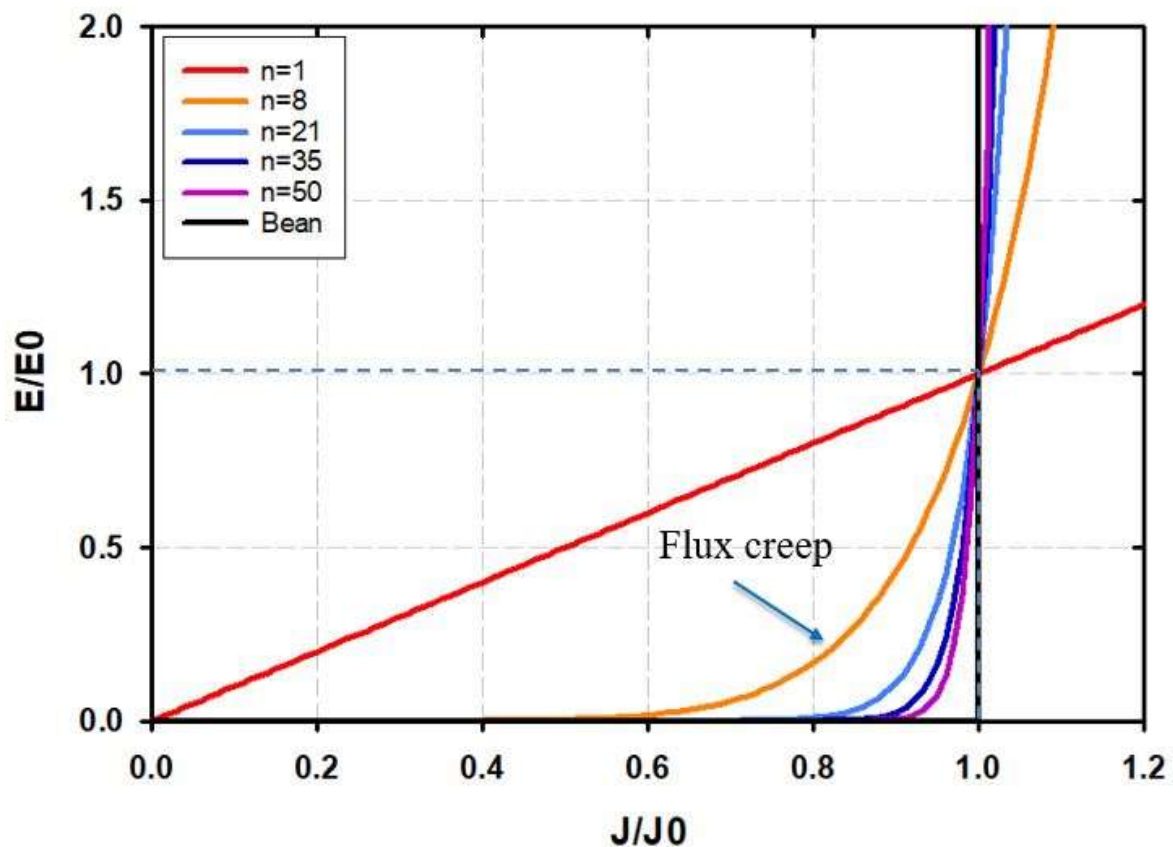
Figure 2.12: Typical E-J characteristics of a superconductor from $n = 1$ (linear) to $n = \infty$ (Bean's model).

where E is the longitudinal electric field within the superconductor; E_0 and J_c are the characteristic electric field (1 e^{-4} V/m) and critical current density, respectively; n is a characteristic parameter of a given superconductor, which describes the relationship of the

voltage drop across the wire to the applied current [8]. The variety of n value corresponds to different superconducting behaviour. For $n = 1$ the equation displays a linear line which seems like normal metal; $n = 8$ represents a superconductor with strong flux creep; $n = 21$ and 35 are values normally taken in the simulation; and $n = 50$ is the limiting value between HTS and LTS superconductors [38]. Normally for a good approximation of the Bean model, n should be larger than 20. Figure 2.12 shows the E-J curve of a superconductor with varying n values from 1 to infinite. The critical current (I_c) of a superconductor is always defined as the current that produces a voltage drop of 1 μV/cm in the industry [8].

2.2.3 Kim model

As we discussed in 2.1.1.3, the three factors (current density, magnetic field and temperature) are associated with each other. Only below the critical temperature and critical magnetic field, can the superconductivity persist. Kim [39] and Anderson [40] proposed the critical current in type-II superconductors depends much on the temperature, as well as the local magnetic field. Their relationship can be interpreted as follow:

$$J_c(B) = \frac{\alpha(T)}{B_0 + B} = \frac{J_{c0}(T)}{1 + \frac{B}{B_0}} \tag{2.8}$$

where B_0 is a characteristic magnetic field which relies on the material; $J_{c0}(T) = \frac{\alpha(T)}{B_0}$; α is related to the temperature, given by:

$$\alpha = \frac{1}{d_0}(c - bT) \tag{2.9}$$

where d_0 is dependent on the physical microstructure of the material and $\frac{c}{b} \leq T_c$.

If we only consider the magnetic field of the y-axis since the perpendicular field has more effects on the AC losses than that of a transverse or parallel field [41], the current density and power index will be given as:

$$J_c(B) = \frac{J_{c0}}{1+\frac{|B_y|}{B_0}} \tag{2.10}$$

$$n(B) = \frac{n_{c0}}{1+\frac{|B_y|}{B_0}} \tag{2.11}$$

where J_{c0} and n_{c0} are the critical current density and power index in a self field. B_0 is gathered from the I_c-B_{DC} experimental curve. The results adopting these equations in models are more accurate, especially for the model where both transport current and external magnetic field are applied.

If the orientation of the magnetic field corresponding to the superconductor is taken into account, the equation can be expressed by [42, 43]:

$$J_c(B_\perp, B_\parallel) = J_{c0}(T)\left(1 + \frac{\sqrt{B_\perp{}^2 + k_0{}^2 B_\parallel{}^2}}{B_0}\right)^{-\beta} \tag{2.12}$$

where $B_\perp$ and $B_\parallel$ are the magnetic field perpendicular and parallel to the flat surface of the superconducting tape, respectively; k is the anisotropy parameter and usually less than 1; B_0 and β are the parameters to determine the rapidity of the J_c reduction with the magnetic field. k_0, B_0 and β are temperature-dependent variables. The so-called elliptical approximation is a more precise way to reproduce experimental data [44, 45].

2.3 Numerical modelling

2.3.1 Overview of numerical modelling

Analysis methods like CSM are capable of solving problems with simple structure. However, when the models become complicated, numerical models are powerful to solve cases involved with transporting currents, magnetic fields and even forces and temperature.

The finite element method (FEM) is a convenient tool for solving partial differential equations (PDEs). It is always used with Ampere's law to calculate current and magnetic field distributions since Ampere's law relates the magnetic field to the current source. Maxwell's equation can be transferred into different formats to satisfy FEM implementation [46]. There are three formulas used most in FEM application: the A-V-formulation, which is based on the magnetic vector potential; the T-Ω-formulation, which is based on the current vector potential, and the H-formulation, which is based on the magnetic field [44, 47]. The name of each formula is based on the variables solved by the formula. Other FEM models, such as E or J formulations and Campbell's equation were also investigated in several research [48-50].

Compared with the other formulations, H-formulation has fewer variables and easy to integrate the boundary conditions. Therefore, H-formulation will be selected to be the main formulation of the simulation models in this thesis. A new numerical model was developed in recent years, which is the T-A formulation. It is suitable for solving models occupying lots of computational time [51, 52]. Both approaches will be illustrated in section 2.3.2 and 2.3.3.

2.3.2 *H*-formulation 2D&3D

H-formulation was first reported in 2003 and was developed and used by many research groups worldwide [53-59]. Compared to the other differential methods, the H-formulation has the advantages of using the fewest variables, easily setting boundary conditions and avoidance of unstable calculations. Another obvious advantage is that it can be applied using commercial software, which saves us plenty of time on tedious programming [46].

The dimension of a model chooses to simulate mostly depends on the number of variables involved. 2D and 3D H-formulation models are widely used in research. Both models will be illustrated in this chapter.

2.3.2.1 2D H-formulation models

Cartesian and cylindrical coordinates are two basic model coordinates formed in 2D models. As shown in Figure 2.13, the model in Cartesian coordinates is ideally used for an infinitely long tape or sample which can be asymmetric. Whereas, axisymmetric objects, such as bulks or coils, are more suitable for 2D cylindrical models.
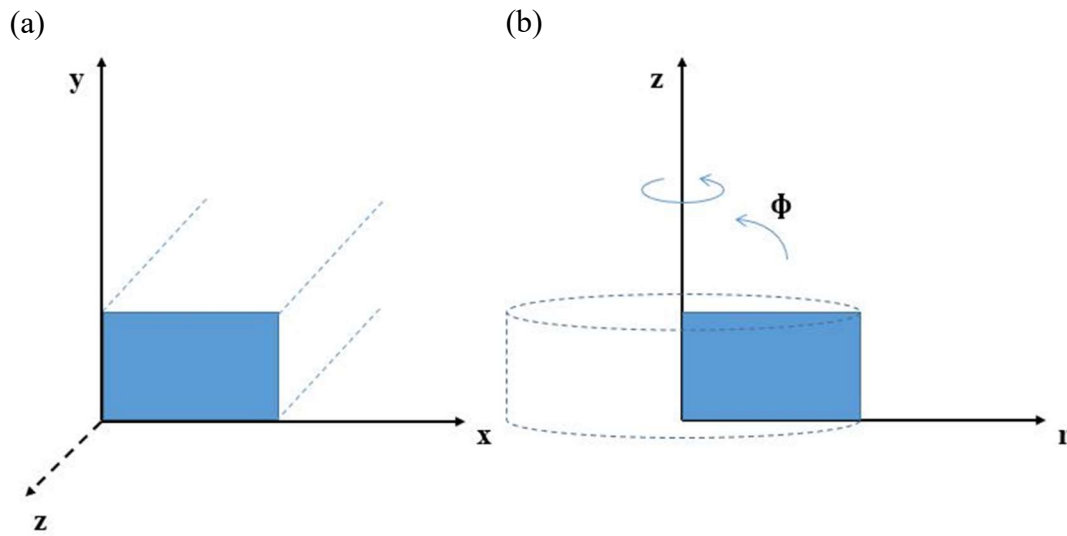
Figure 2.13: Comparison of the 2D coordinate system between (a) Cartesian and (b) cylindrical coordinate.

A set of PDEs is defined in each subdomain and boundaries. All of these PDEs use the same dependent variables and based on Faraday's Law and Ampere's law [53]:

$$\nabla \times \boldsymbol{E} = -\mu \frac{d\boldsymbol{H}}{dt} \tag{2.13}$$

$$\nabla \times \boldsymbol{H} = \boldsymbol{J} \tag{2.14}$$

Boundary conditions are essential for the modelling cases where part of the sample is under certain condition. The Dirichlet condition is widely used in electromagnetic modelling. It can define how the external magnetic field or the applied current varies with time.

The equations can also be represented by the general PDE form:

$$\nabla \times (\rho \nabla \times \boldsymbol{H}) + \mu \frac{d\boldsymbol{H}}{dt} = 0 \tag{2.15}$$

These basic equations will be the foundation of the simulation work in Chapter 3, Chapter 4 and Chapter 6.

2.3.2.2 3D H-formulation

3D models include more variables compared to 2D models. It demonstrates better views of models, especially for irregular geometry models. However, the computation time will increase as well with more elements to solve.

There are three variables for magnetic field, current density and electric field:

$$H = [H_x; H_y; H_z], J = [J_x; J_y; J_z], E = [E_x; E_y; E_z] \qquad (2.16)$$

The governing equations can be expressed in Table 2.1:

Table 2.1: Governing equations of 3D H-formulation model

Faraday's law	$$\begin{bmatrix} \dfrac{\partial E_z}{\partial y} - \dfrac{\partial E_y}{\partial z} \\[2mm] \dfrac{\partial E_x}{\partial z} - \dfrac{\partial E_z}{\partial x} \\[2mm] \dfrac{\partial E_y}{\partial x} - \dfrac{\partial E_x}{\partial y} \end{bmatrix} = -\mu_0\mu_r \begin{bmatrix} \dfrac{\partial H_x}{\partial t} \\[2mm] \dfrac{\partial H_y}{\partial t} \\[2mm] \dfrac{\partial H_z}{\partial t} \end{bmatrix}$$
Ampere's law	$$\begin{bmatrix} J_x \\ J_y \\ J_z \end{bmatrix} = \begin{bmatrix} \dfrac{\partial H_z}{\partial y} - \dfrac{\partial H_y}{\partial z} \\[2mm] \dfrac{\partial H_x}{\partial z} - \dfrac{\partial H_z}{\partial x} \\[2mm] \dfrac{\partial H_y}{\partial x} - \dfrac{\partial H_x}{\partial y} \end{bmatrix}$$
E-J power law (assuming an isotropic material)	$$\begin{bmatrix} E_x \\ E_y \\ E_z \end{bmatrix} = E_0 \begin{bmatrix} \dfrac{J_x}{J_{norm}}\left(\dfrac{J_{norm}}{J_c}\right)^n \\[2mm] \dfrac{J_y}{J_{norm}}\left(\dfrac{J_{norm}}{J_c}\right)^n \\[2mm] \dfrac{J_z}{J_{norm}}\left(\dfrac{J_{norm}}{J_c}\right)^n \end{bmatrix}$$ where $J_{norm} = \sqrt{J_x^2 + J_y^2 + J_z^2}$, $E_{norm} = \sqrt{E_x^2 + E_y^2 + E_z^2}$
Dirichlet boundary condition	$$H = f(t)$$ $$f(t) = \begin{bmatrix} f_x(t); & f_y(t); & f_z(t) \end{bmatrix}$$

2.3.3 *T-A* formulation 2D&3D

The simulation time and memory requirement for extensive or complicated structure models can be excessive. *T-A* formulation is a new efficient simulation method which assumes the superconducting layer as a thin film with no thickness. It saves plenty of computation time and has been validated that it is an excellent choice for simulating large–scale 2G HTS stacks, coils and cables [51, 52, 60, 61].

The *T-A* formulation involves two state variables: the current vector potential *T* and the magnetic vector potential *A,* which are defined as:

$$\boldsymbol{J} = \nabla \times \boldsymbol{T} \tag{2.17}$$

$$\boldsymbol{B} = \nabla \times \boldsymbol{A} \tag{2.18}$$

The current vector potential is simulated just in the superconducting domain. The magnetic vector potential, however, is simulated in the whole model space.

In a 3D space, the current only flows in the tangential direction of the superconducting layer. Thus, the computation speed is dramatically increased since the 3D problem can be simplified to a 2D thin shell with scalar variables T. The entire scheme is shown in Figure 2.14. The current vector potential T can be expressed as:

$$\boldsymbol{J} = \nabla \times (\boldsymbol{T} \cdot \vec{n}) \tag{2.19}$$

where $\vec{n}$ is the normal vector of the domain:

$$\vec{n} = \begin{bmatrix} n_x \\ n_y \\ n_z \end{bmatrix} \tag{2.20}$$

If a transport current is applied to the strip, a boundary condition is required to apply on the edges of the thin shell to impose the transport current:

$$I = (T_1 - T_2) \cdot d \tag{2.21}$$

Where T_1 and T_2 are the values of T on the left and right edge, respectively, as shown in Figure 2.14. d is the real thickness of the superconducting layer. The values of T on the upper and lower edges are equivalent to zero since T is perpendicular to the surface of HTS layer [51].

27
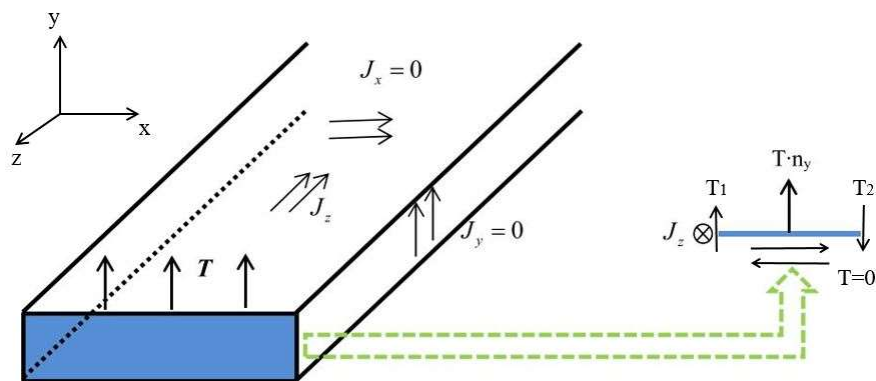
Figure 2.14: Schematic of *T-A* formulation for a single 2G HTS layer (the thickness of the superconducting layer is also presented in the diagram for better visualisation and understanding). The superconducting layer is simulated as a line (like the figure arrow pointed on the right) in actual *T-A* model [52]. Boundary condition of the transport current is also presented in the figure arrow pointed.

(a)

(b)
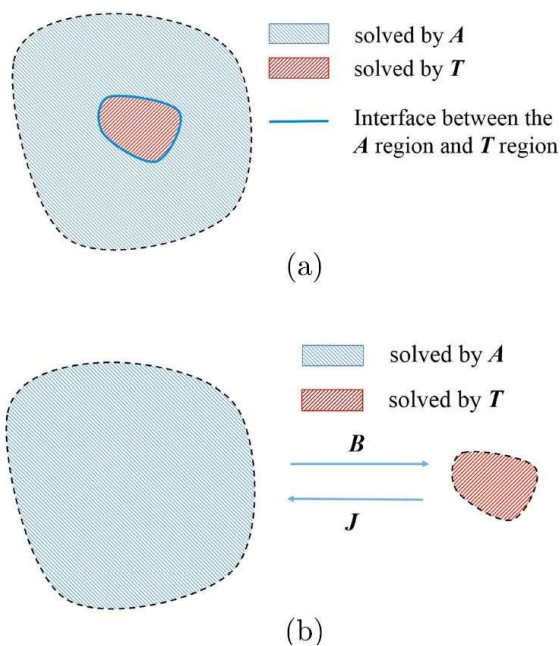
Figure 2.15: Relationship between current vector potential *T* and the magnetic vector potential *A* in (a) the simulation of typical eddy current; (b) the simulation of a coated conductor in the *T–A* formulation [51].

Previous eddy current problems used vector and scalar potential functions to define the field magnitudes [62]. Figure 2.15 (a) shows the relationship between T and A in the simulation of typical eddy current by fully coupling T and A since T and A are solved at the same time. The challenge of this method is that the interface boundary should be considered carefully to hybridise different vectors in a formulation. However, there is no interface boundary between different vectors in T-A formulation models. As Figure 2.15 (b) presents, T and A are solved separately in the simulation of a coated conductor in the T–A formulation. Current density J (solved at T within the superconducting region) and magnetic field density B (solved at A in the whole space) are exchanged between these two regions.

In T-A formulation model, Faraday's Law will be expressed as:

$$\nabla \times (\rho \nabla \times (\boldsymbol{T} \cdot \vec{n})) = -\frac{d\boldsymbol{B}}{dt} \tag{2.22}$$

Ampere's law will be written as:

$$\nabla \times (\nabla \times \boldsymbol{A}) = \mu J \tag{2.23}$$

2.4 Magnetisation

Significant advantages to superconducting trapped field magnets like bulks or stacks, when compared to conventional magnets, are due to the flux pinning in the interior of superconductors. The magnetisation of superconductors is hysteretic but fundamentally varies from the magnetisation of ferromagnetic materials which has local values everywhere within the material. For a hard type-II superconductor, the magnetisation process is irreversible and similar to a ferromagnetic material. The local value is the field generated by the currents. The volume average of the local magnetisation can be defined as M. The main parameters of magnetisation for different geometries of superconductors in the critical state were summarised in [63]. Figure 2.16 presents the magnetisation loop of an infinite slab with different amplitudes

of maximum applied fields H_m. The magnetisation and applied field H_a are normalized by the saturation magnetisation ($M_{sat} = J_c d/4$) and the penetration field ($H_p = J_c d/2$), respectively [63]. J_c and d represent the critical current density and the width of the plane. The loops were determined with the following sequence of applied fields: $0 \rightarrow H_{m,0.5} \rightarrow -H_{m,0.5} \rightarrow H_{m,1} \rightarrow -H_{m,1} \rightarrow H_{m,2} \rightarrow -H_{m,2} \rightarrow H_{m,3} \rightarrow -H_{m,3} \rightarrow H_{m,3}$, where $H_{m,i} = iH_p$. In terms of the loops, the remnant magnetisation cannot be higher (in magnitude) than the saturation one [63].
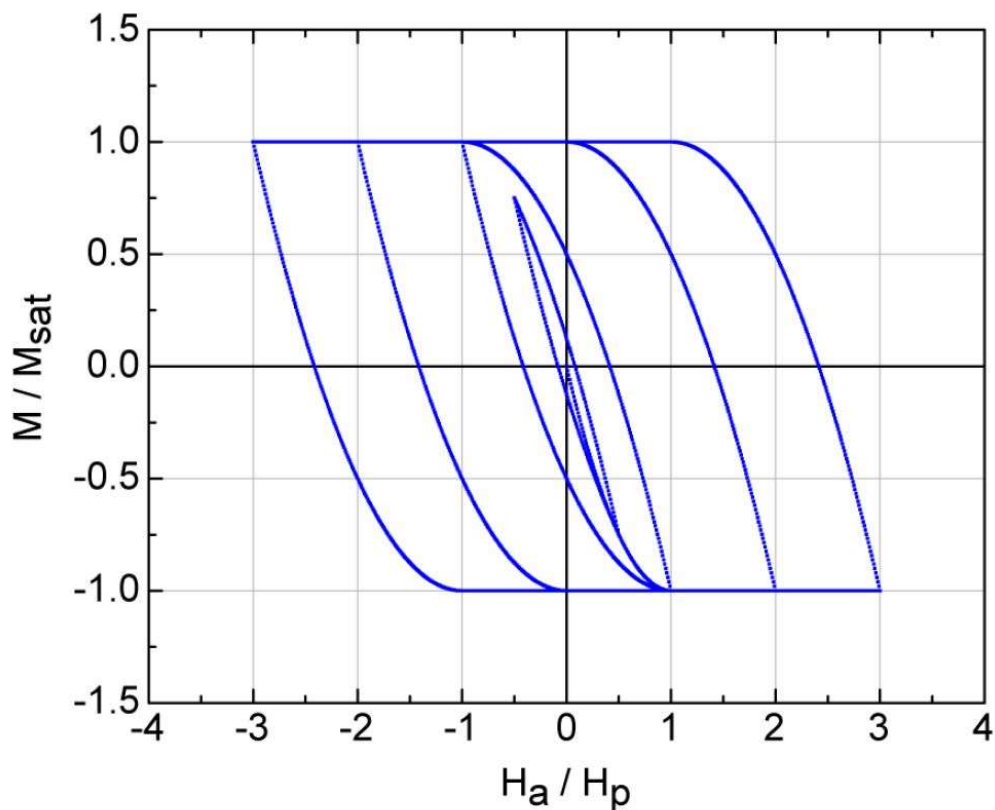
Figure 2.16: Magnetisation loops for an infinite slab with different amplitudes of maximum applied fields H_m [63].

2.4.1 Magnetisation methods

Magnetisation is, as the name implies, the ability to generate a magnetic field. To achieve effective, stable, and inexpensive magnetisation, various techniques have been used in different research. The most common methods can be separated into two categories. One is the traditional field magnetisation, which contains field cooling (FC) and zero-field cooling (ZFC).

The other is novel magnetisation, which includes pulsed-field magnetisation (PFM) and flux pump. PFM will be the main method discussed in the next chapters.

2.4.1.1 Field cooling (FC) and zero-field cooling (ZFC) magnetisation

In the process of FC and ZFC magnetisations, the variation rate of the magnetic field is not as fast as the pulse field magnetisation, which always ramps up or down in few minutes or even hours. Therefore, the temperature rises in FC and ZFC magnetisations can usually be ignored. The principles for FC and ZFC techniques are related to cooling temperature and external magnetic field and can be explained by CSM in Figure 2.17.
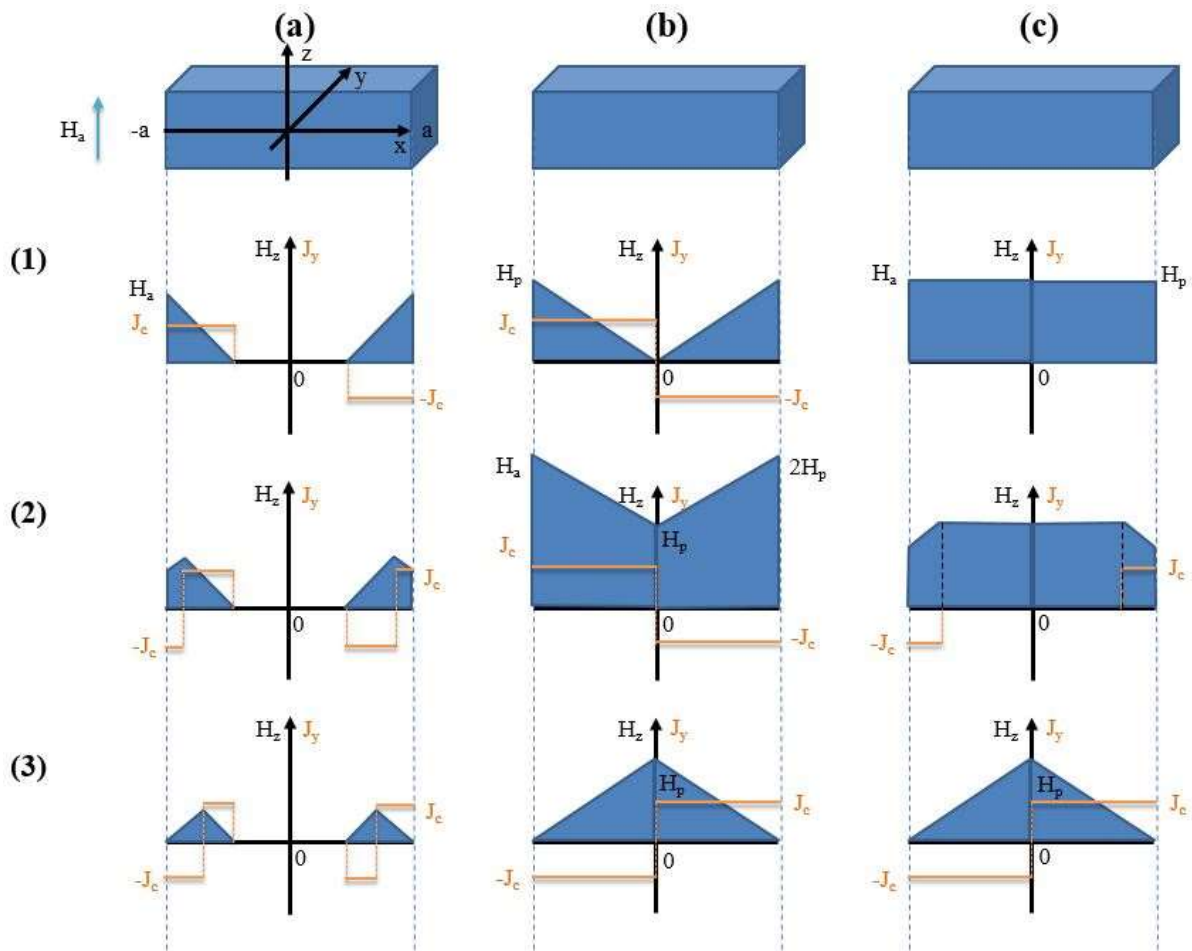
Figure 2.17: Distribution of magnetic field and current density of an infinite HTS slab displayed by Bean model in (a) partially magnetised ZFC magnetisation ($H_a < H_p$ is applied to the slab and then removed); (b) fully magnetised ZFC magnetisation ($H_a = 2H_p$ is applied to the slab and then removed); (c) fully magnetised FC magnetisation ($H_a = H_p$ is applied to the slab and then removed).

The magnetisation process of an infinite slab with the width of *2a* exposed in a magnetic field H_a parallel to the x-z plane as shown in Figure 2.17. H_p is the penetration field which equals to $J_c a$. In the ZFC presented in Figure 2.17 (a) and (b), the superconducting sample is firstly cooled down to the superconducting state without any applied magnetic field which is below its critical temperature T_c. And then a ramping field is added to the sample, which is typically several teslas and the magnitude should be at least twice of the penetration field to fully magnetise the slab. Finally, the external field is reduced to zero and the trapped field will remain in the superconducting sample. A reverse operation process is applied to the FC method in Figure 2.17 (c). The field is applied to the superconductor in the normal state ($T > T_c$). After that the superconducting sample is cooled below T_c, then the field is removed. However, the magnitude of the applied field needs to be higher than the final trapped field (H_p) but not as larger as the ZFC method ($2H_p$). Therefore, compared with the ZFC, the FC method is suitable for an experiment to achieve higher trapped field with magnetizing magnets which can only generate lower magnetic fields.

Both ZFC and FC methods require large excitation magnets which can supply much higher magnetic fields and a lower changing rate than pulsed-field magnetisation. Higher trapped fields can be achieved by these two methods with no doubt. Expense on money, time and space occupation will increase at the same time.

2.4.1.2 Pulsed-field Magnetisation

Pulsed-field magnetisation is a promising magnetisation method in recent years. The process and facilities required are relatively inexpensive and compact in contrast to the FC and ZFC. It can be considered as a special case of zero-field cooling. Since it is not necessary for the PFM to reach the desired temperature with a static high field, the field can be accomplished in very short time with lower magnitudes generated. The time duration for a pulse is typically within 0.1 seconds, which can be achieved by using the reinforced copper coils and capacitor banks.

An example experiment rig for the PFM is shown in Figure 2.18. It can be separated into two parts. One is the charge part which contains a power source and a capacitor bank. Another is the discharge part which includes the magnetisation coil(s), a capacitor bank and diodes. The

HTS sample will be magnetised by the pulsed magnetic field produced by the magnetisation coil(s) which is discharged by the capacitor bank for milliseconds. The experiment work is based on this setup and will be detailed further in Chapter 5.

An exponential equation related to the magnetic field and time can be used in a simulation to represent the pulse [64]:

$$B_{app}(t) = B_a \frac{t}{\tau} e^{\left(1 - \frac{t}{\tau}\right)} \tag{2.24}$$

where τ is an appropriate value for the rise time of the pulse. With different values of τ, the durations of pulses will be various.
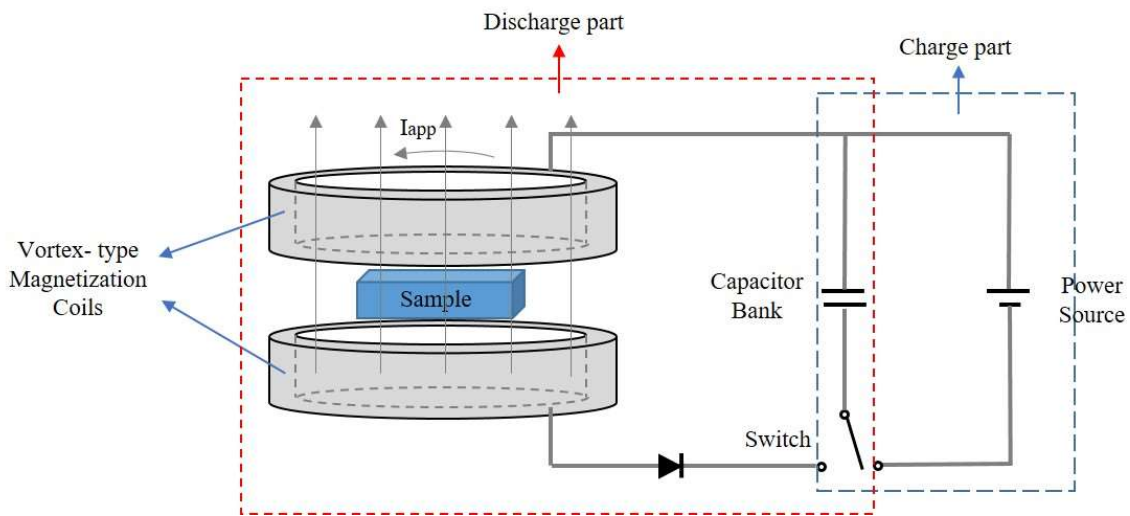
Figure 2.18: Diagram of the experimental test rig for pulse field magnetisation of a sample.

One of the inevitable drawbacks for PFM is the temperature rise due to the fast-dynamic motions of magnetic flux during PFM process, which gives rise to lower trapped fields produced compared with the FC or ZFC technique reached. The difference is more obvious at a lower temperature (much lower than the T_c). When the operating temperature approaches to T_c, the trapped fields produced by the PFM can be close to that of the FC or ZFC [65].

The record trapped field by the PFM is 5.2 T (@29 K) for bulks and 2 T (@10 K) for stacks, which is far more lower than the trapped field generated by the ZFC or FC, 17.6 T (@26 K) for bulks and 17.7 T (@8 K) for stacks [18, 19, 66, 67]. According to the contribution from previous researchers, the flux dynamics during magnetizing and optimum trapped fields of bulks or stacks by the PFM technique can be affected by different aspects, such as applied-pulse techniques, magnetisation coil arrangements, composite structures of HTS magnets and temperature applied [65]. Detailed discussions about these effects of factors on HTS stacks will be presented in Chapter 4 and 5.
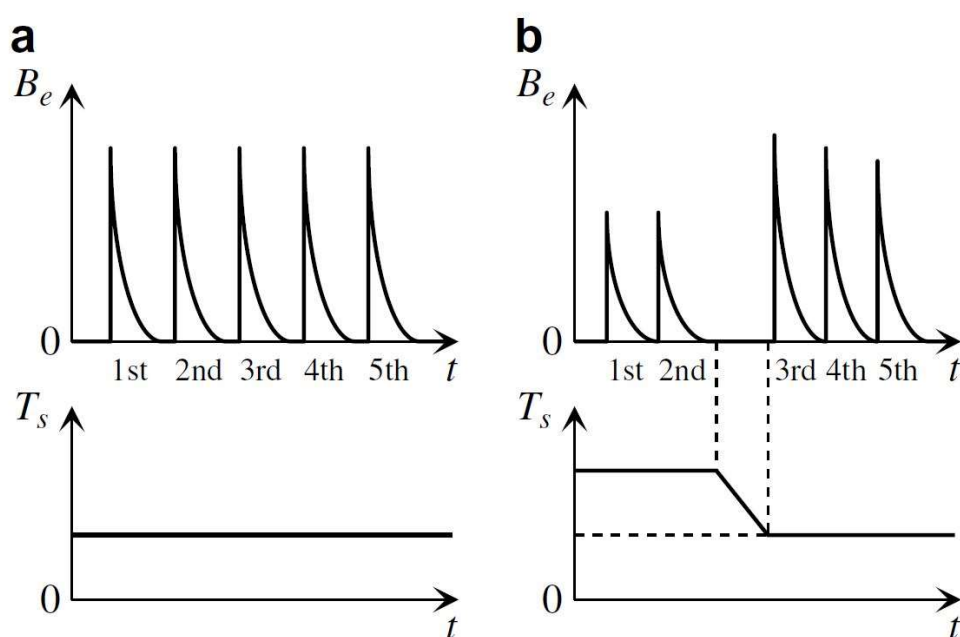
Figure 2.19: Schemes of the applied fields and corresponding cooling temperatures of multi-pulse PFM with (a) SPA technique and (b) MMPSC technique [68].

For applied pulses in PFM, lots of variables need to be taken into account, for example, the pulse magnitude, duration and shape, the number of pulses and so on. Single-pulse magnetisation is the most basic of the PFM techniques. The drawbacks for single-pulse magnetisation is the maximum trapped fields or fluxes is less than the ideal ones compared with the FC or ZFC.

It was proved by both experiment and simulation that the multi-pulse techniques are effective ways to promote the trapped fields of HTS bulks or stacks by the PFM. There are different

types of multi-pulse techniques, including the successive pulsed-field application (SPA), iteratively magnetizing pulsed-field method with reducing amplitude (IMRA), and multi-pulse technique with step-wise cooling (MPSC) [67-75]. Figure 2.19 illustrates the schemes of two techniques. The pulses of external magnetic fields with almost the same strength are applied at a constant temperature for the SPA technique shown in Figure 2.19 (a). For IMRA, the only difference to the SPA is the amplitude of fields applied is reducing like the third, fourth and fifth pulses in Figure 2.19 (b). In a MPSC technique, the sample was first magnetised by pulsed magnetic fields with relatively small magnitude at around a relatively high temperature. Afterward, the sample is cooled down to a lower temperature and applied a few pulsed fields with larger strength. The modified MPSC (MMPSC) presented in Figure 2.19 (b) [71], after decreasing the temperature, the amplitude of pulses are reducing and achieving a higher trapped magnetic field of 4.33 T at the centre of a SmBaCuO bulk [70].
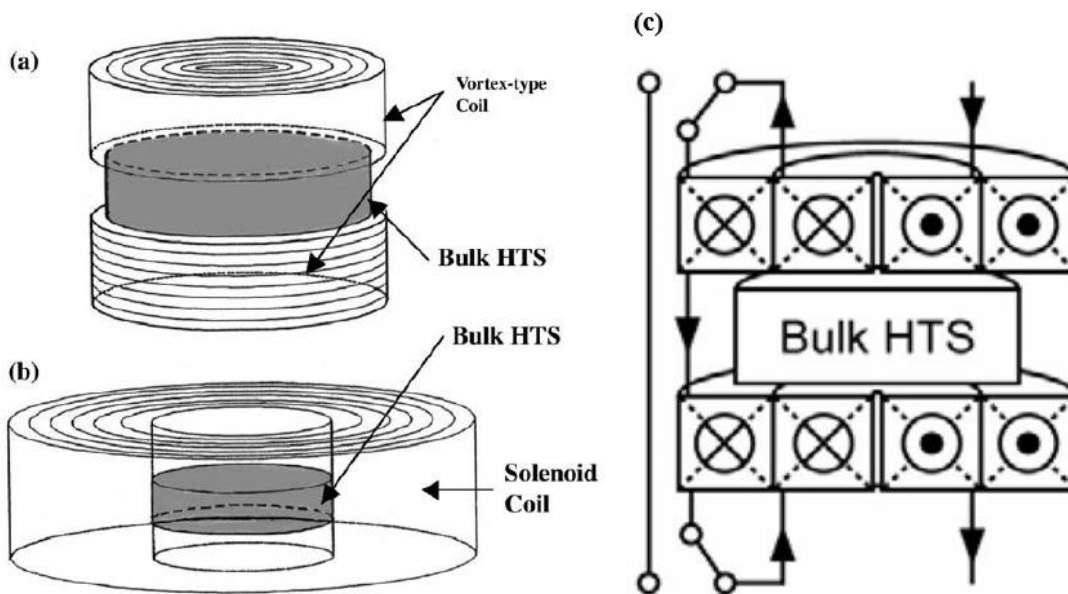
Figure 2.20: Schemes of the arrangement of magnetisation coils used for the PFM of HTS. (a) split-type vortex coils [76]. (b) Solenoid coil [76]. (c) Controlled magnetic density distribution coils (CMDCs) [77].

In terms of magnetisation coils, three different structures have been investigated by experiment and simulate [64, 76-82]. The most commonly used one is the solenoid coil on account of its simple structure [64, 81, 82]. The split-type vortex coils show enhancement on trapping fields and the magnetic flux starts to trap on the bulk centre [76, 80]. Furthermore, the heat generation

during the flux intrusion on the periphery of the bulk is reduced [79]. As for Controlled magnetic density distribution coils (CMDCs), the coils composed of inner vortex coil and outer solenoid coil as shown in Figure 2.20 (c). The dimension of CMDCs is the same as a normal split-type vortex coil that is same or larger than samples. The pulsed current is applied to both solenoid and split-type vortex coils under serial connection. The CMDC can also be utilized as an armature coil in the motor [77]. There are gradient applied fields generated by CMDCs with peak values in the centre, which can reduce heat generation during PFM and increase the trapped field and trapped flux. The larger the gradient, The higher the trapped field [78]. There has also been work introducing ferromagnetic materials (like an iron yoke) within the magnetising circuit to trap higher fields [83].

2.4.2 HTS trapped field magnets (TFM)

Both static and dynamic magnetisation leave remnant currents or fields in HTS, which makes the HTS as a permanent magnet. Considering the sample volume, the usages of HTS bulks or stacks are space and cost savings. Compared to HTS bulks, stacked tapes present better performance on uniform current density and thermal stability, especially during pulse-field magnetisation.

2.4.2.1 Bulks

Well-connected, single-grain bulks fabricated by type-II HTS materials can trap fields more than 10 times higher than that of conventional magnets [18, 65]. A great number of experimental or simulating works has been proposed for trapping-field analysis on bulk [18, 64, 67, 69-77, 79-82, 84-91]. The volume fraction of HTS has been largely increased to over 90% owing to the technical development on top-seeded melt growth (TSMG). The world record trapped field is 17.6 T at 26 K generated by two superconducting bulks made of composition $(RE)Ba_2Cu_3O_{7-\delta}$ (ReBCO) [18]. It was also shown in research that the trapped fields for standard, non-irradiated sample at liquid nitrogen-boiled temperature (77 K) are up to 1.5 T for YBCO, 2 T for (RE)BCO and 3 T for Gadolinium barium copper oxide (GdBCO) bulks [92].

There are inevitable drawbacks for HTS bulks. During the magnetizing process, tensile stresses occur in the sample due to the stored flux density gradient and may exceed the mechanical tensile strength of the material which results in cracks in the fragile ceramic HTS. The cracks can also be detected at 20 K to 30 K resulting from the flux jump owing to thermomagnetic instabilities [93]. To reinforce the mechanical and pinning properties, Ag and Zn can be added into the bulk during manufacture [93, 94]. It is also proved that telescoping the bulk disks in steel tubes or drilling small holes into the centre of the bulk gives rise to improvement on tensile stresses and thermal stability of bulks [85, 93]. However, it is still unavoidable for most of the experiment that the sample bulk is easy to be damaged when trapping very high fields (over 10 T). Even for the previous world records, the two bulks need to operate with shrink-fit steel [18] or resin impregnation with a carbon fibre wrapping [85].

2.4.2.2 Stacks

Superconducting stacks utilized as TFMs can trap fields higher than the superconducting bulks in recent research [19]. The world record trapped fields now is 17.7 T for a hybrid stack which combined the SuperPower stacks and American Superconductor (AMSC) stacks at 8 K [19]. Compared to HTS bulks, HTS stacks have a great number of advantages, especially, for trapping very high fields. First of all, the HTS stacks consist of HTS tapes which are relatively cheaper than bulks. It is more flexible to constitute different configurations and shapes [95]. Secondly, since the high volume fraction of metallic substrate, the tensile strength is quite high, there is no extra mechanical reinforcement required for stacks to withstand Lorentz forces at high trapped fields [19]. Last but not least, for some of the HTS tapes, the silver layer is able to deliver thermal stability for the inside superconducting layer which is beneficial to conquer flux jumps, dissipate the unwanted eddy current heating generated during a pulse and supress hotspots [96]. The timeline for trapped field records of HTS stacks can be found in Figure 2.21. Using HTS stacks as permanent magnets in electric motors has been proposed but not a lot [97], which needs to be further investigated.
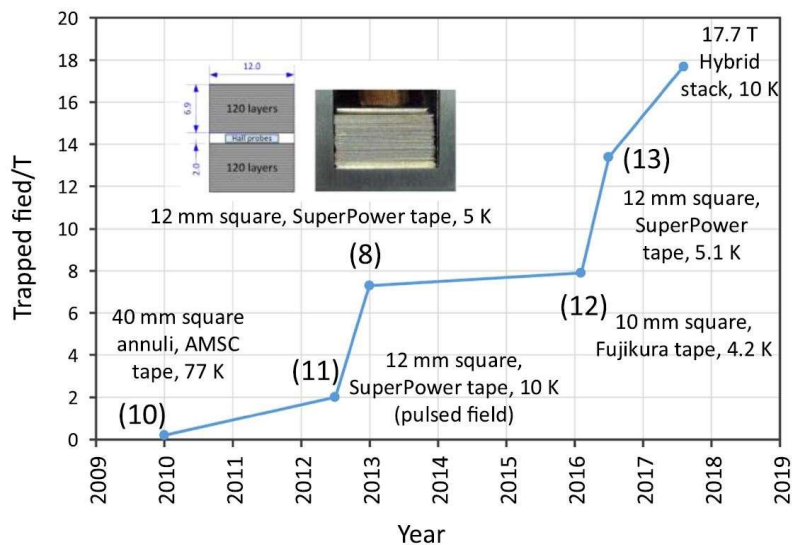
Figure 2.21: Timeline of trapped field records for stacks of HTS tape [19].

2.4.3 Application on HTS rotating machines

Thanks to the higher current densities, lower losses and higher field produced, HTS magnets can be utilized in industrial, medical and chemical domains, such as nuclear magnetic resonance (NMR) spectroscopy or magnetic resonance imaging (MRI) systems, magnetic levitation, magnetic bearings and flywheels, superconducting mixers, magnetic resonance microscopes, HTS rotating machines (motors and generators) and so on [21].

It was the copper windings that adopted on rotors and stators of rotating machines, which increase the resistive loss, unwanted energy and general expense. Due to the characteristics of zero to near - zero resistance, the HTS materials could reduce the electrical energy loss and improve the efficiency. Moreover, the huge size and weight of power components and machinery can be reduced, which can save the overall cost in building the electrical system.

HTS rotating machines tend to be used in transportation applications, such as naval, wind turbines and ship propulsions [98, 99]. As we know, the power of a rotating device can be calculated by multiplying the torque (T_t) and the rotational speed (ω), as expressed in equation 2.25. The torque of an electrical machine is proportional to the armature electric loading (A_e), the peak airgap flux density (B_{air}), and the volume enclosed by the airgap (V) [98]:

$$P = T_t \times \omega \qquad (2.25)$$

38

$$T_t \propto B_{air} \times A_e \times V \tag{2.26}$$

Appling HTS bulks in HTS rotating machines has been proved to be an effective way to minimize the volume and weight of the synchronous motor and supply a large torque and power. The general pros and cons of HTS machine are listed in Table 2.2 [12, 100]:

A great number of novel prototypes or design concepts with HTS rotors and stators has been developed, for instance, the axial-gap and radial-gap type synchronous rotating machines [20, 86, 101-112], the reluctance rotating machines and hysteresis machines. Most of the developed machines are adopted HTS TFM (especially bulk) or coils as the DC field magnets or windings located on the rotor and copper AC windings located in the stators [8, 86, 104, 108]. Compared to HTS coils, magnetized TFMs are able to supply a more persistent and compact source of field. The rotating HTS TFMs produce a magnetic field in the copper armature winding. The magnitude of this field is typically twice than that of a conventional motor [8, 110]. A schematic illustration of a synchronous HTS motor is presented in Figure 2.22. The characteristics of motors adopted HTS bulks as pole-field magnets are summarised in Table 2.3. It reveals that the using of melt-growth $GdBa_2Cu_3O_y$ (Gd-123) HTS bulks (fabricated by the quench and melt growth method) can dramatically increase the maximum trapped fields of the eight poles, as well as the rotation speed, torque and output power of the motor.

Table 2.2: Advantages and challenges of HTS synchronous machine

Advantages	*Challenges*
High efficiency	HTS material
More compact, lighter	Cryogenic cooling and vacuum technology
Low synchronous reactance and small load angle	*In situ* magnetisation
Better transient stability and grid stability, high overload capacity	AC loss from high-power density stator winding
Low noise and vibration (no armature teeth)	Expense
Low harmonic content	
Superior negative sequence capability	
Higher rotating speeds limits	

Further investigation of HTS armature windings has been stated [20, 110]. The fully HTS machine becomes realisable and has been proposed by several groups [15-17, 107, 110, 113, 114]. Compared to partially HTS machines, the fully HTS machine is able to accomplish higher electric loading from HTS AC windings and smaller air gap since the DC and AC windings operate at the same temperature [20]. However, there are still challenges in seeking HTS TFMs with higher trapped fields and lower AC losses on armature winding. HTS excitation coils might not be a proper choice to replace the conventional copper coils to magnetise the TFMs by field cooling method, which gives rise to higher costs and risky prospects compared with using copper stator coils as pulse magnetisation coils. Therefore, the thesis will pay more emphasis on the pulse field magnetisation on HTS TFMs to promote the trapped field ability of TFMs and methods to reduce the AC losses on armature windings.
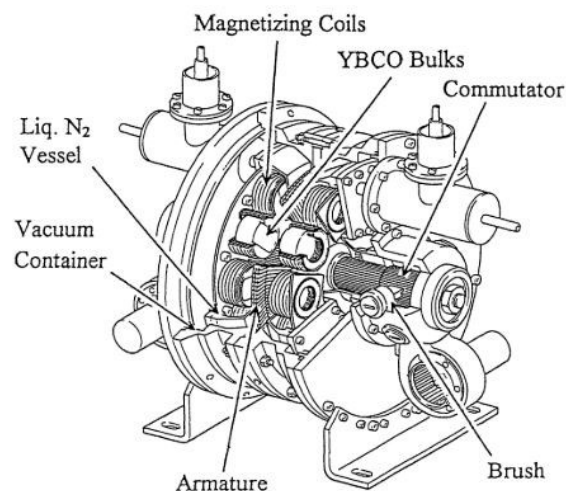
Figure 2.22: Schematic illustration of the construction of a synchronous HTS motor using HTS bulk as field magnets [102].

Table 2.3: Characteristics of motors using different HTS bulks as pole-field magnets

	YBCO bulks [115]	GdBCO bulks [86]	Melt-growth GdBCO bulks [104]	Melt-growth GdBCO bulks [104]
Number of poles	8	8	8 (single rotor)	8 (twin rotor)
Bulk number/ diameter/thickness	8/ 60 mm/ 15 mm	8/60 mm/19 mm	8/60 mm/20 mm	16/60 mm/20 mm
Maximum Trapped field	0.6 T	0.5 T	1.0 T	0.7 T
Rotation speed	600 rpm	720 rpm	850 rpm	760 rpm
Torque	25 N m	44.2 N m	132.7 N m	212.3 N m
Output power	1.5 kW	3.1 kW	10 kW	16 kW
Operating temperature	27 K	77 K	77 K	77 K

2.5 AC losses

A superconductor is usually perceived to be a conductor which can carry electrical current without resistance. However, in general, a superconductor is simply a conductor which has a very low resistance if operated under proper conditions. At low frequency of electrical power applications, resistance arises in ordinary type-II superconductors because of flux flow and flux creep. The mechanism is that the pinning force continuously prevents flux lines from entering or leaving the superconductor as witnessing an AC magnetic field. Type-II superconductors are of much more technological interest since they can carry more current in larger magnetic fields, whereas, they also have losses because electric fields can be produced inside. Hence, when carrying an alternating current or in an AC electromagnetic field, superconductors present some electromagnetic energy losses, namely AC losses [34].

AC losses within the superconductor need to be maintained to a very low level since they occur at a low temperature required to keep superconductivity. To remove the heat that occurs in that low temperature, it requires much more refrigerator energy power. Therefore, AC losses should be low enough to avoid energy waste and detrimental effects on the extra investment in the superconductor.

AC losses of superconducting composites can be classified either by external sources for the losses (magnetic field loss and transport current loss) or by natures of the losses (hysteretic loss, eddy current loss, coupling loss). To calculate the total losses in the superconductor, the former classification is widely used in many applications.

Magnetisation loss (Q_m) is the power dissipated in the superconductor when an alternating magnetic field is applied to the superconductor. The energy source comes from the magnetic field. Transport current loss (Q_t) is the power that is delivered by a transporting current (I) resourcing from the power supply. The voltage, V, along the sample is a measure for the dissipated power. The total power dissipated is $Q_{total} = Q_m + Q_t$. Both losses can occur in superconducting applications with AC magnetic field or current applied.

When the operating current is lower than critical current I_c, the vortex is completely pinned in superconductors which means hysteresis loss is generated and dominates the AC losses. When the operating current exceeds I_c, the superconducting vortex can move freely, and flux flow loss dominates the AC losses. This assumption makes calculations of AC losses much easier [3]. More information about the nature of AC losses and other losses will be illustrated below. The schemes for each loss are presented in Figure 2.23.
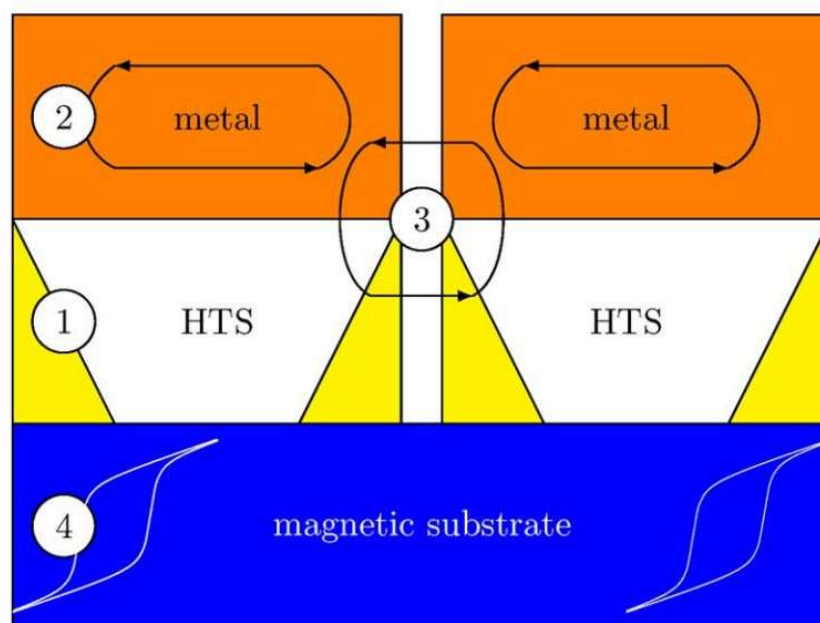
Figure 2.23: Schemes of losses contributions in a ReBCO HTS tape. (1) Hysteresis losses in the superconducting layer; (2) eddy current losses in the normal metal stabilizer; (3) coupling losses between different filaments and (4) ferromagnetic losses in the magnetic substrate (if applicable) [44].

2.5.1 Hysteresis loss

Hysteresis loss per cycle like Figure 2.23 (a) shows is independent of frequency arising in a superconductor under a varying magnetic field. This loss is caused by the irreversible magnetic properties of the superconducting material due to hindering flux line from free motion by flux pinning. For a single superconducting filament or bulk, AC losses are mainly hysteresis losses. Hysteresis loss becomes higher for stronger pinning, which means the larger the critical current of a hard type-II superconductor, the larger the hysteresis losses [22]. The hysteresis loss can be defined by the area of the hysteresis loop shown in Figure 2.16 which is the energy dissipation during a magnetisation cycle described by:

$$Q = \int M \cdot dH = \int H \cdot dM \qquad (2.27)$$

When an alternating transport current is supplied to a superconductor, hysteresis losses occur due to the self fields generated by the transporting current. In transport losses, hysteresis losses occupy a large part, which is quite significant.

To reduce this loss the superconductor should better to be divided into many fine filaments and the matrix of normal metal is used to protect these fine filaments [116].

2.5.2 Eddy current loss

Eddy current loss arises in the normal matrix of a composite superconductor or the structural material when exposed to a varying magnetic field, either from an applied field or from a self field. Owing to the eddy current, the ohmic energy dissipation can be of significance if the magnetic field is perpendicular to the tape. If there are no superconducting filaments and only a normal conducting matrix exists, then only normal eddy current loss exists. However, if there are superconducting filaments in the current path of the eddy current, the resistance of the current path is greatly reduced, therefore the circulating eddy currents increase, and AC loss also increases. This enhanced eddy current loss, as noted above, is called coupling current loss.

It must be noted that coupling current loss is also sometimes called "simply eddy current loss" when the normal eddy current loss inside the metal matrix can be ignored [34].

The idea of reducing the eddy current losses are increasing the effective resistivity of the matrix, reducing the thickness of metal stabilizer, or applying fields slowly.

2.5.3 Coupling loss

Coupling loss could be a vital problem in multi-filament superconductors. When the frequency of the applied field increases, the filaments of superconducting composite begin to "couple". Here, the term "couple" is used to describe currents which have paths which are partially within the superconducting filaments and partially in the matrix. Two filaments in a strand, as well as two non-insulated strands in a cabled conductor, constitute a loop for induced currents under a perpendicular time-varying field. Even though the losses originate exclusively with the normal conducting regions of the path, the losses from the "coupling currents" are far greater than normal eddy currents. The coupling current loss affects the stability, that is, the ability of the superconductor to withstand magnetic field transients [34].

To reduce the linked area, the filament bundles can be twisted and the strands are cabled with tight pitches, leading to transposition with respect to the perpendicular field [23].

2.5.4 Ferromagnetic loss

Ferromagnetic losses play important roles in the AC loss characteristics as there are hysteresis cycles in the ferromagnetic substrate layer. When an AC transport current or magnetic field applies to an YBCO tape, the parallel component of the self field or applied external field will magnetise and demagnetise the substrate, generating a large amount of ferromagnetic loss. Moreover, the magnetic permeability of the substrate will be affected by the magnetic field inside the substrate. As a result, the AC loss characteristics of the superconducting layer will be influenced as well.

Ferromagnetic losses can be eliminated by avoiding ferromagnetic materials. For a HTS cable, the substrate layers should be better able to face inside of the cable [117].

2.5.5 Flux flow loss

Theoretically, there should be no loss under DC conditions, however, when the coil approaches the critical state, there will be flux-flow and flux-creep related losses, which can be estimated by multiplying the coil voltage and current. As the operating current exceeds critical current I_c, the contribution of flux flow loss becomes more significant for AC losses. There is an overlap between the hysteretic loss and flux flow loss due to the pinning strength distribution amongst independent pinning centres, which leads to a smooth transition from hysteretic loss to flux flow loss [3].

2.5.6 AC losses reduction

A great number of groups have been working on the AC losses mitigation since the efficiency of practical superconducting devices need to be improved. From the material point of view, the development of manufacturing techniques can considerably improve pinning effect, grain structure or boundaries, etc. However, in this part, part of the existing methods of AC loss reduction for the manufactured superconductors will be introduced.

2.5.6.1 Multi-filament superconductor

Using multi-filament tapes is an effective way to reduce AC losses and remnant fields, as found by Brandt [118], the magnetisation loss follows a square law with the width of the superconductor. The multifilamentary tape is striated using a variety of techniques. The most popular methods are laser scribing or chemical etching. The improvement of manufacturing techniques has allowed the use of narrower filaments and results have proved that the thinner the individual filaments, the lower the undesirable ac loss. Additionally, striated HTS can also reduce current inhomogeneity caused due to screening currents, which are crucial to applications such as NMR and MRI. More details about this part will be shown in chapter 6.

2.5.6.2 Roebel cable

Ludwig Roebel was the first person who proposed the concept of Roebel transposition in 1914. Until now Roebel cable has been considered as one of the most promising methods to carry

large current density and reduce the AC losses. If we simply stack single tapes together to develop a large–current bundle, currents will be transported imbalance, which can give rise to serious problems and affect the performance of the coated conductors [119]. The detailed geometry and schematic view of a Roebel cable can be seen in Figure 2.24. In high power electrical devices such as superconducting transformers and fault current limiters, it is desirable to assemble the YBCO coated conductors to increase current-carrying capacity [120]. Roebel cable is a promising solution for high current capacity applied in various applications. However, it is formidable to reduce AC losses in high current YBCO conductors. Much work has focused on creating striated strands in order to diminish the hysteresis loss [121]. The results are encouraging. There is no significant degradation of the critical current on single strand after striation process. Effective AC loss reduction due to the striation process was confirmed, which is more obvious at high field amplitude [121].
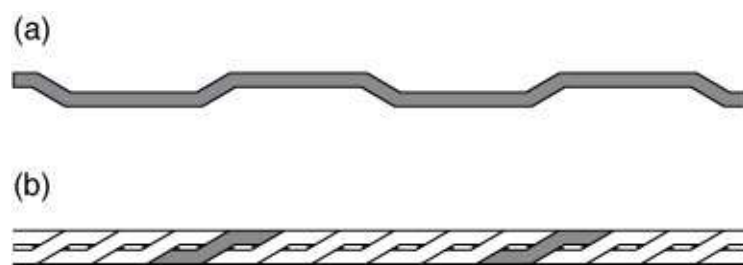
Figure 2.24: Schematic views of the Roebel cable: (a) strand and (b) assembled strands [119].

2.5.6.3 Twisted wires

Twisted superconducting wires are used to avoid flux linkage between the filaments [122, 123]. It is effective to degrade AC loss against an AC transverse magnetic field [124]. Ideally, the wires would be fully transposed, where each wire swaps places with every other wire along the length, so that averaged over the length, no net mutual flux linkage occurs. However, twisting the filaments severely will damage the microstructure, the evolution of texture, and eventually decrease the critical current. Due to the nature of the geometry of the high-temperature

superconductors, having a large aspect ratio, the damage can be even greater than with other superconductors [34, 125].

2.5.6.4 Magnetic shielding flux diverter

Magnetic materials can be used to manipulate the magnetic flux in a superconductor to reduce the AC losses. Using a magnetic cover for individual filaments in a striated YBCO conductor is capable of decoupling the filaments and reducing losses [125]. Regarding the flux diverter approach, the use of external flux diverters modifies the magnetic flux profile of the conductor(s) in order to achieve a reduction in AC loss without modifying the original conductor. Results have been shown that in a YBCO-based superconducting coil, there is a reduction in AC loss without any change in the critical current, which is a promising result for this technique [125].

Chapter 3   Numerical modelling for HTS stacks

As an effective tool, numerical modelling is capable of solving complicated computations with long algorithms and predicting the electromagnetic performance of superconducting systems, in order to optimise the design for applications. Considering the significant impact of temperature during the pulsed field magnetisation (PFM) process, it is essential that an electromagnetic model is coupled with a temperature model, to analyse the behaviour of currents and magnetic fields with thermal alternations. A thermal-coupled model requires large computation time and thus, a more efficient model is of importance.

This chapter will introduce the fundamental models used during the simulation work, which were the basis for further analysis. A thermal-coupled 2D model using the *H*-formulation method for the HTS stack with a magnetic substrate will be introduced in section 3.1. A *T-A* formulation model that involved the specific substrate and stabilisers will be presented in section 3.2. Comparison results using two formulations for ZFC of HTS stacks will be analysed in section 3.3. A thermal-coupled *T-A* formulation model will be proposed and explored in section 3.4. The simulation results of the new model will be compared with the *H*-formulation model for PFM of HTS stacks in section 3.5.

3.1 2D model using *H*-formulation for HTS stacks

One of the inevitable drawbacks facing PFM is the temperature rise during the fast movement of penetrating flux. Thermal analysis is one of the key factors in the simulations. A 2D Cartesian model was built in COMSOL 5.2, which was electromagnetic-thermal coupled and based on *H*-formulation. 2D *H*-formulation models of stacks have previously been validated by experiments [126]. The fundamental implementation of *H*-formulation is described in section 2.3.2. The temperature-dependent models will be described in section 3.1.2, which will

show the implementation of heat transfer in the modelling. It is crucial to consider temperature-dependent parameters and material properties for different structures and types of stacks.

3.1.1 Geometry, parameters and mesh

An overview of the geometry of the stacks in COMSOL 5.2 is shown in Figure 3.1. The configurations of the AMSC (with magnetic substrate) and SuperPower tapes (without magnetic substrate) used during this research are presented in Figure 3.2. The framework uses Maxwell's equations combined with the E-J power law to solve different variables. The governing equations are listed in Table 3.1.
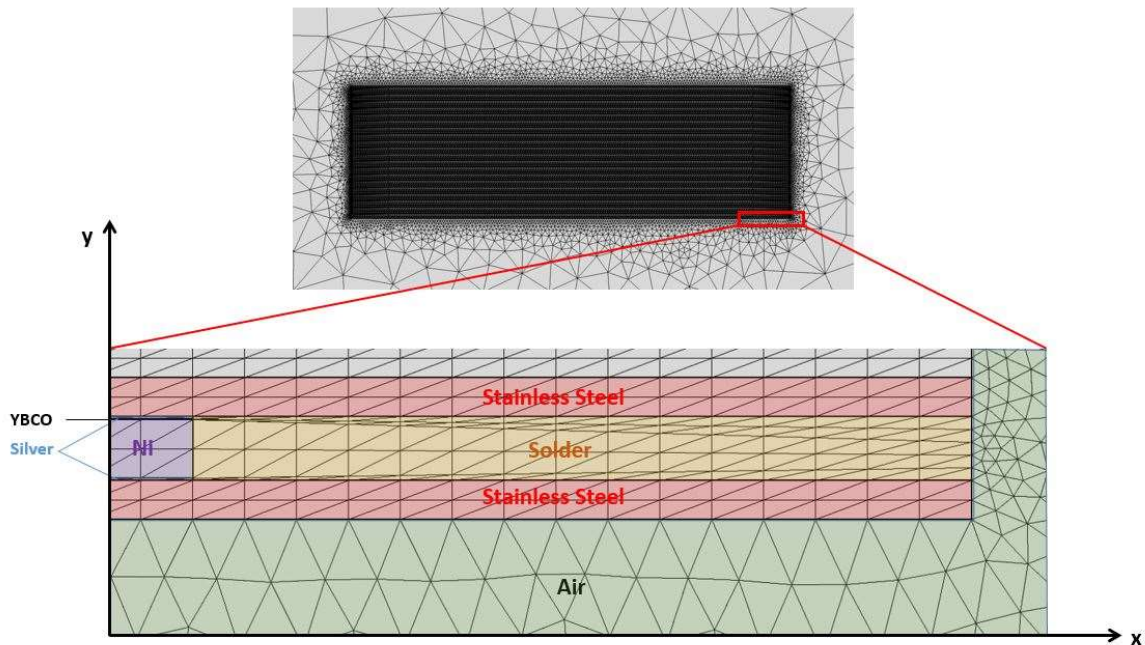
Figure 3.1: Geometry and typical finite element mesh of a 20-layer AMSC stack in COMSOL 5.2. The bottom figure shows the zoomed in mesh with all the composing layers of the stack and air surrounding.
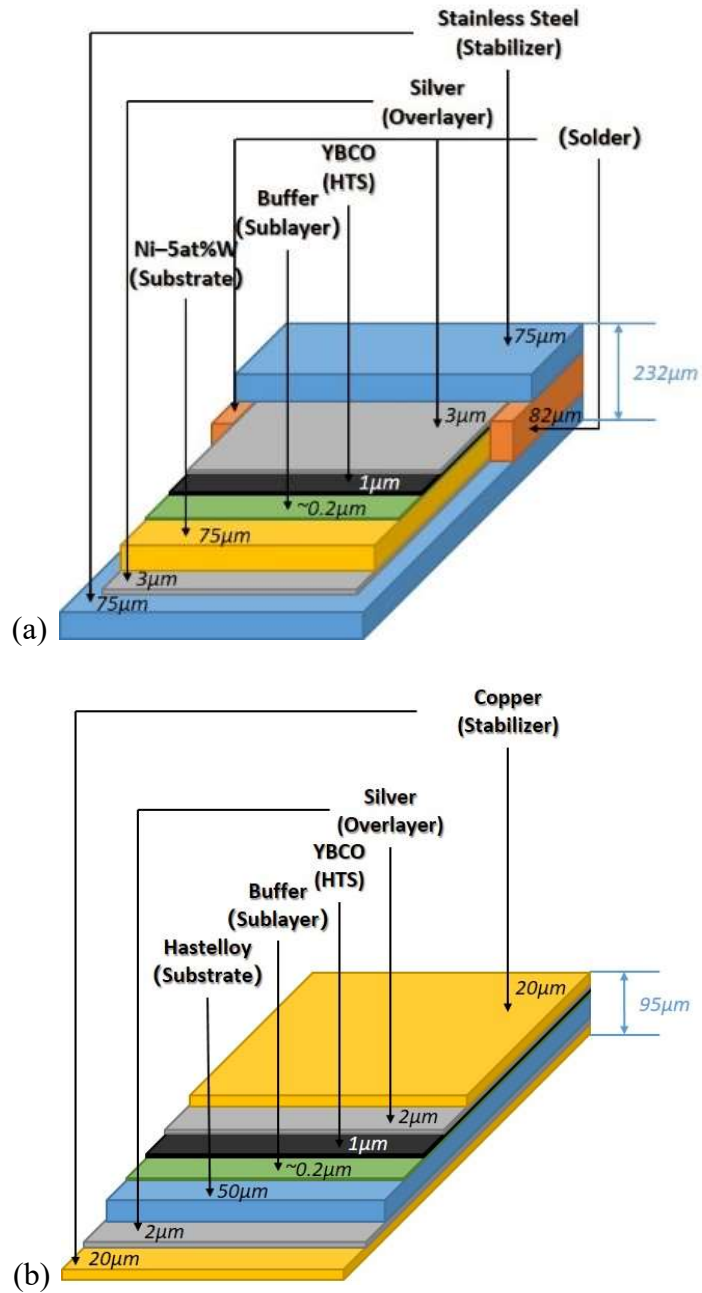
Figure 3.2: Composition and geometry of the 12 mm tape made from (a) American Superconductor (AMSC) with a magnetic substrate and (b) SuperPower without a magnetic substrate.

Table 3.1: Governing equations of 2D Cartesian model using H-formulation

Cartesian model

Faraday's law	$$\begin{bmatrix} \dfrac{\partial E_z}{\partial y} \\ -\dfrac{\partial E_z}{\partial x} \end{bmatrix} = -\mu_0\mu_r \begin{bmatrix} \dfrac{dH_x}{dt} \\ \dfrac{dH_y}{dt} \end{bmatrix}$$
Ampere's law	$$J_z = \frac{\partial H_y}{\partial x} - \frac{\partial H_x}{\partial y}$$
E-J power law	$$E_z = E_0 \left(\frac{J_z}{J_c}\right)^n$$
Partial differential equation (PDE)	$$\begin{bmatrix} \dfrac{\partial\left(E_0\left(\dfrac{\frac{\partial H_y}{\partial x}-\frac{\partial H_x}{\partial y}}{J_c}\right)^n\right)}{\partial y} \\ -\dfrac{\partial\left(E_0\left(\dfrac{\frac{\partial H_y}{\partial x}-\frac{\partial H_x}{\partial y}}{J_c}\right)^n\right)}{\partial x} \end{bmatrix} = -\mu \begin{bmatrix} \dfrac{dH_x}{dt} \\ \dfrac{dH_y}{dt} \end{bmatrix}$$
Dirichlet boundary condition	$$\begin{cases} H_x = F_x(t) \\ H_y = F_y(t) \end{cases}$$

In a 2D Cartesian model, the superconductor length is assumed to be infinite in the *z* direction. Different layers are considered with actual thicknesses and corresponding materials. The values of the parameters used in the COMSOL models are listed in Table 3.2. For HTS, the range for the *n* value parameter is commonly from 5 (strong flux creep) to 50 (critical state model approximation) [127].

Since only the magnetic field of the *y*-axis was considered, the Kim model equation (presented in section 2.2.3) was used to define the relationship between the critical current density and magnetic field as:

$$J_c(B,T) = \frac{J_{c0}(T)}{1+\frac{B}{B_0}}$$

(3.1)

Where B_0 is the flux density constant, which will be one of the parameters analysed in section 4.1.

Table 3.2: Description of the tape configuration and values of the parameters used in the modelling.

Parameter	Description	Value
μ_0	Vacuum permeability	$4\pi\times10^{-7}$ H/m
n	n-value in E-J power law	8, 21 and 35
E_0	Electric field constant in E-J power law	1 µV/cm
B_0	Flux density constant in equation 3.1	0.4, 1, and 4 T
B_m	Applied pulsed field amplitude	0.3-4 T
T_0	Equilibrium temperature of stacks	30 K or 77 K
T_c	Critical temperature of stacks at $B = 0$	92 K
t_0	Pulsed field ramp-up time	10 ms
t_d	Pulsed field ramp-down time	50 ms
k_{ab}	Theoretical modelled thermal conductivity in the ab-plane	Figure 3.5
k_c	Theoretical modelled thermal conductivity in the c-plane	Figure 3.5
$k_{other}(T)$	Thermal conductivity as a function of temperature for silver, copper, nickel, stainless steel and Hastelloy.	Figure 3.5
C_{Ni}	Heat capacity for Nickel	440 J/(kg×K)
$C_{other}(T)$	Heat capacity as a function of temperature for YBCO, silver, copper, stainless steel and Hastelloy	Figure 3.6
ρ_{Ni}	Electrical resistivity for nickel	2.68×10^{-7} Ω×m
$\rho_{other}(T)$	Electrical resistivity as a function of temperature for silver, copper, stainless steel and Hastelloy	Figure 3.7

The tape shown in Figure 3.1 is manufactured by AMSC (type 8602). According to previous research, smaller mesh elements give rise to more accurate results but a longer solving time. To achieve more precise results, each layer of the tape was meshed with mapped elements. The thickness of the nickel and stainless steel layers were divided into two parts in the y-axis. There were five divisions for the solder layers and one division for the YBCO and silver layers. For the width of the tape, there were 180 elements for the stainless steel layers, 150 elements for the silver and YBCO layers and 15 elements for both sides of the solder layers. Furthermore,

the mapped square elements were converted into triangular elements. The air domain was meshed with free triangular elements. The mesh contained 76,448 domain elements and 20,610 boundary elements for a 20-layer AMSC stack.

The boundary for the air domain was almost ten times larger than the stack thickness and width. For the electromagnetic parts, a Dirichlet boundary condition was set for all the edges of the air domain in the y-axis direction, which was for the uniform applied external magnetic field. The applied field could vary for different forms of pulses. The most common applied pulse is expressed by equation 2.24.

Since there is no magnetic substrate in the SuperPower tape, the relative permeability in each layer is constant and set to one. However, for the AMSC tape, the relative permeability for the nickel layer is not constant, since it is altered by a magnetic field. According to the research presented in [128], the relative permeability μ_r of the substrate, as a function of the applied field, is shown in Figure 3.3.
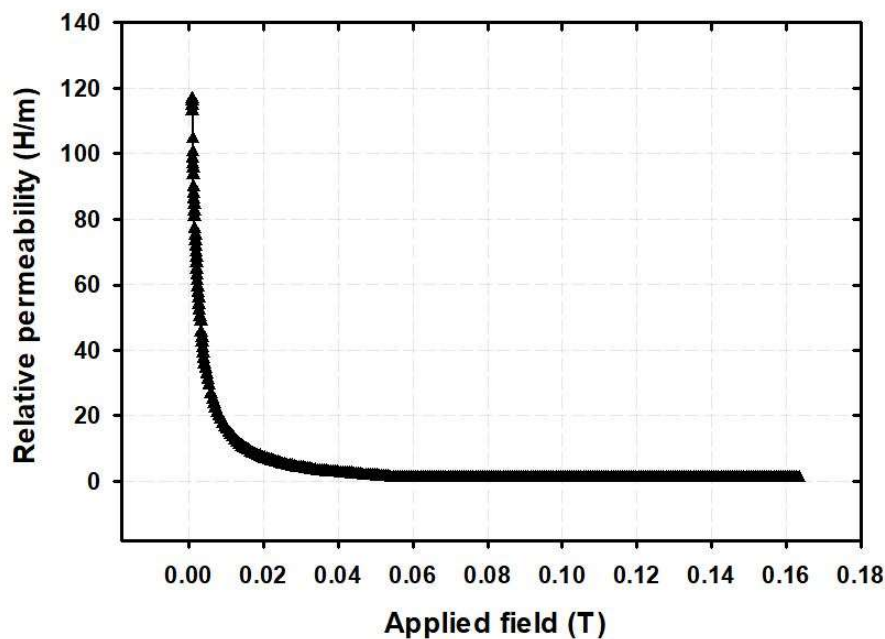
Figure 3.3: Relative permeability μ_r of the substrate as a function of the applied field $\mu_0 H$ [128].

3.1.2 Thermal coupled model

3.1.2.1 Heat transfer

As previously discussed in section 2.1.1.3, temperature can affect the critical current dramatically, especially when the temperature surges above the critical temperature or experiences a sudden increase. It is inevitable, therefore, to analyse and discuss the influence of temperature change and heat transfer on superconductors and other cases. The dynamic process of temperature change is capable of being simulated in the *Heat Transfer* module in COMSOL.

The heat transient equation given by Joule dissipation is:

$$Q = E_{norm} \cdot J_{norm} = \rho C_p \frac{\partial T}{\partial t} - \nabla \cdot (-k\nabla T) \tag{3.2}$$

where Q is the power density dissipated by the heat source; ρ is the density; C_p is the heat capacity; and, k is the thermal conductivity.

For the simulation of superconductors, the *Heat Transfer in Solid* module is widely used, where *Initial Values*, *Thermal Insulation*, *Heat Source* and *Boundary Conditions* need to be set according to the practical requirements.

Since the stack can be attached to a cold head or immersed in a liquid cryogen, there are two types of boundary conditions used in this thesis. One is the Dirichlet boundary condition (equation 3.3) which can be utilized when the superconductor is connected directly or indirectly to a cold head of a given temperature T_0. The other is the Neumann boundary condition (equation 3.4), it represents the superconductor is cooled by a liquid cryogen as the cooling power per unit area q_0 (W/m^2) is known.

$$T|boundary = T_0 \tag{3.3}$$

$$\lambda \frac{\partial T}{\partial n}|boundary = q_0 \tag{3.4}$$

3.1.2.2 Thermal coupling of heat transfer and electromagnetic parts

The *Electromagnetic* module and *Heat Transfer* module need to be run at the same time due to the strong interaction between the simulating results from each module. The input of the *Heat Transfer* module $E_{norm} \cdot J_{norm}$ is generated by the *Electromagnetic* module. The temperature also contributes to the input to the *Electromagnetic* module and influences the thermal variables such as the heat capacity C_p, the thermal conductivity k and the temperature-dependent critical current J_c. The two modules are fully coupled at each time step to produce and export more accurate results.

The temperature-dependent critical current J_c can be determined by two methods [64, 129]:

$$J_c(T) = J_{c0} \cdot \left(\frac{T_c - T}{T_c - T_0}\right)^\alpha \tag{3.5}$$

$$J_c(T) = \alpha \left\{1 - \left(\frac{T}{T_c}\right)^2\right\}^{\frac{3}{2}} \tag{3.6}$$

where J_{c0} and T_0 are the critical current density and critical temperature under a self-field, respectively; T_c is the critical temperature at $B = 0$; and, α is a constant value, which can be adopted by the field dependent critical current density $J_c(B)$ at 77 K. Both methods have been proved accurately [64, 130]. In this thesis, equation 3.6 will be used.
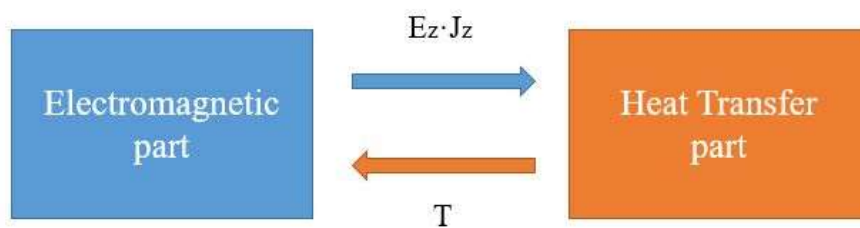
Figure 3.4: Coupling between the *Electromagnetic* and *Heat Transfer* modules in COMSOL.

3.1.2.3 Thermal parameters

Temperature is an important aspect in the models used for investigation in this research. Different temperature-dependent material properties and parameters are considered including the thermal conductivity k, heat capacity C_p, electrical resistivity ρ and critical current density J_c for each material layer. The thermal conductivity, heat capacity and electrical resistivity are material properties, which are different for each material. The thermal conductivity of a superconducting layer needs to be considered not only in the *ab*-plane but also in the *c*-axis. For stacks without a magnetic substrate (SuperPower), the data based on experimental results was obtained from [78]. The related materials are superconductor, copper, silver and Hastelloy. The data graph from another paper [131] shows the values of the parameters for stacks with a magnetic substrate (AMSC) changing with temperature. The related materials are superconductor, stainless steel (SUS 316L), silver and nickel. The values of thermal conductivity, heat capacity and electrical resistivity changing with temperature are presented in Figure 3.5, Figure 3.6 and Figure 3.7, respectively.

For the heat transfer part, the "Thermal Insulation" is set on the outer edges of the tapes. The heat initial value is set to be the original cooling temperature T_0. If the temperature is higher than T_0, the stack will be cooled down as we assume the bottom surface of the stack connected to the cold head.
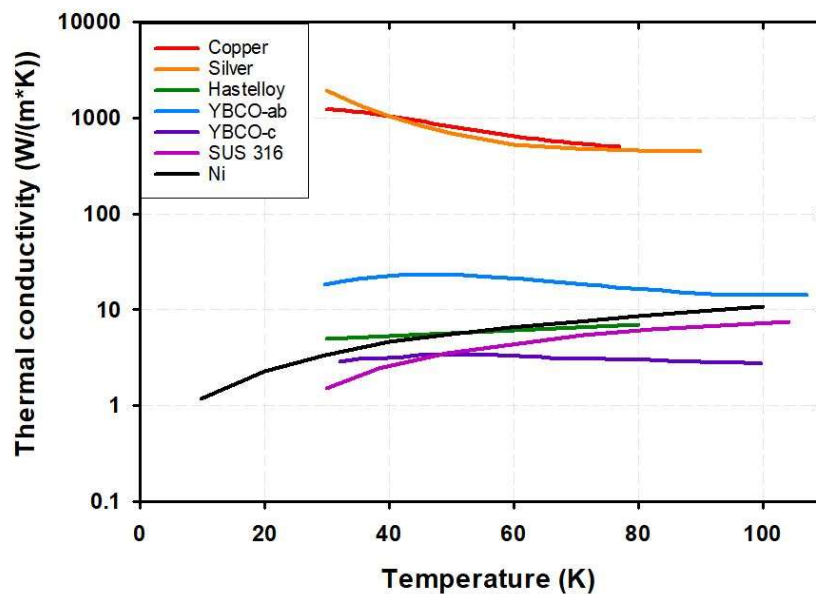
Figure 3.5: Thermal-dependent properties of thermal conductivity for different materials in the SuperPower and AMSC tapes. YBCO-ab and YBCO-c represent the parallel and perpendicular directions to the *ab*–plane, respectively [78, 131].
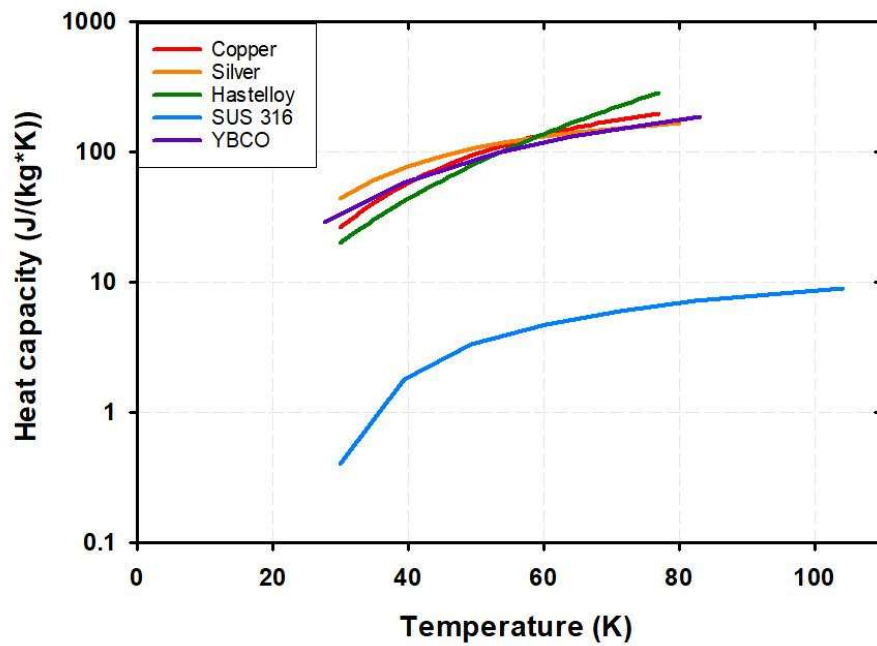
Figure 3.6: Thermal-dependent properties of heat capacity for different materials in the SuperPower and AMSC tapes [78, 131].
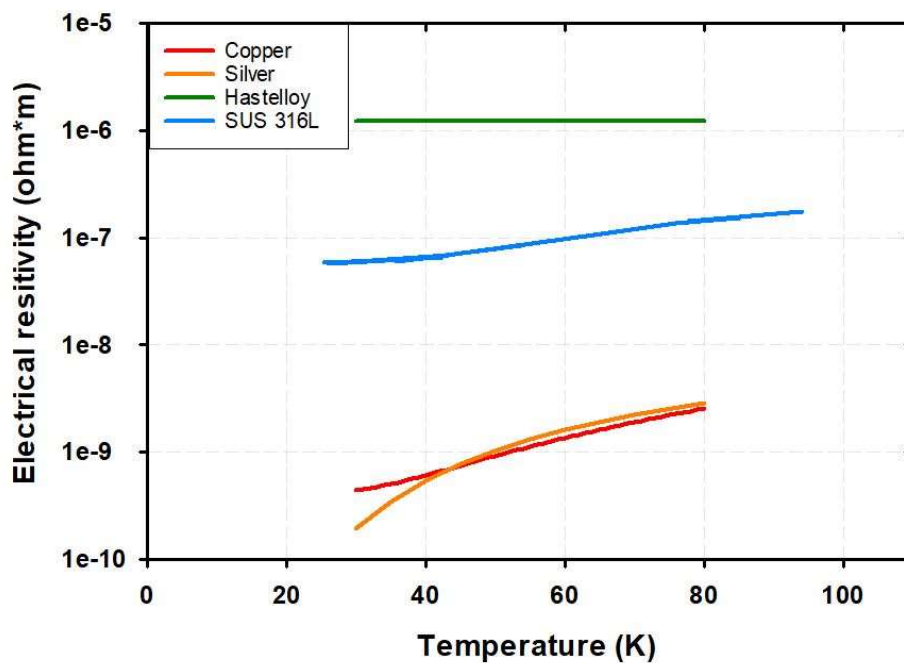
Figure 3.7: Thermal-dependent properties of electrical resistivity for different materials in the SuperPower and AMSC tapes [78, 131].

3.1.3 Experiment validation

Experimental testing was conducted to validate the modelling results. Although HTS stacks are more homogeneous and uniform compared with HTS bulks, it is not easy to characterise the material properties reliably. To achieve more accurate results, most of the parameters used in the models were based on real experimental results from the database in [132, 133]. The field dependence of the critical current for AMSC and SuperPower tapes are shown in Figure 3.8.

Since the temperature changed considerably and is not easy to be measured during the swift PFM process, only trapped field results were compared. The simulation results for the SuperPower stack have been previously validated by Zou *et al.* [126]. She adopted 2D electromagnetic-thermal coupled model using the *H*-formulation. Anisotropic magnetic field and temperature dependent *Jc(B,T)* was considered using the elliptical equation and temperature dependent parameters, which could be generally valid to define the characteristics of the anisotropic critical current density of SuperPower tapes without artificial pinning [43].

The modeling frameworks are the same as the ones discussed in section 3.1. The experimental test rig will be thoroughly discussed in the section 5.3. The AMSC tape was cut into 12 mm × 12 mm squares and stacked tightly. The stack compared in both simulations and experiments was composed of five layers. An explanation of the configuration of the AMSC tape can be referred to in section 5.2. The test point was measured at 0.8 mm above the surface centre of the stack for both simulations and experiments. The applied fields for both simulations and experiments were previously shown in Figure 3.9. The pulse was acquired from an experiment without any sample involved at 77 K. Due to the limitation of voltage source and capacitor banks, the applied voltage was 30 V. Detailed experiment rigs will be shown in Chapter 5.3.
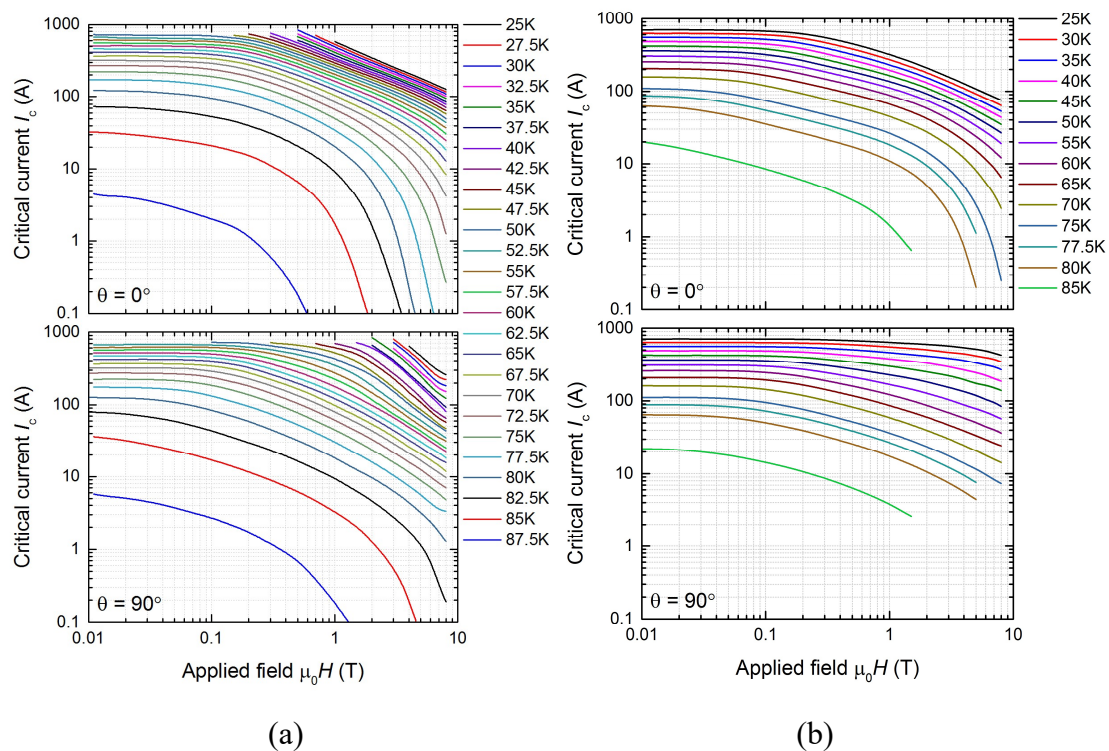
Figure 3.8: Field dependence of the critical current of (a) AMSC and (b) SuperPower tapes measured over various temperatures as the field is perpendicular or parallel to the sample surface [133].
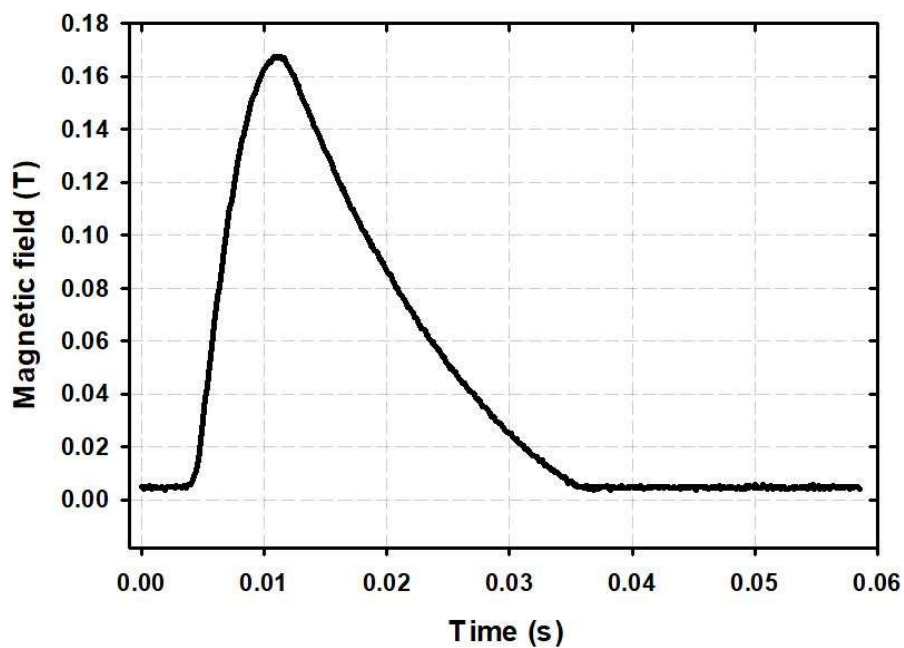
Figure 3.9: Applied pulse for the simulations and experiments of the PFM.

Figure 3.10 shows the comparison results for a 5-layer AMSC stack chilled by liquid nitrogen at 77 K. The trend and values for a single PFM are almost identical, especially for the peak point and final trapped field values. A slight difference appears in the ramp-down duration. The simulation results were slightly higher than the experimental results, which may be related to the noise on the measurement results during the experiments. However, they are still within the approximation and are generally in good agreement. As a result, the proposed 2D *H*-formulation model is validated to be an effective method to predict the trapped field and trapped fluxes of PFM for the AMSC stack.
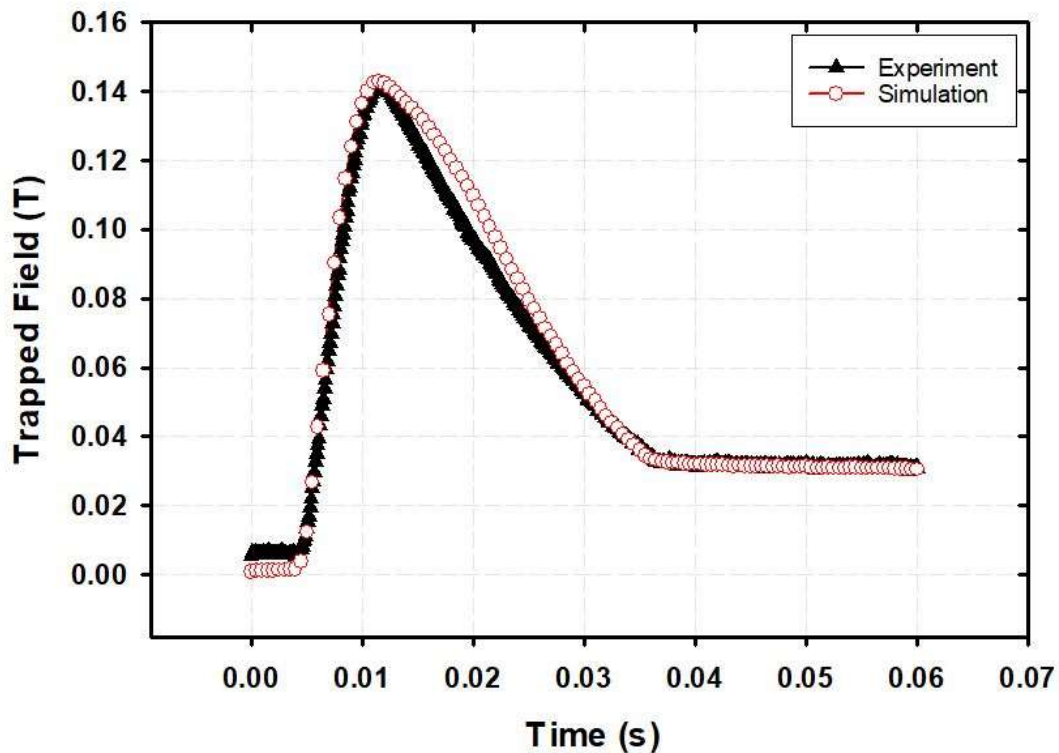
Figure 3.10: Comparison of experimental and simulated results of the 5-layer AMSC stack.

3.2 2D model using *T-A* formulation for HTS stacks

The geometry of the SuperPower stack in COMSOL for the *T-A* formulation model is shown in Figure 3.11. The configuration of the SuperPower tape (without a magnetic substrate) is the same as the definition provided in section 5.2. The thickness of the superconducting layer in the *T-A* formulation model is ignored. However, the properties of the superconducting layer can still be fulfilled by the thin strip approximation, as discussed in section 2.3.3. The other layers of materials are still modelled with their actual thicknesses. The values of the parameters used in the *T-A* formulation model are the same as the ones used in the *H*-formulation model, which are listed in Table 3.2. The governing equations for the *T-A* formulation model are listed in Table 3.3.
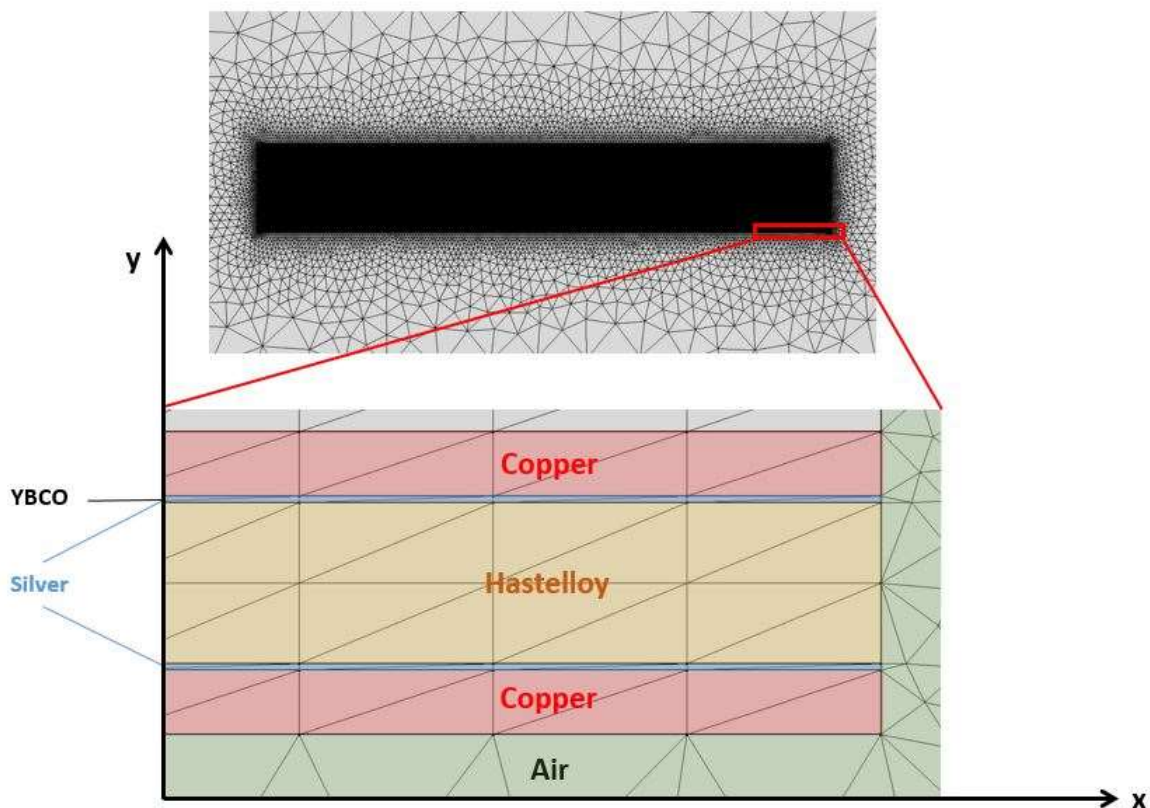
Figure 3.11: Geometry and typical finite element mesh of a 20-layer SuperPower stack in COMSOL. The bottom figure shows the zoomed in mesh with all composing layers and air surrounding. The superconducting layer is approximated as a line.

Table 3.3: Governing equations of the 2D and 3D *T-A* formulation models.

	2D	**3D**
Faraday's law	$\begin{bmatrix} \dfrac{\partial E_z}{\partial y} \\ -\dfrac{\partial E_z}{\partial x} \end{bmatrix} \vec{n} = -\mu_0\mu_r \begin{bmatrix} \dfrac{dH_x}{dt} \\ \dfrac{dH_y}{dt} \end{bmatrix} \vec{n}$ $-\dfrac{\partial}{\partial x}\rho\dfrac{\partial(T \cdot n_y)}{\partial x} = -\dfrac{\partial B_y}{\partial t}$	$\begin{bmatrix} \dfrac{\partial E_z}{\partial y} - \dfrac{\partial E_y}{\partial z} \\ \dfrac{\partial E_x}{\partial z} - \dfrac{\partial E_z}{\partial x} \\ \dfrac{\partial E_y}{\partial x} - \dfrac{\partial E_x}{\partial y} \end{bmatrix} \vec{n} = -\mu_0\mu_r \begin{bmatrix} \dfrac{\partial H_x}{\partial t} \\ \dfrac{\partial H_y}{\partial t} \\ \dfrac{\partial H_z}{\partial t} \end{bmatrix} \vec{n}$
Ampere's law	$J_z = \dfrac{\partial(T \cdot n_y)}{\partial x}$ $\nabla \times \nabla \times \begin{bmatrix} A_x \\ A_y \end{bmatrix} = \mu_0\mu_r \begin{bmatrix} J_x \\ J_y \end{bmatrix}$	$\begin{bmatrix} J_x \\ J_y \\ J_z \end{bmatrix} = \begin{bmatrix} \dfrac{\partial(T \cdot n_z)}{\partial y} - \dfrac{\partial(T \cdot n_y)}{\partial z} \\ \dfrac{\partial(T \cdot n_x)}{\partial z} - \dfrac{\partial(T \cdot n_z)}{\partial x} \\ \dfrac{\partial(T \cdot n_y)}{\partial x} - \dfrac{\partial(T \cdot n_x)}{\partial y} \end{bmatrix}$ $\nabla \times \nabla \times \begin{bmatrix} A_x \\ A_y \\ A_z \end{bmatrix} = \mu_0\mu_r \begin{bmatrix} J_x \\ J_y \\ J_z \end{bmatrix}$
E-J power law	$E_z = E_0 \left(\dfrac{J_z}{J_c}\right)^n$	$\begin{bmatrix} E_x \\ E_y \\ E_z \end{bmatrix} = E_0 \begin{bmatrix} \dfrac{J_x}{J_{norm}}\left(\dfrac{J_{norm}}{J_c}\right)^n \\ \dfrac{J_y}{J_{norm}}\left(\dfrac{J_{norm}}{J_c}\right)^n \\ \dfrac{J_z}{J_{norm}}\left(\dfrac{J_{norm}}{J_c}\right)^n \end{bmatrix}$ where $J_{norm} = \sqrt{J_x^2 + J_y^2 + J_z^2}$, $E_{norm} = \sqrt{E_x^2 + E_y^2 + E_z^2}$
Dirichlet boundary condition	$\begin{cases} H_x = F_x(t) \\ H_y = F_y(t) \end{cases}$	$H = f(t)$ $f(t) = \left[f_x(t); \; f_y(t); \; f_z(t)\right]$

Since the mesh elements in the simulation can affect the trapped field distribution results dramatically in the copper, Hastelloy and silver layers, the same number of divisions were selected for both the *T-A* and *H*-formulation models. There is no thickness for the YBCO layer in the *T-A* formulation model. The total mesh elements in the *T-A* formulation model are less than in the *H*-formulation model. The thickness of the Hastelloy layer was divided into two

parts in the *y*-axis. There were 200 elements along the *x*-axis for each layer. Moreover, the mapped square elements were converted into triangular elements. The air domain was meshed with free triangular elements. The mesh contained 59,332 domain elements and 20,492 boundary elements in total for the 20-layer SuperPower stack.

3.3 Comparison of *H*-formulation and *T-A* formulation for ZFC of HTS stacks

The simulation results using both the *H*-formulation and *T-A* formulation models for the ZFC of a SuperPower stack (without magnetic substrate) are compared in this section. The modeling frameworks in sections 3.1 and 3.2 were adopted. The stack compared in both models was a 5-layer 12 mm × 12 mm squares stack. Only the superconducting layer in the tape is considered in the models. The test point was measured 0.8 mm above the surface centre of the stack for both models, which is the testing height (the thickness of the hall sensor) in the experiment.

The applied triangle pulse for both models is shown in Figure 3.12. Furthermore, the ramp-up and ramp-down time durations are one second. As mentioned in section 2.4.1.1, the pulse for the ZFC method changed within several seconds or minutes. Therefore, it did not involve temperature change. Both the *H*-formulation and *T-A* formulation models were implemented with the same distribution. However, there is no thickness for the superconducting layer in the *T-A* formulation model. Therefore, the total number of mesh domains and boundary elements decreased a lot for the *T-A* formulation model. The number of degrees of freedom (DOF), the minimum reciprocal of the step size (depending on convergence speed) and the computation time for the *T-A* formulation model are much lower than that of the *H*-formulation model. Detailed comparisons are summarised in Table 3.4. Consequently, the *T-A* formulation model is a time-saving method compared to the *H*-formulation model.
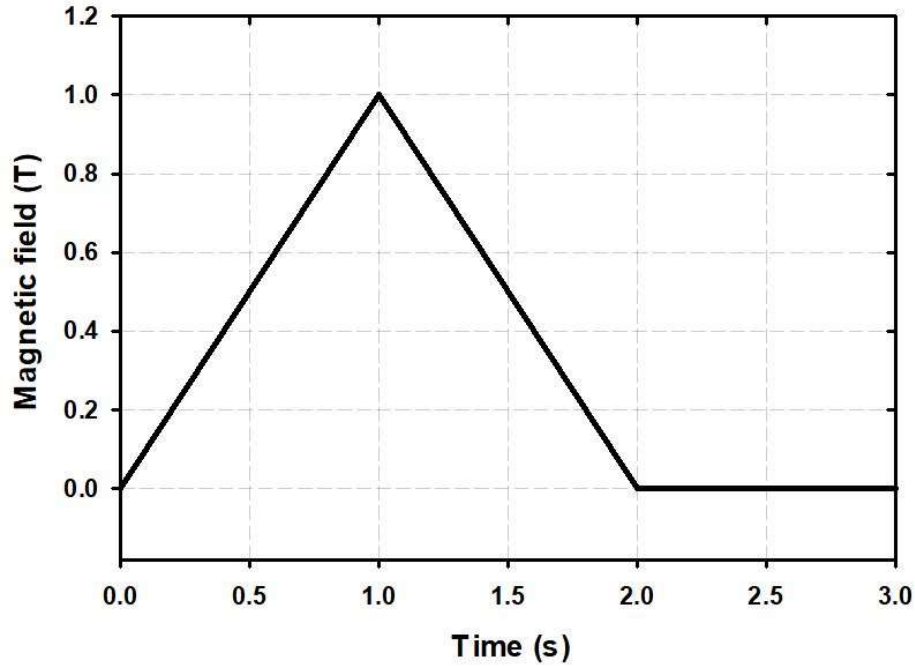
Figure 3.12: Applied field for the simulation comparison of the ZFC.

Table 3.4: Comparison of the mesh and speed of the *T-A* and *H*-formulation models for the ZFC.

	T-A **formulation**	*H*-**formulation**
Mesh domain elements	19554	20016
Mesh boundary elements	3380	4874
Number of degrees of freedoms (DOFs)	11308	30041
Minimum reciprocal of step size	10^3	10^5
Computation time	15 min 6 s (906 s)	14 h 1 min 36 s (50496 s)

The variations in the distribution of the magnetic field and current density for both of the models, changing with time and applied external magnetic field, are shown in Figure 3.13 and Figure 3.14. As can be observed, the distribution of magnetic field and current density for both the *H*-formulation and *T-A* formulation models are almost identical. The only difference is the penetration speed. The penetration speed for the *T-A* formulation model is slower than that of

65

the *H*-formulation model, which may result in a higher trapped field, since it may trap more field when the stack is fully penetrated. In terms of the trapped field results shown in Figure 3.15, both models provide almost the same trapped field results under different magnetic fields.

Figure 3.13: Comparison of the magnetic field distribution of the half side of the SuperPower stack with an external applied field of 1 T during ZFC magnetisation using the H and *T-A* formulation models.

Figure 3.14: Comparison of the normalised current distribution $J/J_c(B)$ of the SuperPower stack with an external applied field of 1 T during ZFC magnetisation using the H and *T-A* formulation models. The thickness of the HTS layer was exaggerated for visualisation.

Figure 3.15: Comparison results of trapped field measured at 0.8 mm above the centre of the SuperPower stack during 3 s using the H and *T-A* formulation models. The applied external field was 1 T.

3.4 Exploration of the 2D thermal-coupled model using *T-A* formulation for HTS stacks

3.4.1 Current redistribution

According to the simulation works, there is a short quench time (milliseconds) during a PFM. The current increased significantly and surpassed the critical current. Meanwhile, the resistance of the superconducting layer in normal zone increases dramatically, which will result in some currents transferred into metallic layers. Therefore, the current redistribution needs to be considered when temperature is involved. Y. Wang et al. mentioned in the paper that the superconductor is equal to two parallel resistances: the resistance of superconducting layers R_{su} and that of the metallic layers R_m [134]. The governing equation of this equivalent circuit can be expressed by the combination of the E-J power law and Kirchhoff's law:

$$\begin{cases} E_0 \left(\dfrac{I_{su}}{I_c(B,T)} \right)^n - I_m \rho_{metallic}(T) = 0 \\ \qquad\qquad I = I_{su} + I_m \end{cases} \tag{3.7}$$

where I_c is the critical current, depending on the background magnetic field B and temperature T. I is the total current flowing in the superconductor tape; I_{su} is the current flowing in the superconducting layer; and I_m is the current flowing in metallic layers. $\rho_{metallic}$ is the resistivity of the metallic layers, which is practically equivalent to the resistivity of the copper stabilizer [135]. $\rho_{metallic}$ can be calculated using the temperature-dependent equation [134]:

$$\rho_{metallic}(T) = \rho_{copper}(300)[1 + 0.0039(T - 300)] \tag{3.8}$$

where ρ_{copper} is the resistivity of the copper stabilizer at 300 K.

In the *T-A* formulation model, the current redistribution can be set in the *Boundary ODEs and DAEs* part in COMSOL for the thin strip layer based on the governing equation 3.7.

3.4.2 Heat transfer model

Due to the thin strip assumption adopted in the *T-A* formulation model, the *Heat Transfer on Solids* part in COMSOL (discussed in section 3.1.2.1) can only deal with the thermal parts in the substrate and stabiliser layers. All the thermal-dependent parameters of the materials in the substrate and stabiliser layers are defined in the *Material* part. The heat source is the volumetric loss density in the electromagnetic section. The governing equation for each substrate or stabiliser layer can be written as:

$$Q_{m0} = \rho_m C_{pm} \frac{\partial T}{\partial t} - \nabla \cdot (-k_m \nabla T) \tag{3.9}$$

where Q_{m0} is the power density dissipated by the heat source of the corresponding substrate or stabiliser layer; ρ_m, C_{pm} *and* k_m are the density, heat capacity and thermal conductivity of the corresponding substrate or stabiliser layer according to the real configuration of the tape (Figure 3.5 and Figure 3.6).

The thermal problem in the superconducting layer needs to be solved by the *Heat Transfer in Thin Shells* part. The heat transient equation given by Joule dissipation is:

$$Q_s = d_s \rho_s C_{ps} \frac{\partial T}{\partial t} - \nabla \cdot (-d_s k_s \nabla T) \tag{3.10}$$

where Q_s is the power density dissipated by the heat source of the superconducting layer; d_s is the thickness of the YBCO layer, which is assumed to be 1 µm in this thesis; ρ is the density of YBCO, which is selected as 5900 kg/m³ in the model; C_p is the heat capacity of YBCO (Figure 3.6); and, k is the thermal conductivity of YBCO (Figure 3.5).

Overall, the thermal parts of metallic (stabilizers and substrates) and superconducting layers were solved in union in [134]. The equivalent homogenous thermal conductivity k and heat capacity C_p were utilized in the entire conductor. However, the heat transfer models for metallic and superconducting layers were solved separately in the proposed thermal-coupled model. They were computed in different *Heat Transfer* modules.

The discretisation of the thermal equation for both *Heat Transfer* parts is solved linearly, which can reduce the number of DOF and not result in a singularity or divergence.

3.5 Comparison of *H*-formulation and *T-A* formulation models for PFM of HTS stacks

To validate the proposed *T-A* thermal-coupled model for the trapped field magnetisation case, a 20-layer SuperPower HTS stack was simulated under different external magnetic fields using both the *H*-formulation and *T-A* formulation models. Equation 3.5 was still utilized in both of the models with the value of 1.5 and 92 K for parameter α and T_c, respectively. The *n* value

and B_0 used in both models were 21 and 1 T, respectively. The applied magnetic fields for both of the models is expressed by equation 2.24 and shown in Figure 3.16. In the equation 2.24, the τ for the rise time of the pulse is 0.01 s. Furthermore, B_a is the applied field magnitude, which is 2 T.
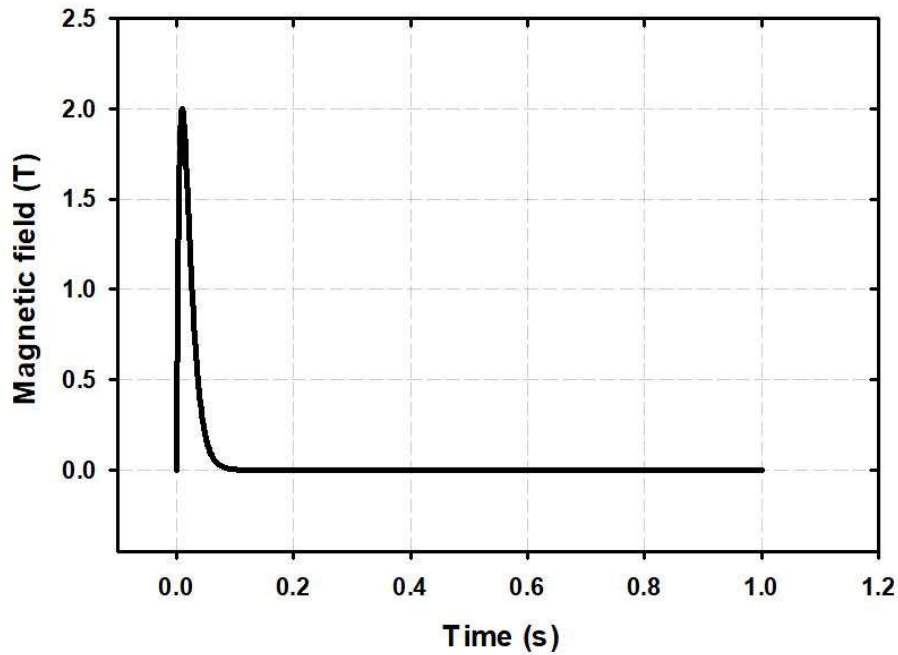
Figure 3.16: Applied field for the compared simulation of the PFM for the two models.

Table 3.5: Comparison of the mesh and speed of the *T-A* and *H*-formulation models for the PFM.

	T-A formulation	*H*-formulation
Mesh domain elements	56320	65750
Mesh boundary elements	20474	24514
Number of degrees of freedoms (DOFs)	188839	126983
Minimum reciprocal of step size	1	10^4
Computation time	3.6 h	168 h

The total number of mesh domains, boundary elements, minimum reciprocal of the step size and computation time for the *T-A* formulation model are much lower than that of the *H*-formulation model. Detailed comparisons are summarised in Table 3.5. It can be observed that the calculation speed of the *T-A* formulation model has increased by over 50 times compared to the *H*-formulation thermal-coupled model.

The distribution of magnetic field and normalised current density are shown in Figure 3.17 and Figure 3.18, respectively. The heat generation powers per thickness of different layers of material in the SuperPower stack are also compared in Figure 3.19. It is observed that the distribution of magnetic field and normalised current density for the H and *T-A* formulation models are almost identical in magnitude. The trapped magnetic field simulated by the *T-A* formulation model is slightly higher near the centre of the stack for the duration of the pulse applied. The normalised current distributions are not exactly the same for the penetration speed especially when compared at 0.1 s. The results were similar to the results shown in section 3.3. The superconducting layer of the stack modelled by the *H*-formulation model had been fully magnetised by the reverse direction of the current. Conversely, the stack modelled by the *T-A* formulation model had not been fully magnetised. The reason for the phenomena might be related to the lamination structure of the model. In terms of previous research on *T-A* formulation, the structure of the model is quite simple, which involves only superconducting layer or equivalent-circuit homogenised model [51, 52, 134], like the model simulated in section 3.3. When different materials of the adjacent layers were added into the model, the metallic properties and thickness will affect the magnetic and current distribution of not only the superconducting layer but also the whole stack. There might be parallel fields produced which cannot be solved by *T-A* formulation model.

The dissipated heat per thickness for all the layers is shown in Figure 3.19. The heats generated in the stabilisers (copper and silver layers) in the *H*-formulation model was higher than that of the *T-A* formulation model. For the *T-A* formulation model, the heat was concentrated in a thin line whereas there was a thickness of 1 μm for the YBCO layer in the *H*-formulation model, so more heat was dissipated into the connecting layers. As Figure 3.11 shows, there are double layers of copper and silver in a single tape. The top layers of silver and copper are connected to the YBCO layer where the most heat is produced. The heat dissipated to the other two layers of copper and silver sank a lot by the substrate (Hastelloy layer). Therefore, the overall heat generated in the copper and silver layers in the *H*-formulation model are higher than that of the *T-A* formulation model.
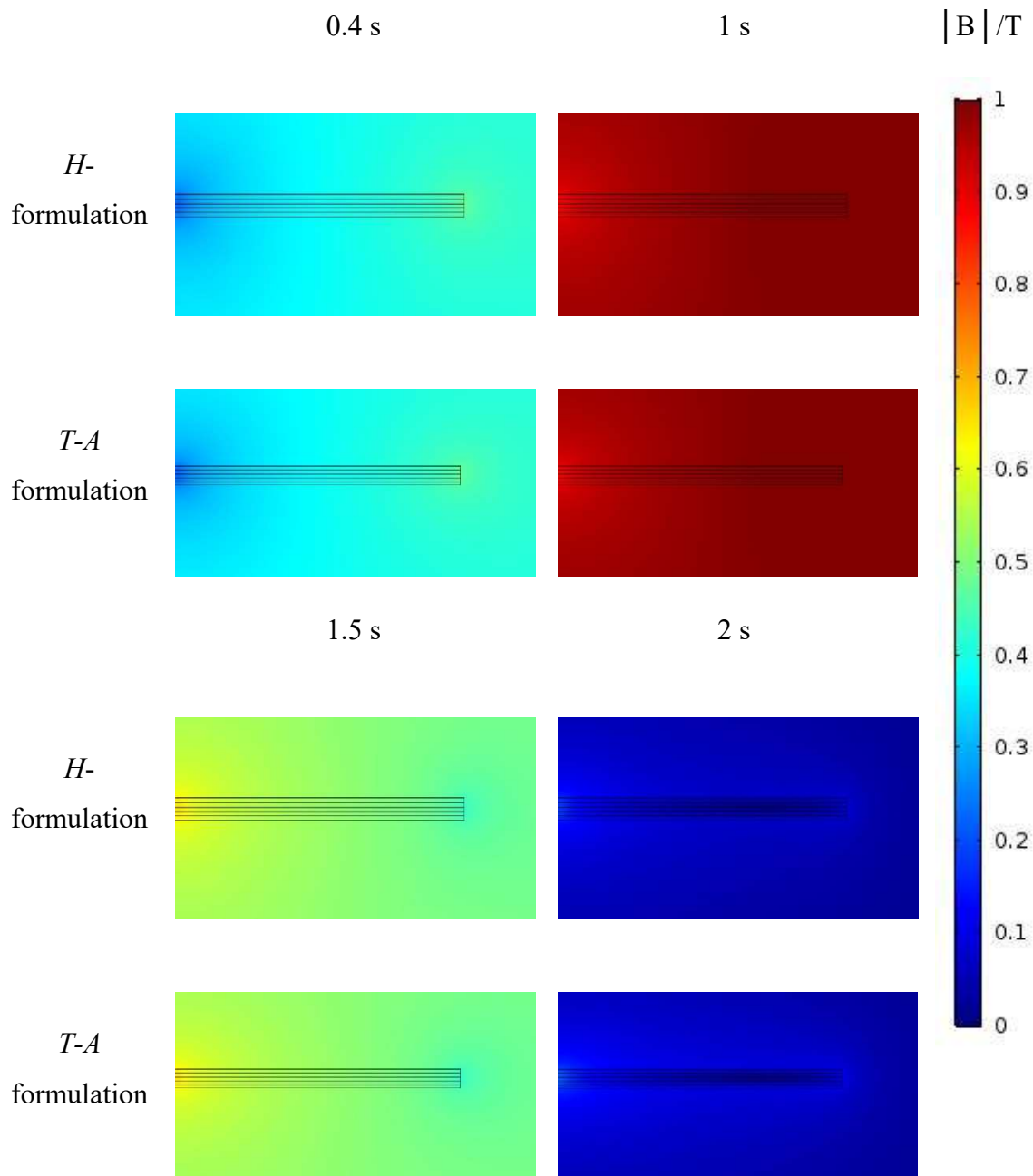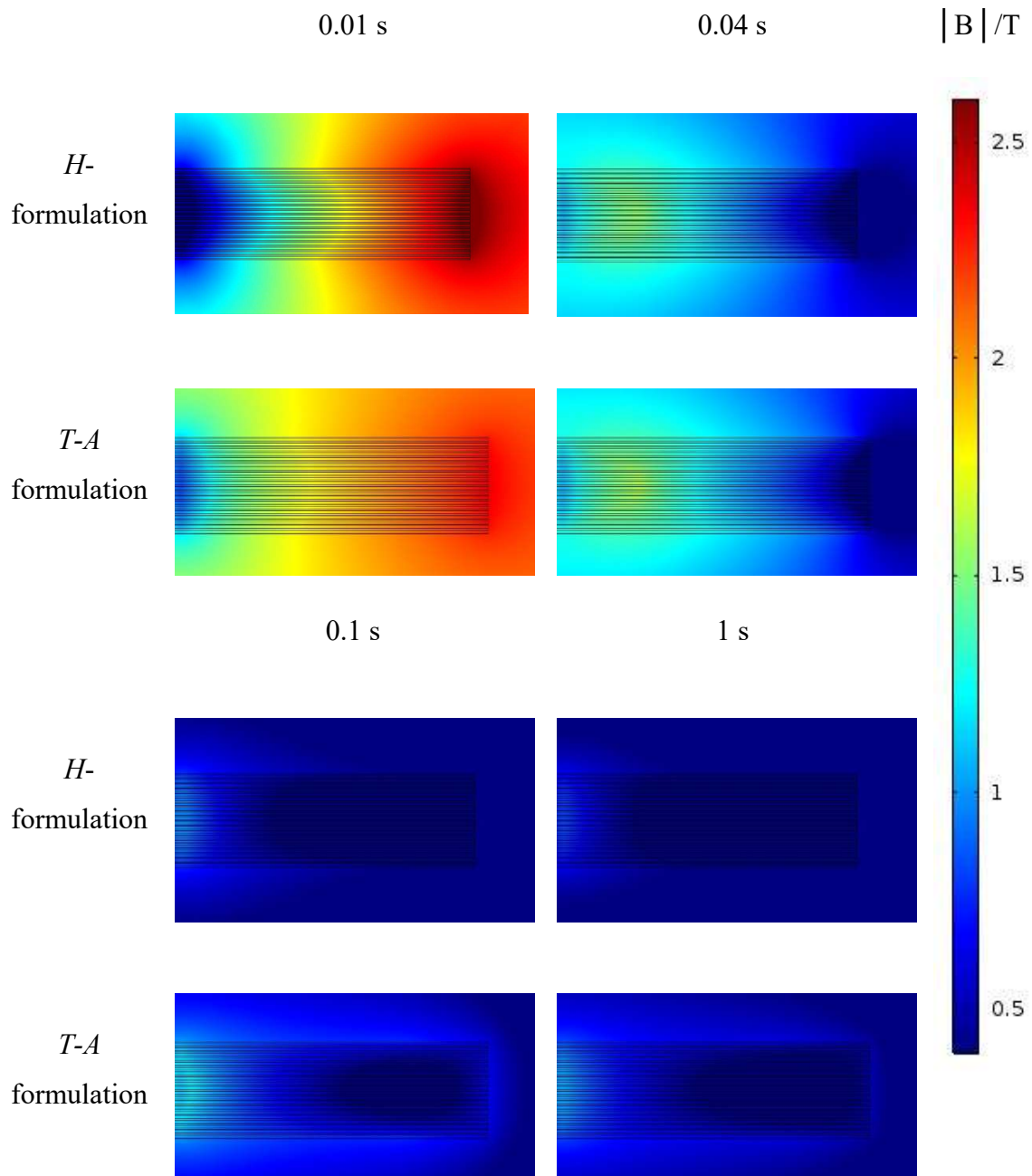
Figure 3.17: Comparison of the magnetic field distribution of half side of the SuperPower stack with an external applied field of 2 T during PFM using the H and *T-A* formulation models.

Referring to the trapped field results shown in Figure 3.20, the final field trapped in the centre of the stack modelled by the *T-A* formulation model is larger than that of the *H*-formulation model. One possible reason is that the penetration speed of the *T-A* formulation model is slower than that of the *H*-formulation model. It also highlights that the variation in temperature can affect the final trapped field results in the centre of the stack. However, the tendencies of the trapped field with different applied fields for both models are generally the same. *T-A* formulation model can be used as qualitative instead of the quantitative simulation for PFM of HTS stacks. The results also showed that the current redistribution did not have much impact on the magnetic field or current distribution.
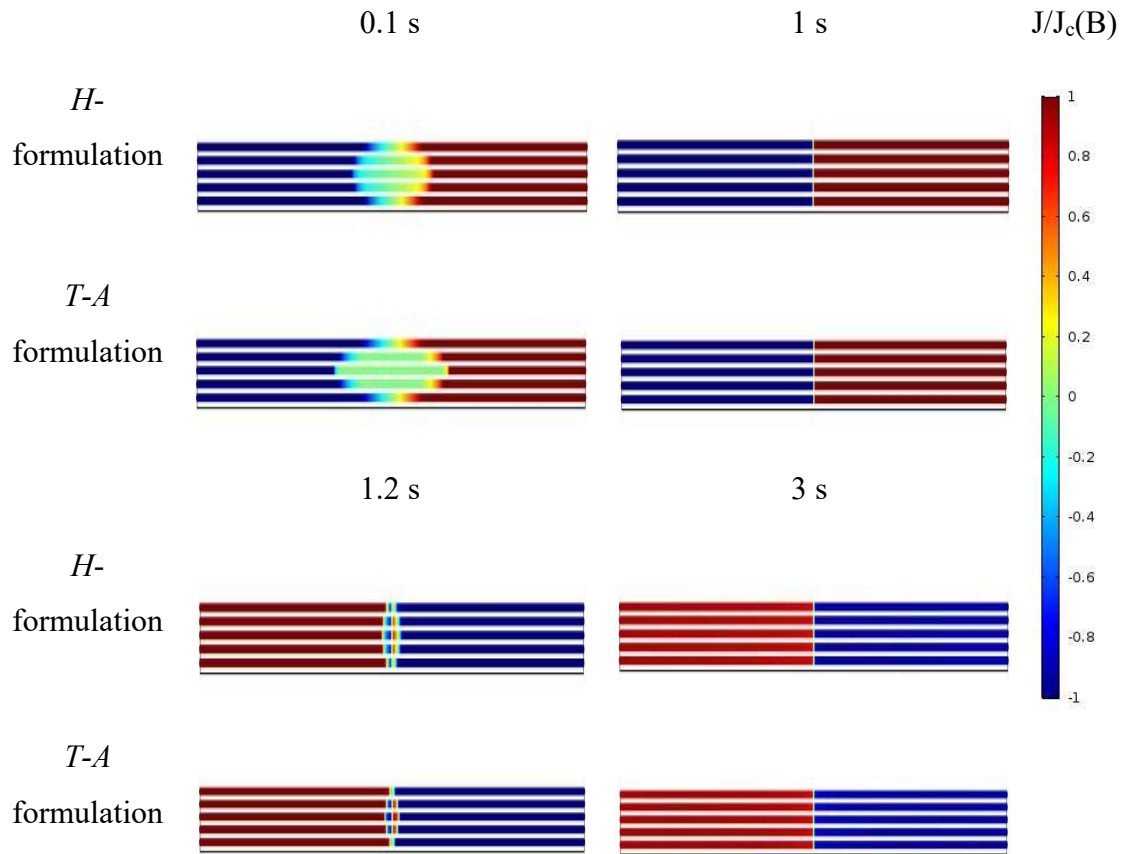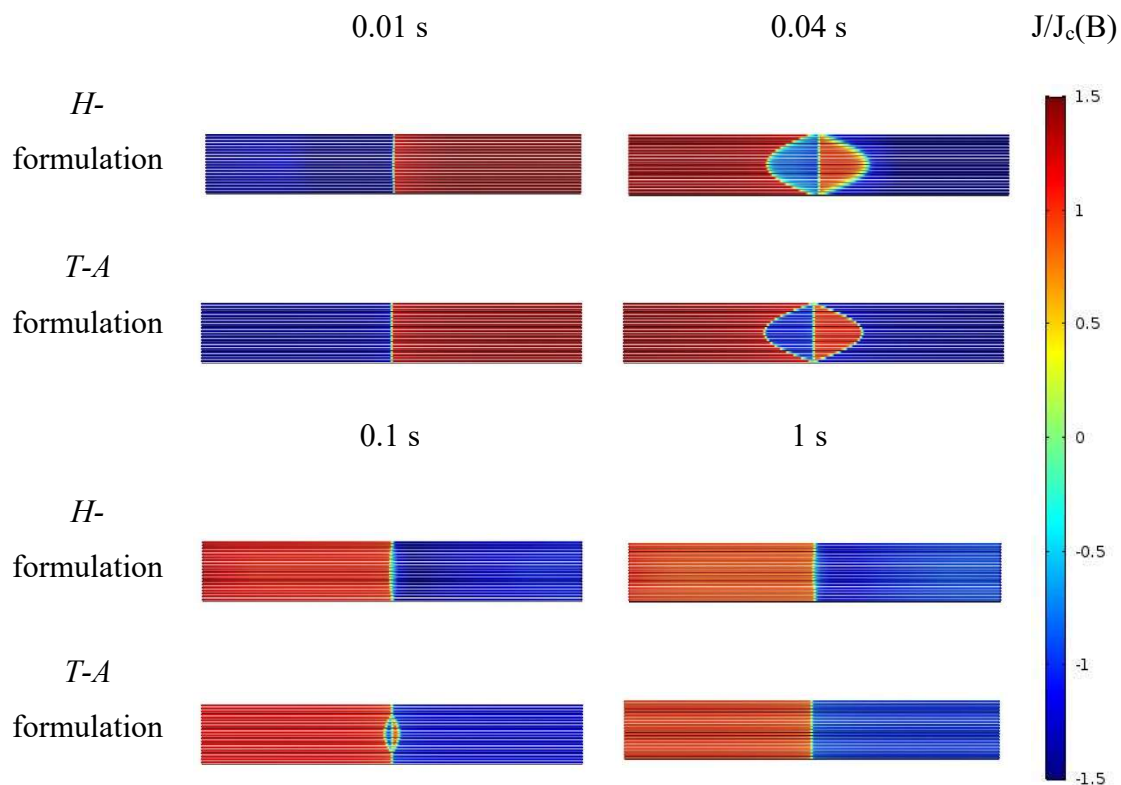

Figure 3.18: Comparison of normalised current distribution *J/Jc(B)* of the SuperPower stack with an external applied field of 2 T during PFM using the H and *T-A* formulation models. The thickness of the HTS layer was exaggerated for visualisation.
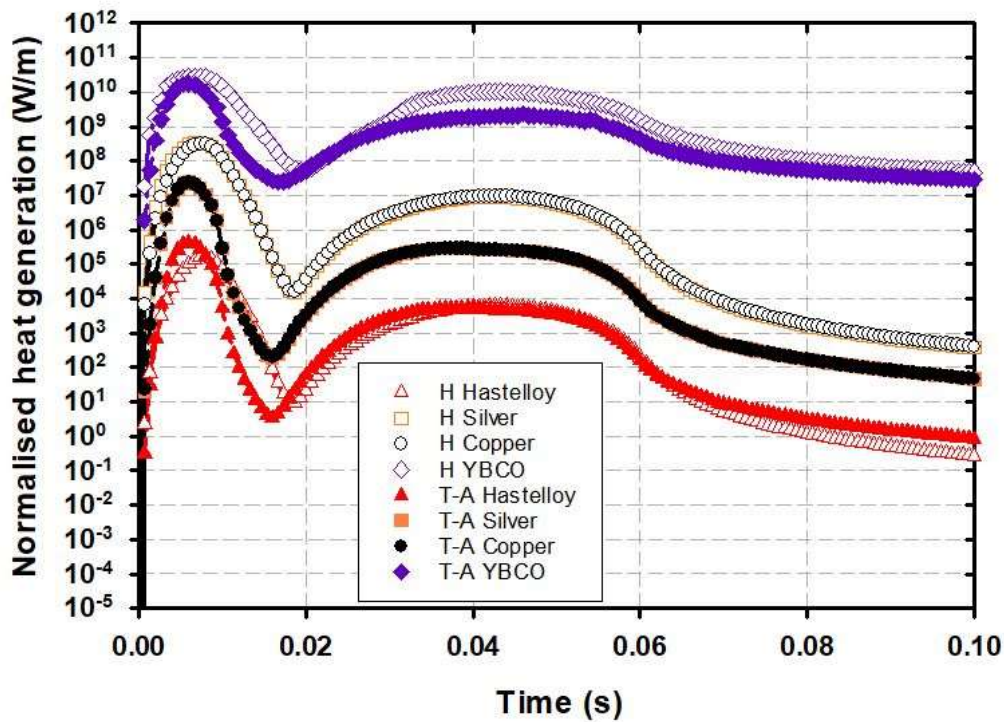
Figure 3.19: Normalised heat generation power of different layers of materials during PFM using the H and *T-A* formulation models.
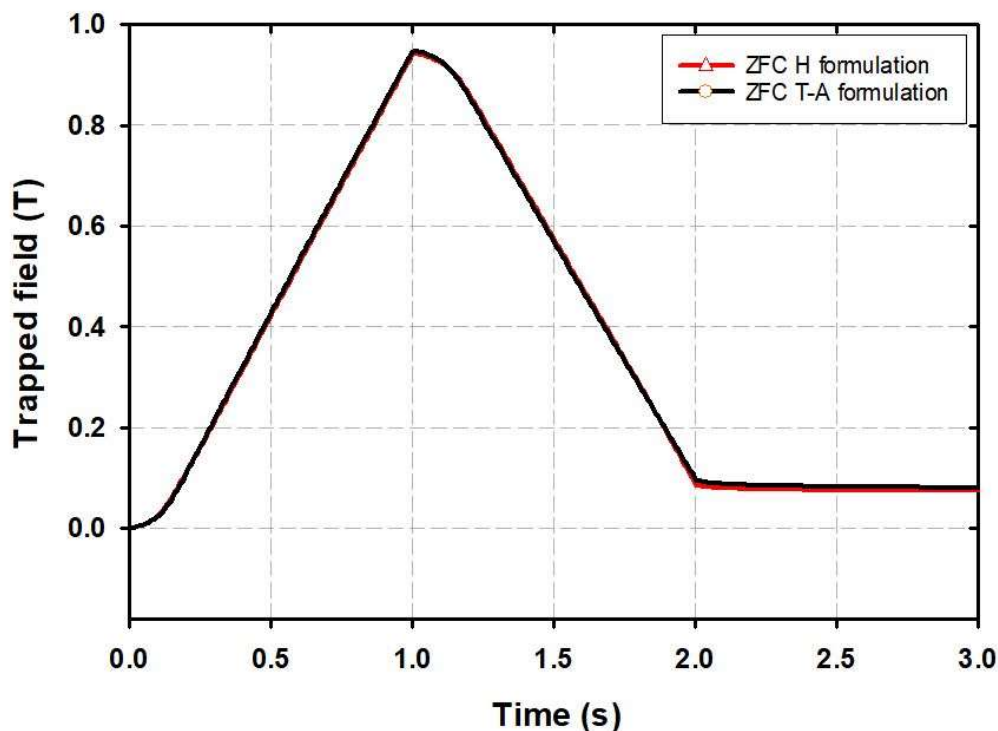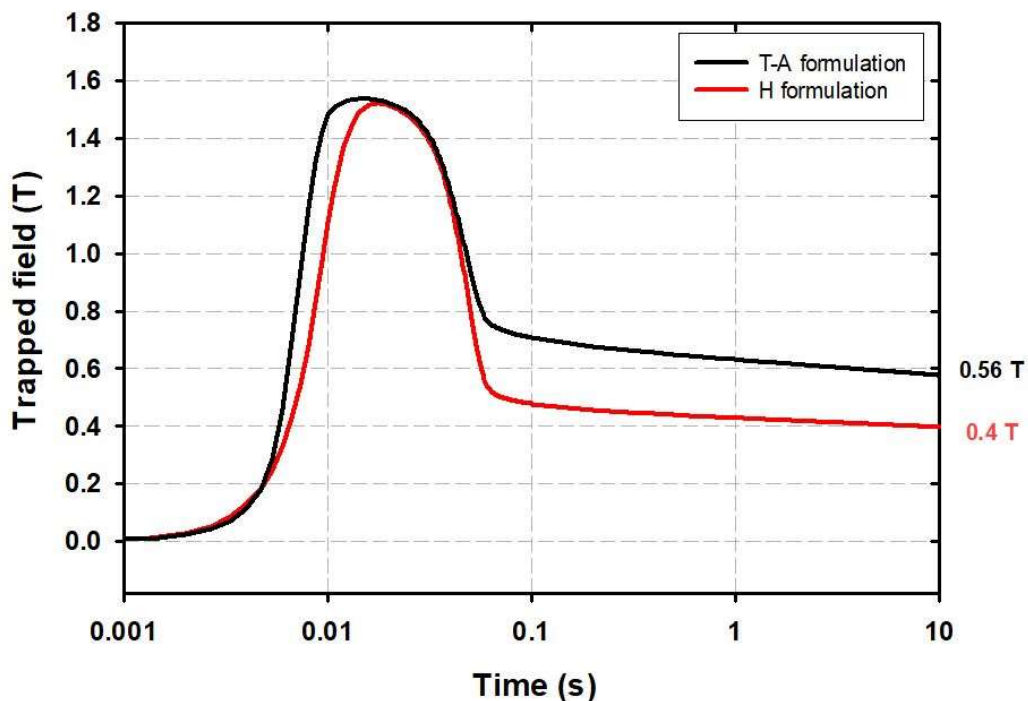

Figure 3.20: Comparison results of trapped field measured at 0.8 mm above the centre of the SuperPower stack during 10 s using the H and *T-A* formulation models. The applied external field was 2 T.

3.6 Conclusion

A 2D thermal-coupled *H*-formulation model of the AMSC stack was introduced in section 3.1. The proposed 2D *H*-formulation model of PFM was validated by experiments on a 5-layer AMSC stack in section 3.1.3. A 5-layer stack model using *T-A* formulation was compared to the *H*-formulation model for ZFC magnetisation in section 3.3. The calculation time of the *T-A* formulation model was much less than the *H*-formulation model. Although the penetration speed of the *H*-formulation model was higher than the *T-A* formulation model, the magnitude of magnetic field and current density, as well as the trapped field changing with an external magnetic field, were generally in good agreement.

A new FEM thermal-coupled model using *T-A* formulation to calculate the trapped field by PFM was presented in sections 3.2 and 3.4. The simulated results were compared with the *H*-formulation model in section 3.5. The computational time of the *T-A* formulation model was significantly less compared to the *H*-formulation model. However, for laminated structure of models, when heat transferred between different layers, current and magnetic field distribution can be affected by the thin approximation model. The trapped field somehow will be enhanced. The final trapped field values using both formulations did not match perfectly. The *T-A* formulation would be a better choice to be used for simple structure analysis and qualitative simulation for PFM of HTS stacks. More investigation is required for the thermal-coupled T-A formulation to understand the extent of its usefulness on laminated structure of models. Therefore, *H*-formulation will be the fundamental FEM utilized in the thesis to ensure the accuracy and consistency of simulation results.

The simulation works also indicated that the heat capacity, thermal conductivity and electrical resistivity are important variables for different materials on account of the heat generated during the PFM process. Stabilisers and substrates with lower values of heat capacity and thermal conductivity could give rise to a lower temperature rise during PFM, which can result in higher trapped field values.

Chapter 4　　Simulations　　　of　　　pulsed-field magnetisation of HTS stacks

Simulations provide good approximations for practical or theoretical cases. The results from simulations also motivate the progress to practical testing and test-rig system building. According to the test results from previous research group, further analysis needs to be completed for pulse-field magnetisation (PFM) by simulations. It is difficult, time consuming and expensive to analyse the magnetic distribution and heat dissipation for different substrates and stabilisers by experimental analysis. Therefore, detailed investigations with the feedback from some experimental work can be fulfilled by creating more composite and thermal coupled structures in modelling. In this chapter, essential parameters related to the trapped fields in simulations will be discussed in section 4.1. Trapped fields depending on stacks with and without a magnetic substrate and the thicknesses of substrates will be analysed in section 4.2.

4.1 Influence of simulated parameters on trapped fields of HTS stacks with and without a magnetic substrate

Two relevant parameters can affect the trapped field results significantly. One is the n value in the E-J power law (equation 2.7), which is related to the electrical resistivity of the HTS layer. The other is the flux density constant B_0 in the Kim model (equation 2.8), which is the association between the temperature-dependent critical current and magnetic field. Zou *et al.* provided a detailed investigation of the influence of parameters on a HTS bulk in a 2D axisymmetric model with and without the thermal coupling. The simulation results indicated that the optimal trapped field increases with a larger n value and B_0. Furthermore, temperature

can affect the trapped field dramatically [136]. According to previous experiments and simulation work, the value of n and B_0 ranges from 8 to 50 and 0.3 to 6, respectively [65, 78, 79, 96, 126, 137].

In previous simulations of PFM of a stack, two different n values were used for different ranges of time. An n value of 9 was used before 0.1 s (duration of pulse), to avoid instability caused by higher n values; and, 21 was chosen to simulate during 0.1 to 10 s, which is more adequate to practical flux creep. B_0 was selected to be a constant value of 1.3 T [96, 137]. However, it is temperature-dependent with values for B_0, presented in [78], to have a range of 0.59 T to 5.04 T from 65 K to 20 K, respectively. Although the n value and B_0 somehow can be acquired from experiment results, it is still worthy to analyse the appropriate estimation and elucidate the effects of these parameters on different structures and materials of stacks in simulations.

In this chapter, the AMSC (with magnetic substrate) and SuperPower (without magnetic substrate) stacks were built in 2D electromagnetic-thermal coupled planar models using H-formulation. Detailed configurations about the models were introduced in the previous chapter. The influence of the n value and B_0 on the simulation results of HTS stacks (with and without magnetic substrates) magnetised by PFM are presented in this Chapter.

A one-pulse magnetisation field is applied to a stack, as shown in Figure 4.1 [138], which follows the following equation:

$$
B_{ap} = \begin{cases} B_a \sin^2\left(\frac{\pi t}{2\tau}\right) & 0 \leq t \leq \tau \\ B_a \cos^2\left(\frac{\pi(t-\tau)}{10\tau}\right) & \tau \leq t \leq 6\tau \end{cases} \tag{4.1}
$$

where τ is the ramp-up time, which was selected as 0.01 s in this work. The ramp-down duration was 0.05 s. This artificial pulse has the same tendency as the pulse in equation 2.24 which is driven by the discharging of a capacitor bank [136]. It is smoother at all transient points and is more beneficial to retain stability, avoid singular and no coverage during modelling, which can improve the computing speed. According to the results provided in [137], the dependence of the trapped field on the applied field was not affected by the time after 10 s and the trapped field rose with an increase in the sample height. Thus, all the trapped field is acquired after 10 s and 0.8 mm (the hall sensor height) above the stack surface centre.
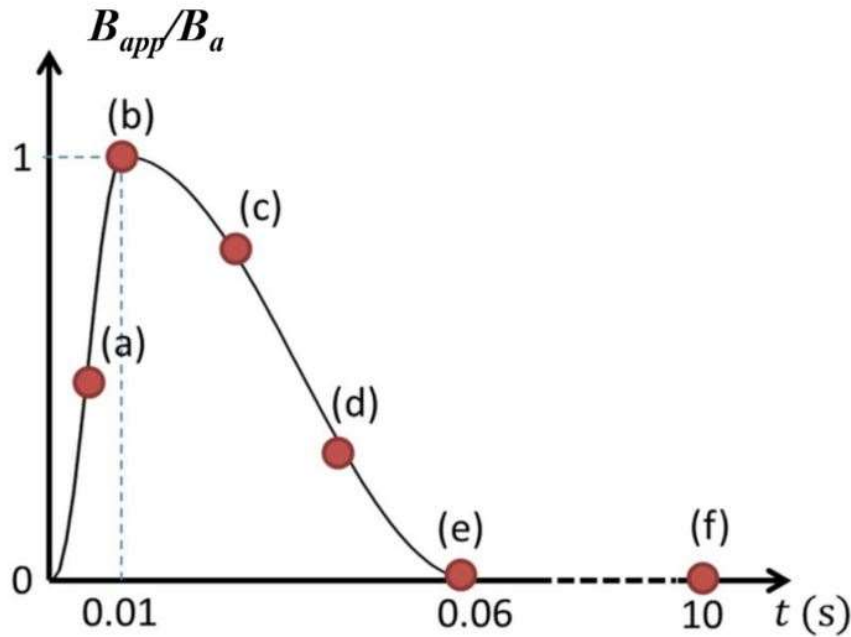
Figure 4.1: Single-pulse magnetisation field applied to a stack in the simulations at (a) 0.005 s; (b) 0.01 s; (c) 0.015 s; (d) 0.04 s; (e) 0.06 s; (f) 10 s [78].

4.1.1 Effects of n value in E-J power law

The n value defines the steepness of the shift between the superconducting and normal states for superconductors and accounts for flux creep relaxation. To avoid the effect of different $J_c(B)$ to the final trapped fields, same $J_c(B)$ value (based on equation 2.8) was applied for both AMSC and SuperPower models. The B_0 value was set as 1 T. Three different n values were selected to compare as variables, which were 8, 21 and 35. They are all common n values that have been used in previous research [55, 96, 139].

It can be seen in Figure 4.2 that a larger n value results in a larger trapped field and lower temperature rise in both the AMSC and SuperPower stacks after 10 s. Moreover, there are saturation points for both the AMSC and SuperPower stacks where they reach the optimal trapped field. Before the saturation point, the external applied field is too small to fully magnetise the stacks. If the applied field is too large, the stacks will be over magnetised, which leads to excessive heat and diminishes the trapped field. The presented results match the conclusion of the bulk model in [136].

The decay of trapped fields needs to be considered especially for lower n values. As presented in Figure 4.2 and Figure 4.3, a decrease in the trapped field can be as much as 32% and 34%

for the AMSC and SuperPower stacks, respectively. After 0.06 s, the trapped field dropped down dramatically for $n = 8$ in the centre but for $n = 35$ the decay was steadier for both stacks. Figure 4.2 shows that the rate of temperature rise increases as the n value decreases. In other words, after the saturation point or in the over magnetisation duration, the trapped field with a smaller n value decreases faster than one with a larger n value after the ramp-up pulse.

Applying the same n value, B_0 and external field, the AMSC stack trapped more field and produced less heat during PFM than the SuperPower stack. The temperature growth in the SuperPower stack reached 18 K at saturation with an n value of eight and an external applied field of 2 T, which is more than five times higher than the temperature growth in the AMSC stack (3.5 K). The reasons for this could be related to the temperature-dependent thermal conductivity and heat capacity in each layer. According to Figure 3.5 and Figure 3.6, the overall thermal conductivity and heat capacity of the SuperPower stack is much higher than that of the AMSC stack. However, it cannot be guaranteed that the AMSC stack has better performance of trapping field over the SuperPower stack. In this part, we assume the same current- magnetic field distribution applied for both AMSC and SuperPower stacks, therefore, the value of $J_c(B)$ in the simulation might not correspond to the experimental test results mentioned in Chapter 3.1.3. Furthermore, the effect of stack thickness also needs to be taken into consideration for further investigation.

Referring to the normalised current density $J_z/J_c(B)$ in Figure 4.4, the normalised current density decreases when the n value increases for both the SuperPower and AMSC stacks. The peak point of the applied single pulse field is at 0.01 s. At this time, the stack with $n = 21$ has been fully penetrated, which is not the case for $n = 8$. The same conclusion can be draw for the AMSC stack as well. Thus, applying the same external field, the penetration depth is shallower with a smaller n value. Additionally, the normalised current density $J_z/J_c(B)$ rises significantly to over two during the ramp-up pulse duration when $n = 8$. This indicates that the superconducting layer is in an over-critical state for several milliseconds. There are no errors mathematically in the simulations but theoretically the current should not cause a quench for a long time due to the unbound exponential increase of the electric field for currents above the critical current I_c [140, 141]. Since the temperature increases in a short time for the PFM, it will not lead to an irretrievable quench. To summarise, it is doubtful whether smaller n values should be used, especially during the ramp-up and ramp-down pulse regions within 0.1 s.

(a)

(b)
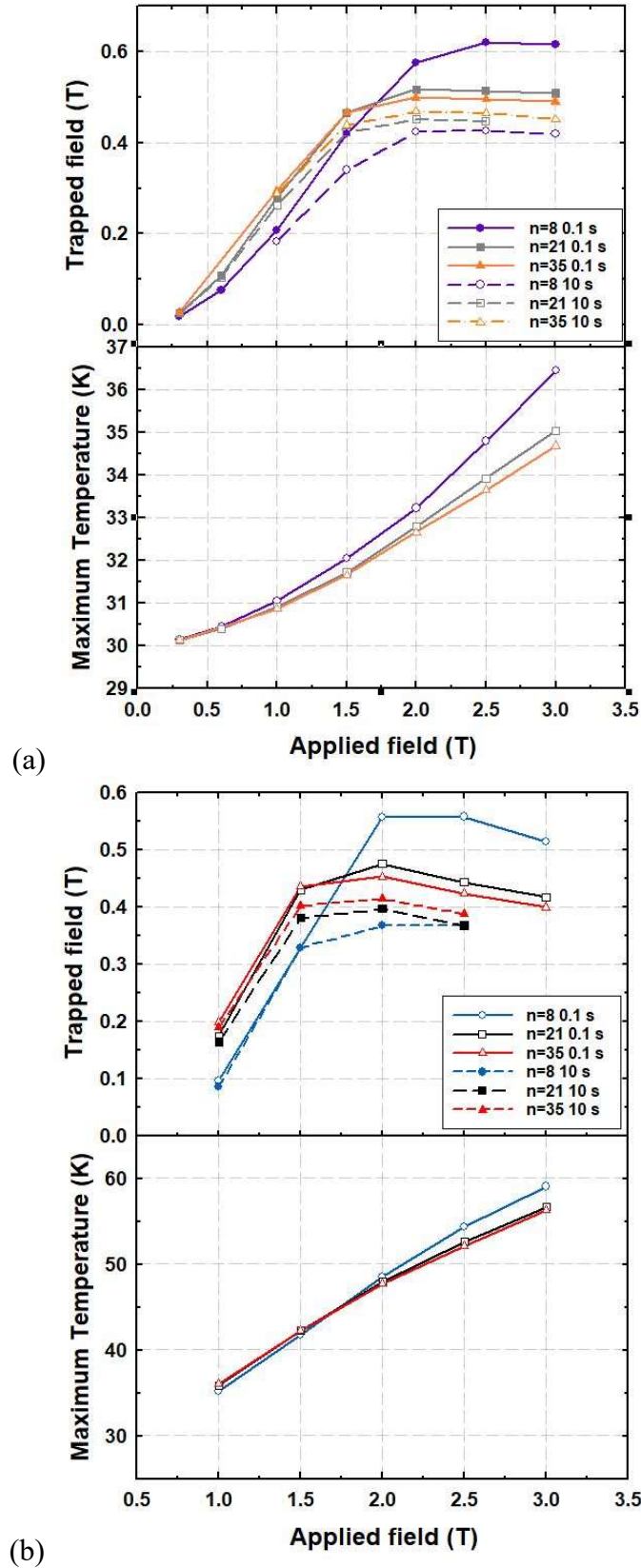
Figure 4.2: Comparison of trapped fields and maximum temperatures of a 20-layer (a) AMSC stack and (b) SuperPower stack at 30 K for different *n* values in the E-J power law at 0.1 s.

(a)

(b)
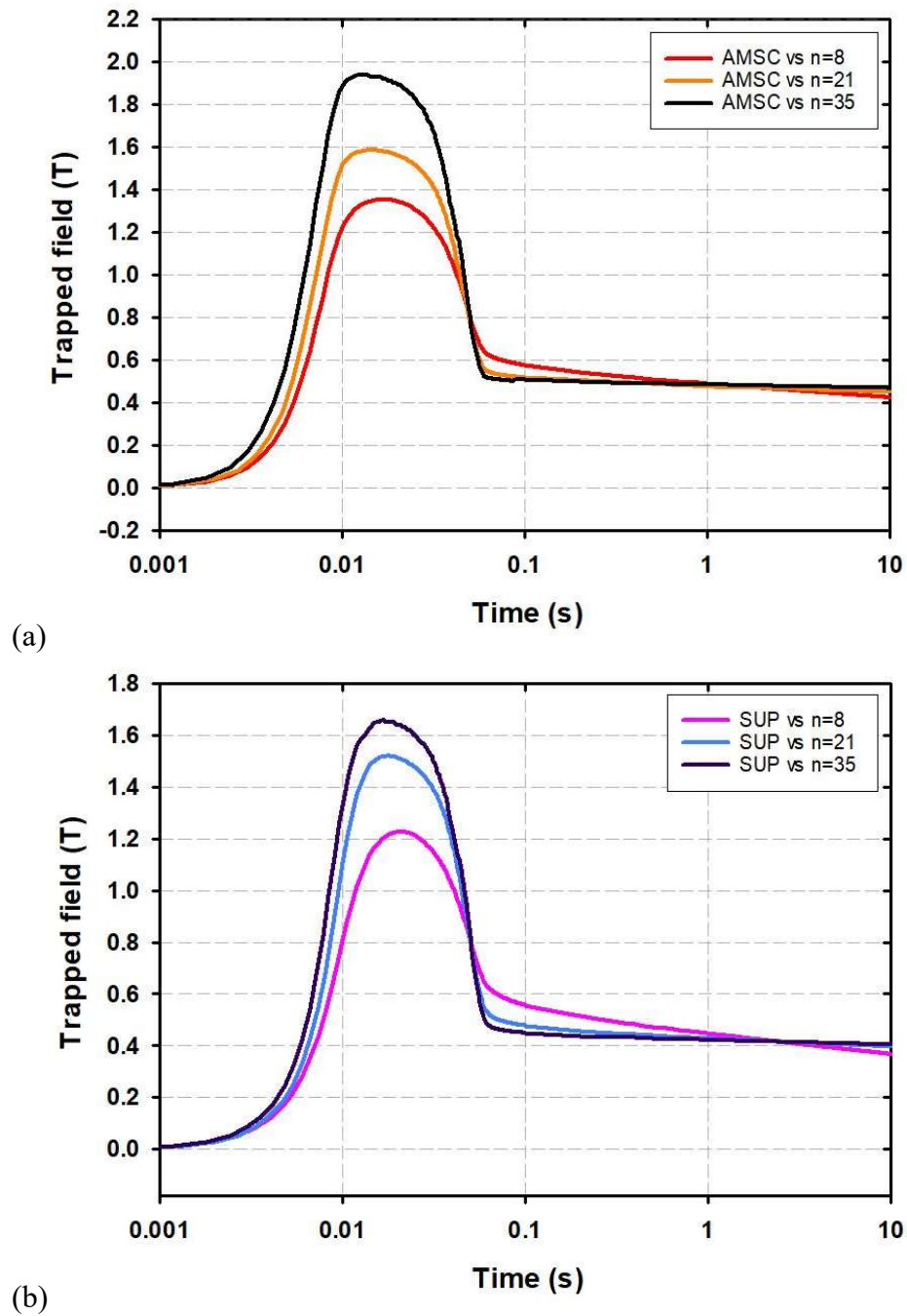
Figure 4.3: Comparison results of trapped fields with different *n* values applied to the (a) AMSC stack and (b) SuperPower stack for 10 s. The magnitude of the applied field is 2 T.
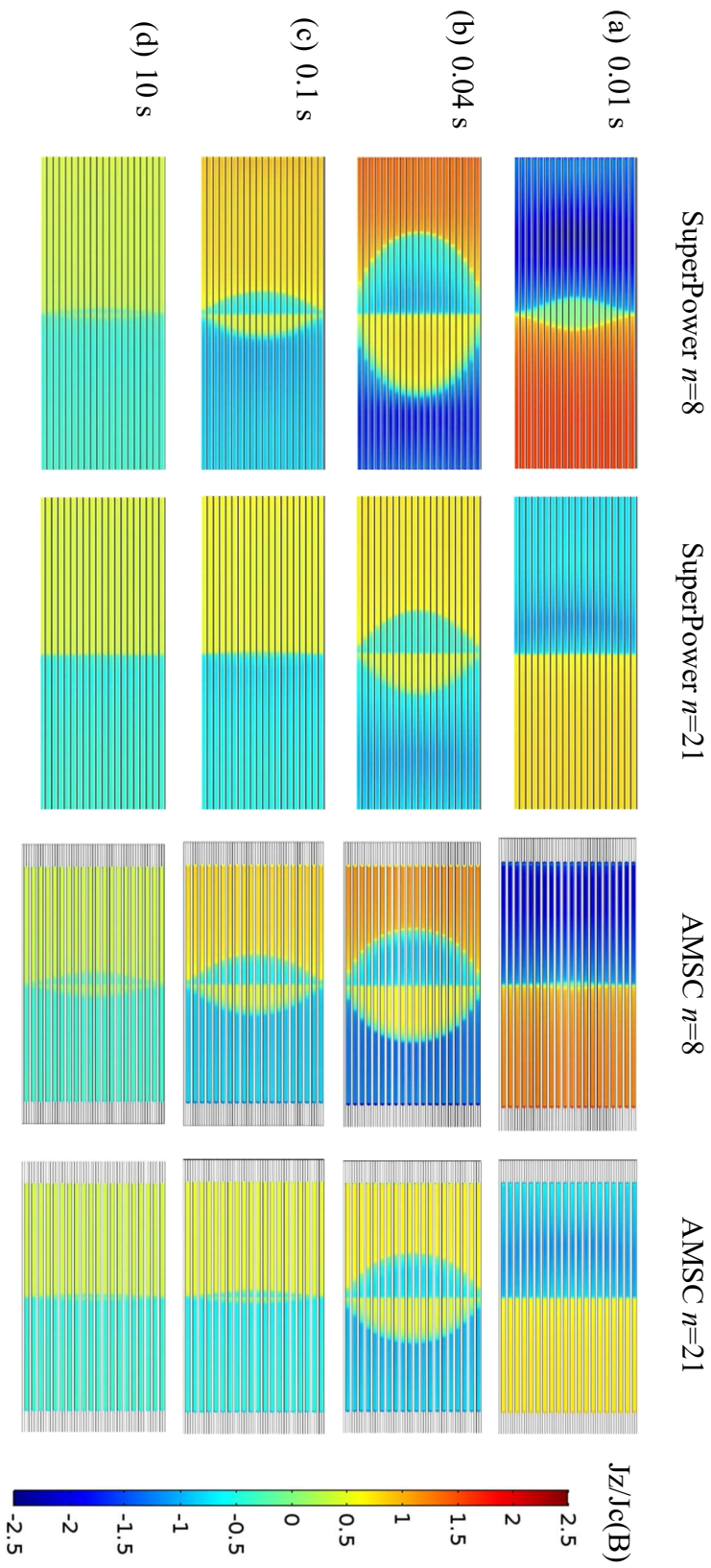
Figure 4.4: Normalised current distribution $J_z/J_c(B)$ of the SuperPower stack and the AMSC stack with an applied field of 2T with different n values at (a) 0.01 s, (b) 0.04 s, (c) 0.1 s, (d) 10 s. (The thickness of the HTS layer was exaggerated for visualisation. The figures of the cross-section of the stacks are not to scale.)

4.1.2 Effects of B_0 in Kim model

The effects of the flux density constant B_0 are secondly compared between the AMSC and SuperPower stacks. The n value is set as 21 in the E-J power law. Comparison results of the trapped fields and the maximum temperatures against the amplitude of the external applied field are presented in Figure 4.5. Three different values of B_0 are compared, which are 0.4 T, 1 T and 4 T. Both the AMSC and SuperPower stacks have the same tendency, i.e. the optimal trapped field and maximum temperature generated during the process increases with an increase of B_0. The conclusion is the same as the simulation results for bulks [136].

The saturation points for the AMSC stack appear at 1.5 T, 2 T and 3 T when the trapped field is 0.33 T, 0.45 T and 0.66 T after 10 s for B_0 equals 0.4 T, 1 T and 4 T, respectively. The optimal trapped fields for the SuperPower stack are 0.31 T, 0.4 T and 0.5 T for B_0 equals 0.4 T, 1 T and 4 T with approximately 1.5 T, 2 T and 2.5 T applied field, respectively. It can be clearly seen that the larger the B_0 value, the more the fields could be trapped in the stack and the larger the applied field required for both the SuperPower and AMSC stacks for all time scales. Moreover, more heat is generated when a larger B_0 is applied, which reduced the maximum trapped fields for both stacks.

In terms of the normalised current density in Figure 4.6, the penetration speed for stacks with a higher B_0 is slower as the same pulse field applied, which represents the stacks with a higher B_0 have more potential to capture more fluxes if apply a higher magnetising field. Thus, if the critical currents of two tapes are similar, the one with high B_0 value might trap more fields. Finally, the trapped field of the AMSC stack decreases slower than the SuperPower stack owing to more heat being generated in the SuperPower tape when the same applied field surpasses the saturation point. The reason is the thermal conductivity of the copper stabilizer in the SuperPower stack is much higher than that of the stainless steel stabilizer in the AMSC stack. Thus, the overall heat generation for the SuperPower stack is higher than that of the AMSC stack under the same condition.

For both of the study, compared with the results for superconducting bulk [136], the maximum temperatures in the centre of the top surface of the stacks during the pulse-field magnetisation did not surged a lot as the n value decreased or B_0 increased, even at a lower temperature (stack @30 K and bulk @77 K). The main reason is related to the metallic layers in the HTS tape, which is able to improve the stability in the centre of the superconducting layer. With the same engineering current density, stacks could trap more fields and fluxes compared to bulk from

previous research [96]. The overall heat generation might not change a lot when different n or B_0 applied to the stacks, since the current density in tape layers is quite uniform. The hotpots appeared in bulks could be avoided as much as possible in stacks.

(a)

(b)
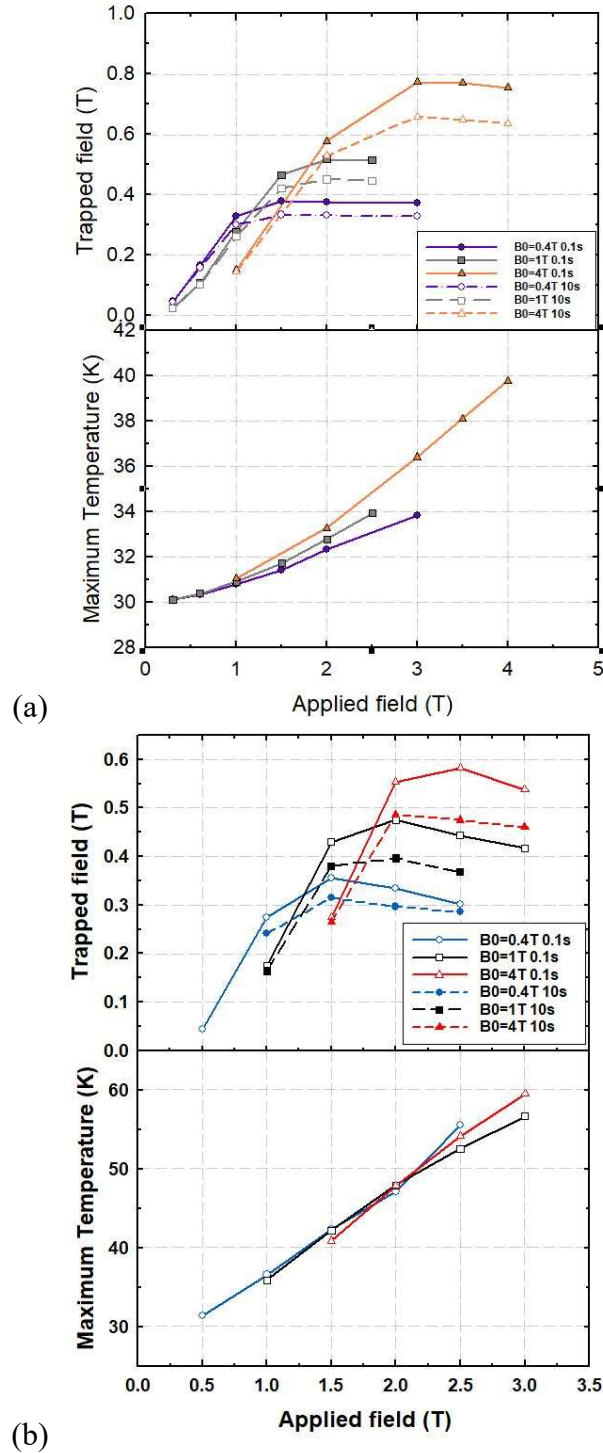
Figure 4.5: Comparison of trapped fields and maximum temperatures of a 20-layer (a) AMSC stack and (b) SuperPower stac at 30 K for different B_0 values in the Kim model measured 0.8 mm above the centre of the stacks at 0.1 s and 10 s.
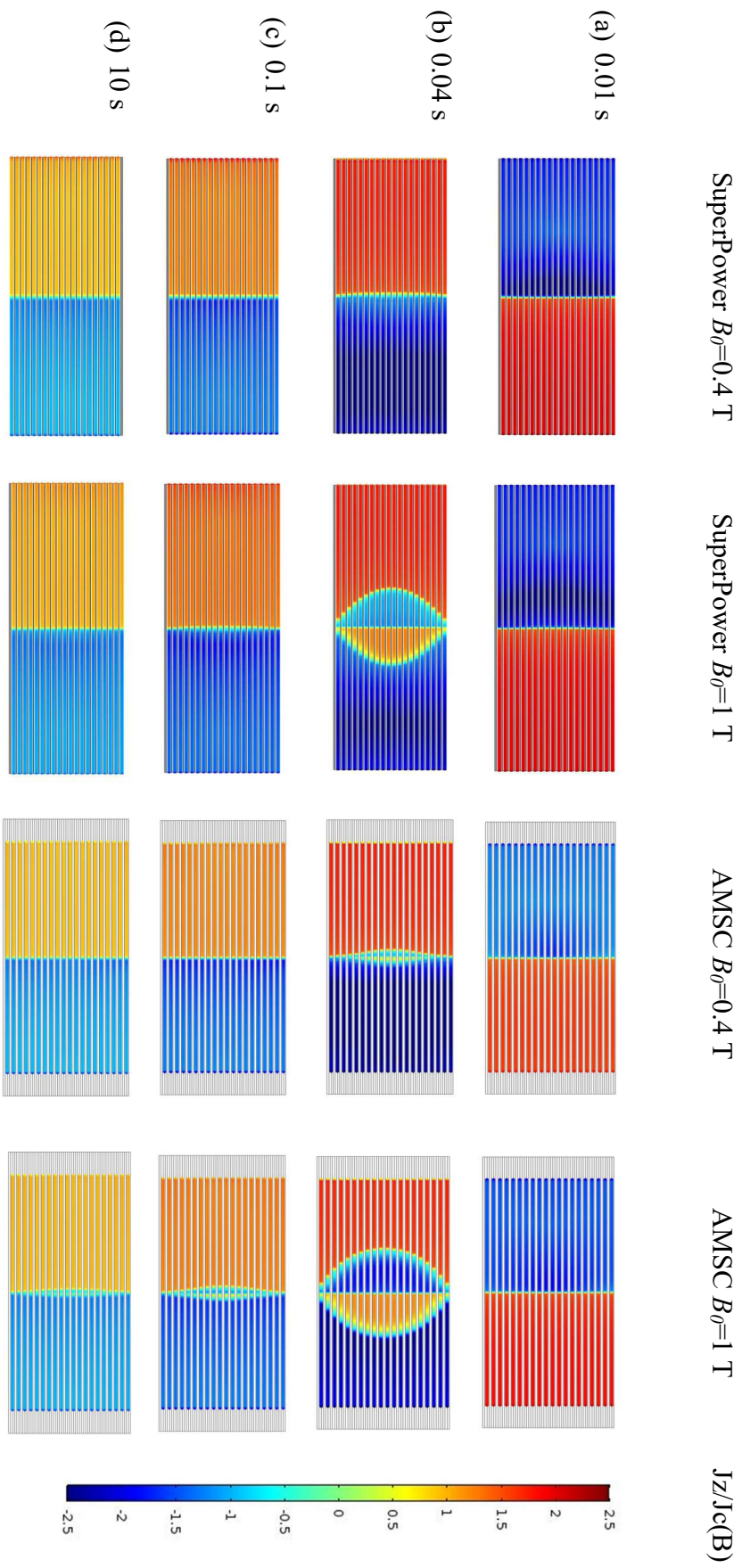
Figure 4.6: The normalised current distribution $J_z/J_c(B)$ of the SuperPower stack and the AMSC stack with an applied field of 2 T with different B_0 values at (a) 0.01 s, (b) 0.04 s, (c) 0.1 s, (d) 10 s. (The thickness of the HTS layer was exaggerated for visualisation. The figures of the cross-section of the stacks are not to scale.)

4.2 Influence of substrates on trapped fields of HTS stacks with and without a magnetic substrate

One of the most obvious effects on magnetic distribution of HTS tapes is the material of the substrates or stabilisers. Stacks with different substrates or stabilisers have different behaviours of trapping field. Understanding the properties of different materials of the substrates or stabilisers is essential in trapped field studies, especially for the choice of the best options of tape selection for practical applications.

Referring to A. Page's study [96], the influence of normal stabilisers on the trapped field has been analysed. According to the results, increasing the thickness of the silver layer raises the total trapped flux but decreases the central trapped field. The copper layer is detrimental to the central field and flux due to the effect of eddy current heating abandoning the enhancement of radial thermal conductivity [96]. Furthermore, it was also pointed out that the Hastelloy layer works as a heat sink. Zou et al. mentioned in the paper that less heat can be generated during PFM for tapes with metallic stabilizers of larger resistivity [78]. Further to their results, the roles of substrates during PFM need to be further investigated, especially the effect of magnetic properties of the substrates.

This chapter investigates the influence of substrates with and without magnetic materials of the 2G YBCO tapes by numerical methods. Different thicknesses and the effects of temperature of substrates will also be discussed. Experimental methods are not easy to be conducted, since the substrates and stabilisers of commercial tapes are fixed. Therefore, this section will be accomplished by simulated methods.

4.2.1 Substrates with and without magnetic materials

There are different types of substrates with different magnetic properties such as the non-magnetic substrate Hastelloy, weakly magnetic substrate RABiTS and strongly magnetic substrate Ni-alloy [56]. The most commonly used substrates in the 2G YBCO CC industry are Hastelloy and Ni–5at%W alloy (Ni5W). It is well known that the Ni5W alloy has high strength, good thermal stability and high magnetic properties compared to Hastelloy [142]. It is worthy to analyse whether the magnetic properties of substrates are important factors for trapping fields, especially for magnetic distribution and temperature rise.

In this section, two 20-layer sample stacks will be analysed at 30 K. One is the AMSC stack mentioned in Figure 3.1, where the function of relative permeability μ_r of the substrate, changed by an external magnetic field, is shown in Figure 3.3. The second is a self-defined stack with the relative permeability in the substrate layer set as a constant of one. As for the other stabilisers, the thickness and width of the two stacks are exactly the same. The only dissimilarity between these two stacks is the substrate. The substrate of the AMSC stack is magnetic and the substrate of the self-defined stack is non-magnetic. The magnetism of the substrate is the emphasis points in this part, therefore, $J_c(B, T)$ for both of the stacks were adopted the same schemes proposed in section 3.1.

The trapped fields in the centre of the top surface of the stack, the heat generation and the trapped fluxes for different substrates are compared in Figure 4.7, Figure 4.8, Figure 4.9 and Figure 4.10. The measurement point for the trapped centre fields was selected 0.8 mm above the surface centre of the stacks. The results show that the substrate with magnetic properties has a higher trapped field in the centre. The maximum trapped field for the AMSC stack is 24% larger than that of the self-defined stack with no magnetic substrate.

Moreover, the overall dissipated heat of the stack with a magnetic substrate is lower than that of the stack without a magnetic substrate. Most of the heat was generated in the YBCO layer, which can be observed from Figure 4.8. For other layers of the materials, the heats were almost the same for both stacks. The minimum heat dissipated in the substrates with and without magnetism and the generated heats for both substrates were almost equal, because the electrical resistivities for both substrates were set to be identical and were relatively higher than other stabilisers. Nevertheless, less heat is produced in the YBCO layer for the stack with magnetic substrate. It indicates that the contribution of magnetic property is capable of accelerating the dissipation of heat in the superconducting layer and enhancing the final trapped field.
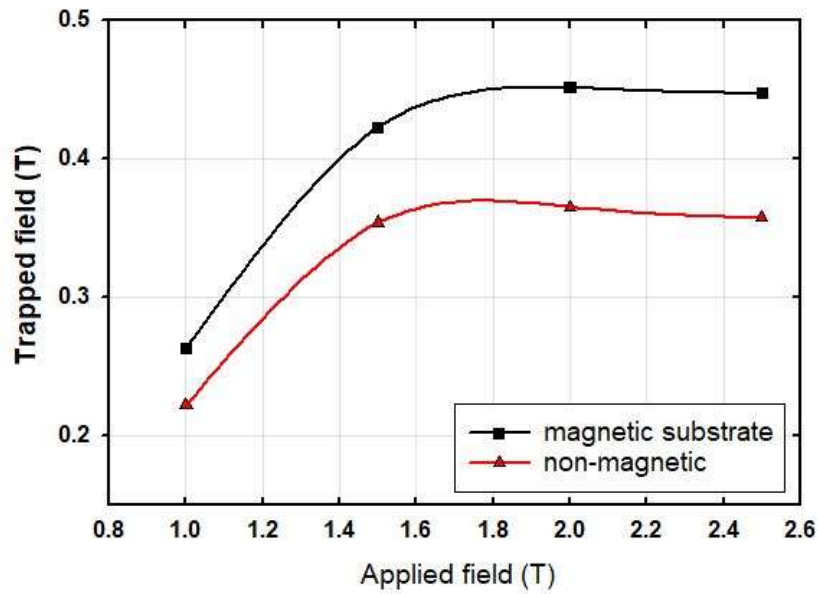
Figure 4.7: Comparison of trapped fields of a 20-layer AMSC stack with and without a magnetic substrate at 30 K measured 0.8 mm above the centre of stacks after 10 seconds.
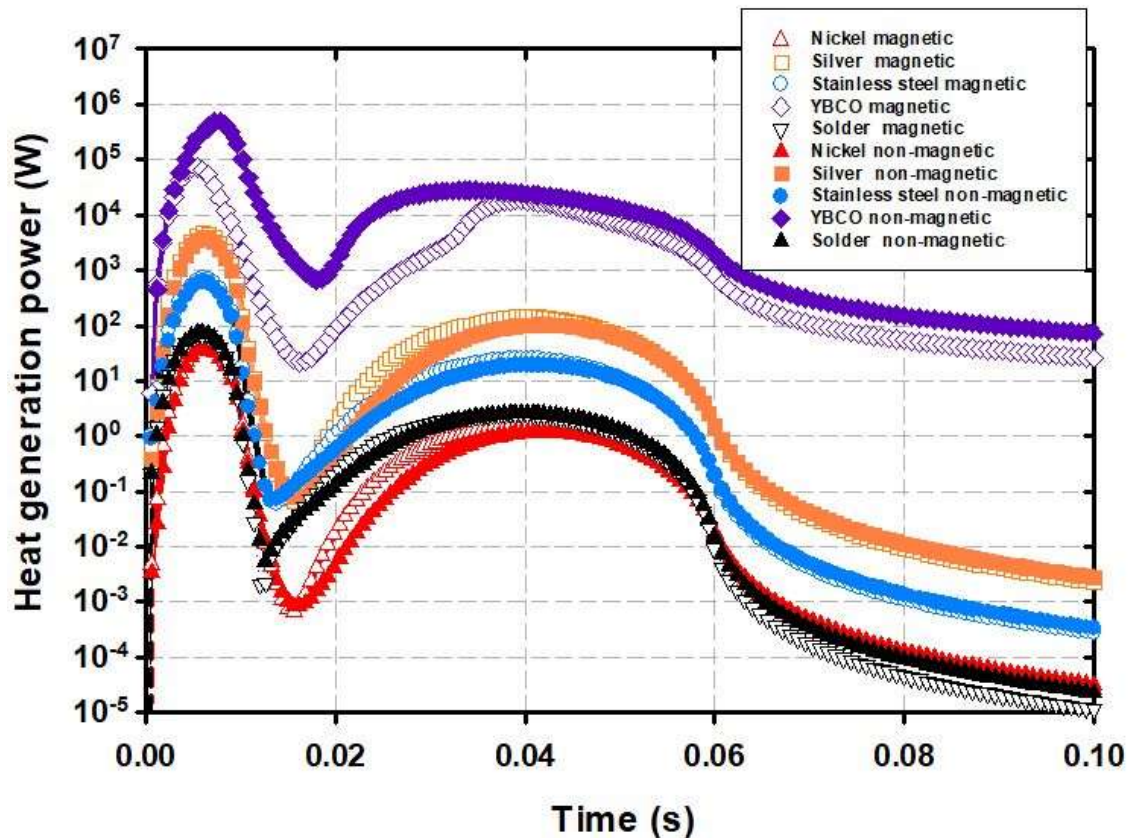
Figure 4.8: Heat generation power of different layers of materials during PFM for stacks with magnetic and non-magnetic substrate.

The distribution of trapped fields at 10 s for both stacks is shown in Figure 4.9. Given the trapped field profiles for both of the stacks, the trapped fluxes were defined at 0.8 mm above the surface from 0 mm to 12 mm on the x-axis. The total fluxes were calculated by:

$$\emptyset = \int B \cdot S = \iint B \cdot dxdz \tag{4.2}$$

The fitted magnetic field distribution shown in Figure 4.9, can be used in the integral in equation 4.2 in the direction of the x-axis. For stacks with a magnetic or non-magnetic substrate, the total trapped fluxes with different applied fields are shown in Figure 4.10. An overwhelming superiority of the trapped fluxes for the stack with a magnetic substrate is presented. A substrate with magnetic properties can improve the trapped field from the edges to the centre. Furthermore, when the applied field increases, the total trapped flux variance also grows from 15% to 34.4%.

When the external magnetic field came to 2 T, the superconducting layers of both stacks were saturated in the centre. However, the total magnetic fluxes of the stack with magnetic substrate still increased as the external magnetic field rose like Figure 4.10 shows. The reason is the magnetic substrate was not saturated yet at this point. Comparison of the magnetic field distribution of both stacks after the rise duration of single pulse is presented in Figure 4.11. The substrate with magnetism was not fully magnetised after magnetisation. The magnetic fluxes were able to penetrate the central section of the magnetic substrate layer of the stack as increasing the excitation field. All in all, the trapped fluxes could rise after the saturation point of the superconducting layer for the stack with magnetic substrate. However, it would remain constant or decline for the stack with non-magnetic substrate.
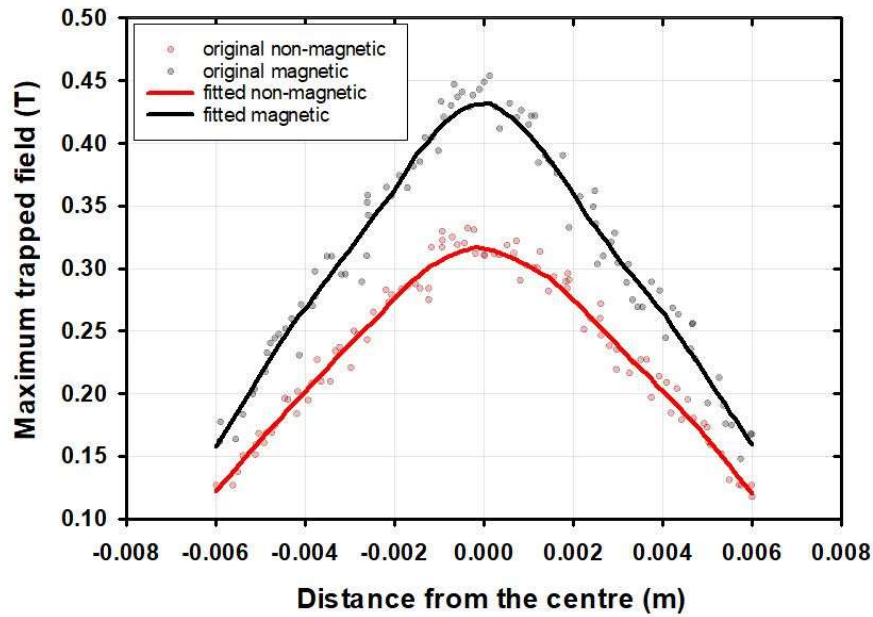
Figure 4.9: Comparison of trapped field profiles of a 20-layer AMSC stack with and without a magnetic substrate from the edge to the centre after 10 s with an external magnetic field of 2 T. The widths of the stacks are from -6 mm to 6 mm, which defines the region of trapped flux. The scatter plots are the original simulation results and the line plots are the fitted results.

Figure 4.10: Comparison of total trapped fluxes of a 20-layer AMSC stack with and without a magnetic substrate after 10 s with different external magnetic fields.

(a)

(b)
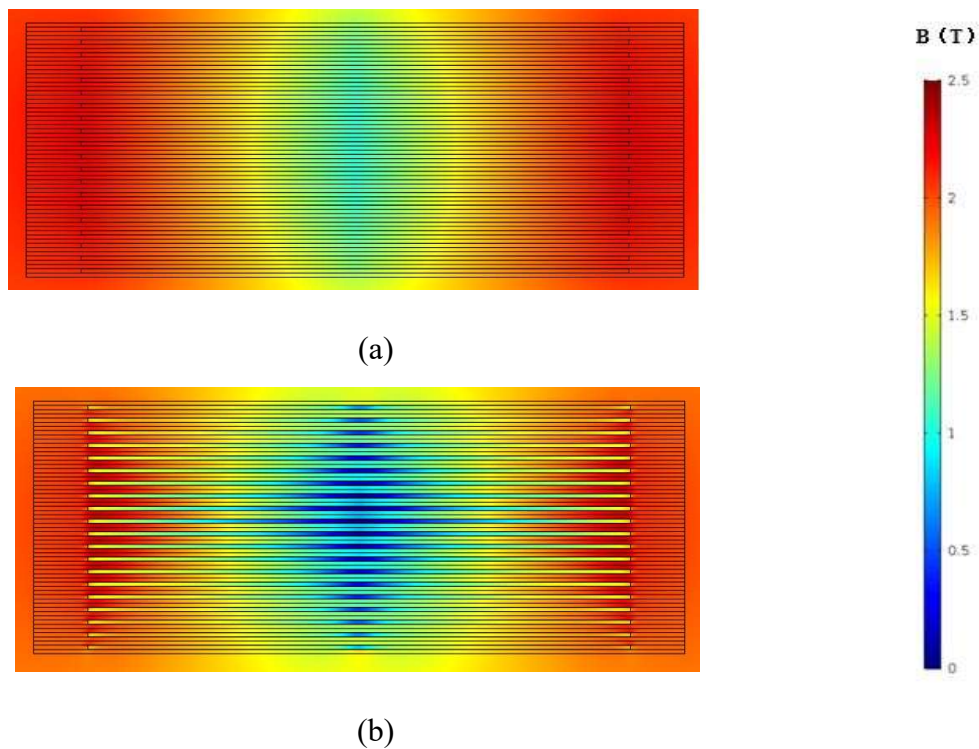
Figure 4.11: Comparison of magnetic field distribution of a 20-layer AMSC stack (a) without and (b) with a magnetic substrate at 30 K after 0.01s (ramp-up time).

The magnetic field distributions of the two stacks after evacuating the external field are compared in Figure 4.12. Since the stacks were largely cooled from the outer surface, most of the field was trapped in the superconducting layer during one pulse. The substrate with magnetic properties could trap field after the magnetisation process. However, there is almost no magnetic field maintained for the stack without a magnetic substrate. Due to flux pinning, the superconductor maintains a memory of its magnetic history in the form of a flux distribution after discontinuing to apply magnetic field. This memory field and the superconductor geometry turn to generate substantial internal fields in the substrate layer [143]. In consequence, the field retained in the substrate helped the stack to trap more field in the middle and edge areas. Thus, the trapped field and overall trapped flux were increased eventually.

(a)

(b)
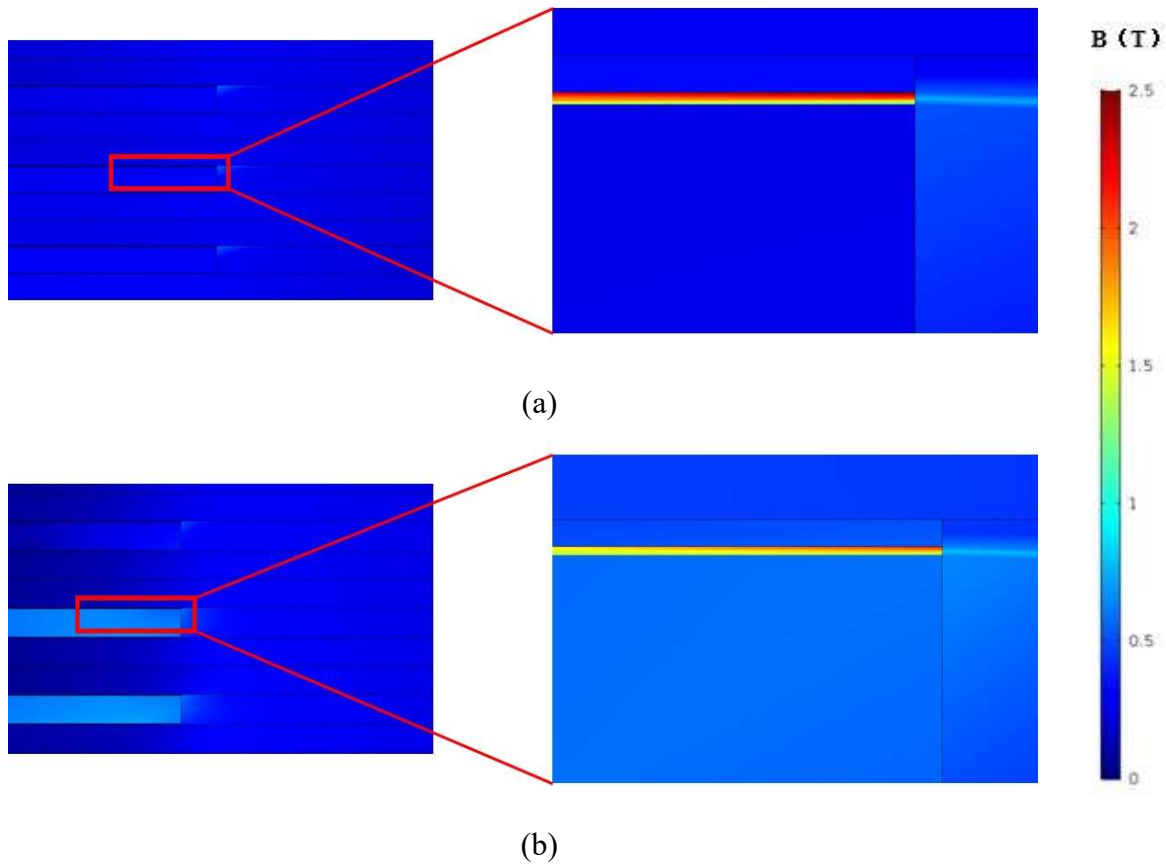
Figure 4.12: Comparison of magnetic field distribution of a 20-layer AMSC stack (a) without and (b) with a magnetic substrate at 30 K after 0.06 s (one pulse finished).

4.2.2 Substrate thickness

The thickness of the substrates is another essential issue that needs to be considered. In this section, the AMSC and SuperPower stacks with different thicknesses of substrates, and with and without magnetic properties will be compared. The configurations will be identical to those mentioned in the previous chapter. For the AMSC stack, the *H*-formulation model will be utilized. The *T-A* formulation model will be adopted for simulating the SuperPower stack. The real thickness of the nickel and Hastelloy substrates for the AMSC and SuperPower stacks are 75 μm and 50 μm, respectively. The compared thicknesses of the substrates in the AMSC and SuperPower models will be 45 μm, 60 μm, 75 μm and 35 μm, 50 μm, 75 μm, respectively.

4.2.2.1 Substrate with magnetic properties

For the AMSC stack, the magnetic substrate with 75 μm thickness shows better performance of trapping magnetic field in the centre, as shown in Figure 4.13 and Figure 4.14. The improvement of trapping field in the centre of the AMSC stack is approximately 3.9% larger compared to the stack with a thickness of 60 μm. However, the increase is not obvious when the edges of the stack are considered. Furthermore, less heat is generated during the pulse magnetisation for the stack with a thicker substrate. This indicates that the Ni5W substrate has the property of absorbing heat from the YBCO layer. The total flux shown in Figure 4.15 also illustrates the increase in the total trapped flux is only in the range of 1% to 6% when a lower external magnetic field is applied, which is mainly due to the increase in the centre. When the stack becomes fully magnetised, the total trapped flux of the thicker substrate is gradually surpassed by the thinner substrate. However, the difference is not that evident (within 1%).
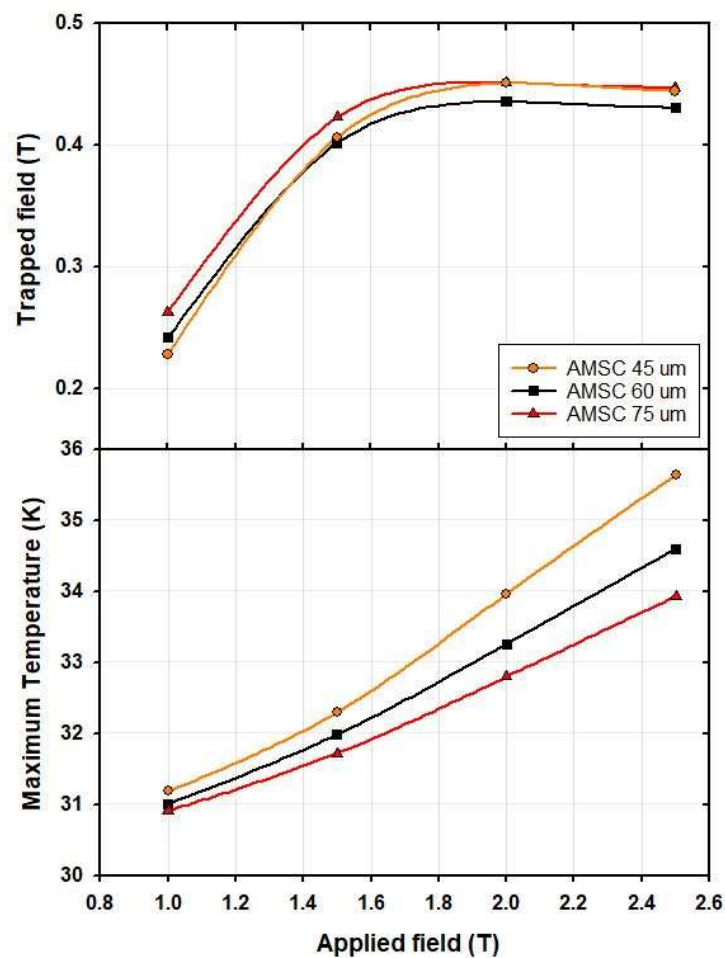
Figure 4.13: Comparison of trapped fields and maximum temperatures of a 20-layer AMSC stack with a magnetic substrate thickness of 45 μm, 60 μm and 75 μm at 30 K after 10 s.
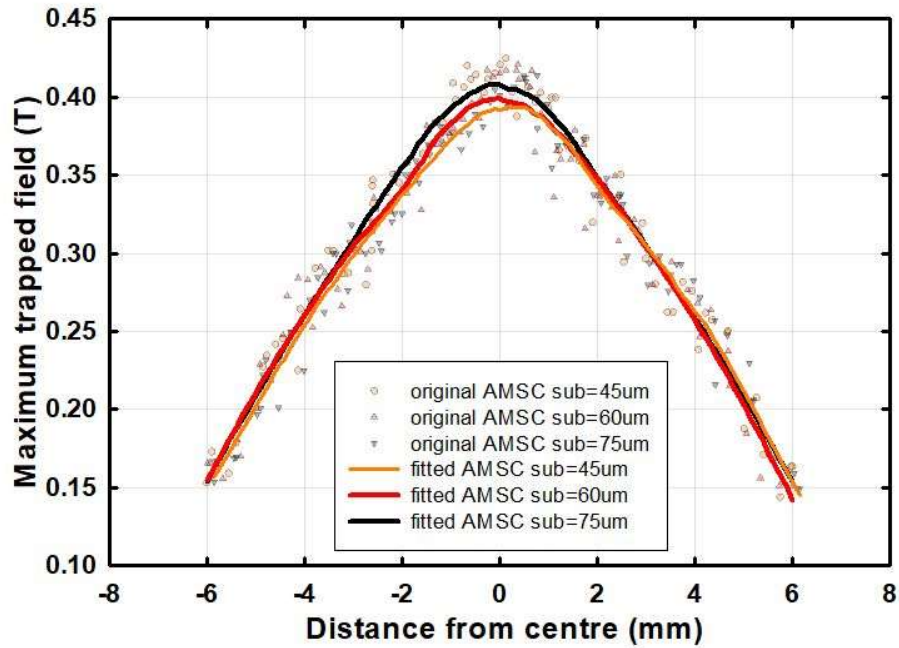
Figure 4.14: Comparison of trapped field profiles of a 20-layer AMSC stack with different thicknesses of substrates from the edges to the centre after 10 s with an external magnetic field of 1.5 T. The scatter plots are the original simulation results and the line plots are the fitted results.
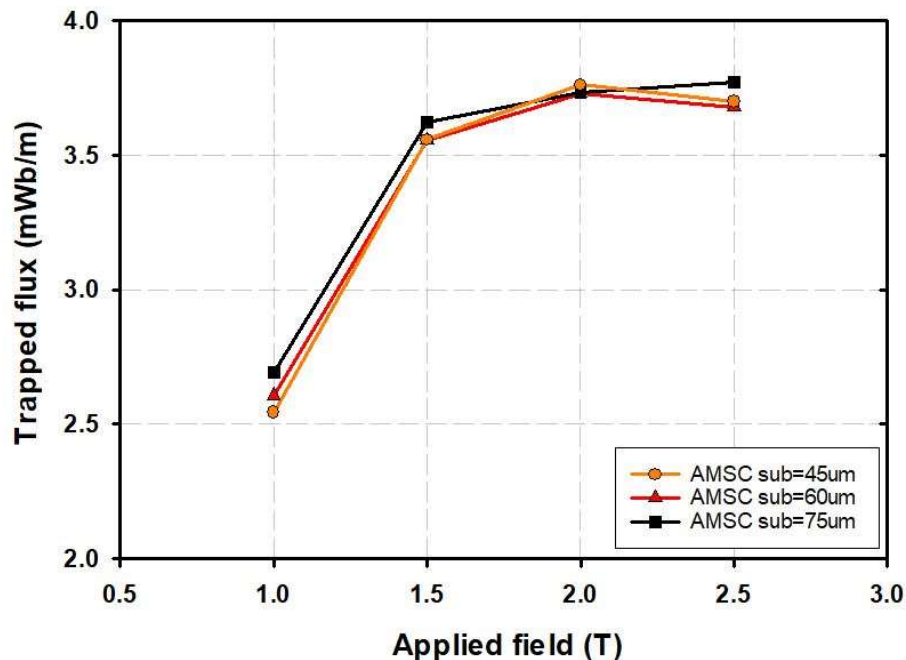
Figure 4.15: Comparison of total trapped fluxes of a 20-layer AMSC stack with a magnetic substrate after 10 s with different external magnetic fields.

4.2.2.2 Substrate without magnetic properties

Regarding the SuperPower stack, the dissimilarity of the centre trapped field with different thicknesses is not as obvious as the AMSC stack as results shown in Figure 4.16, Figure 4.17 and Figure 4.18. There is only a 1% growth when the thickness of the substrate alters. A stack with a large thickness of non-magnetic substrate can generate less heat, which is the same as the conclusion for a stack with a magnetic substrate. However, comparing the trapped fluxes for an entire stack, a stack with a thinner substrate is able to trap more flux. The total trapped flux for a substrate with the thinnest thickness increased by approximately 4% compared to the thickest one.

This reveals the fact that the impact of magnetic properties on the trapped flux is more important than the thickness. To increase the maximum trapped field, one should pay more emphasis to the magnetic properties of the substrate.
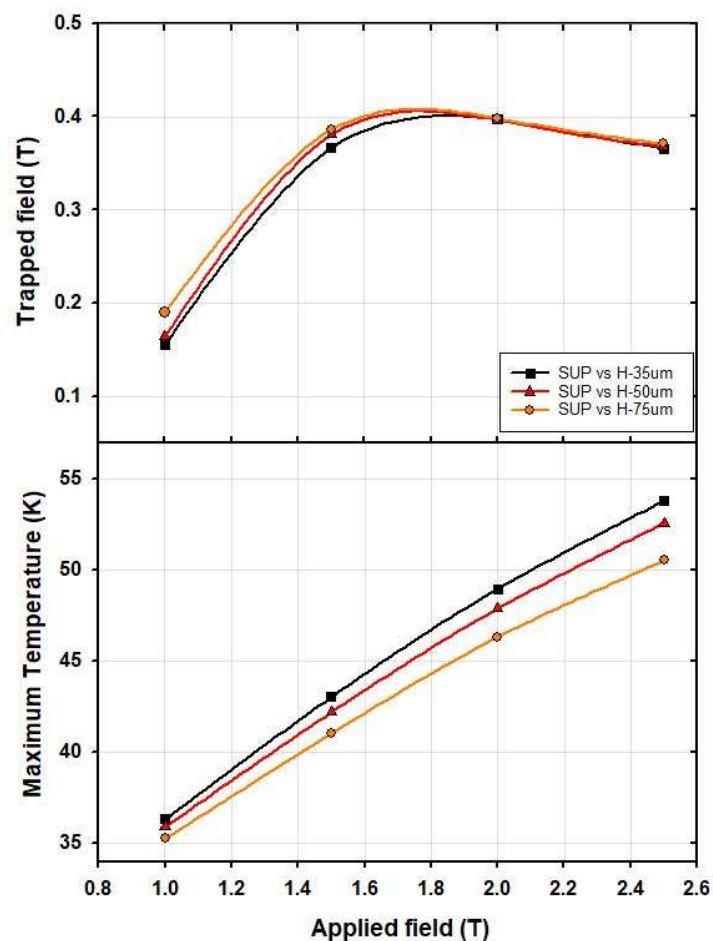
Figure 4.16: Comparison of trapped fields and maximum temperatures of a 20-layer SuperPower stack with a non-magnetic substrate thickness of 35 μm, 50 μm and 75 μm at 30 K after 10 s.
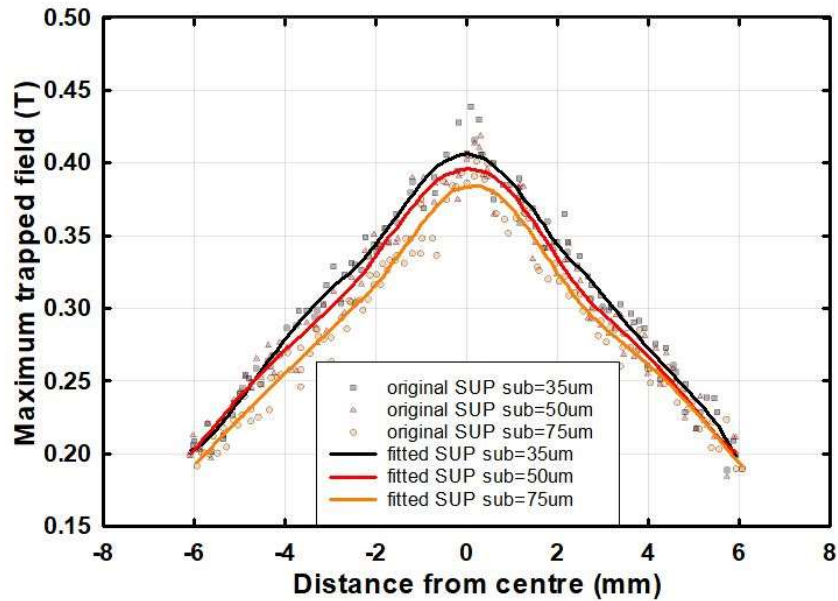
Figure 4.17: Comparison of trapped field profiles of a 20-layer SuperPower stack with different thicknesses of substrates from the edges to the centre after 10 s with an external magnetic field of 2 T. The scatter plots are the original simulation results and the line plots are the fitted results.

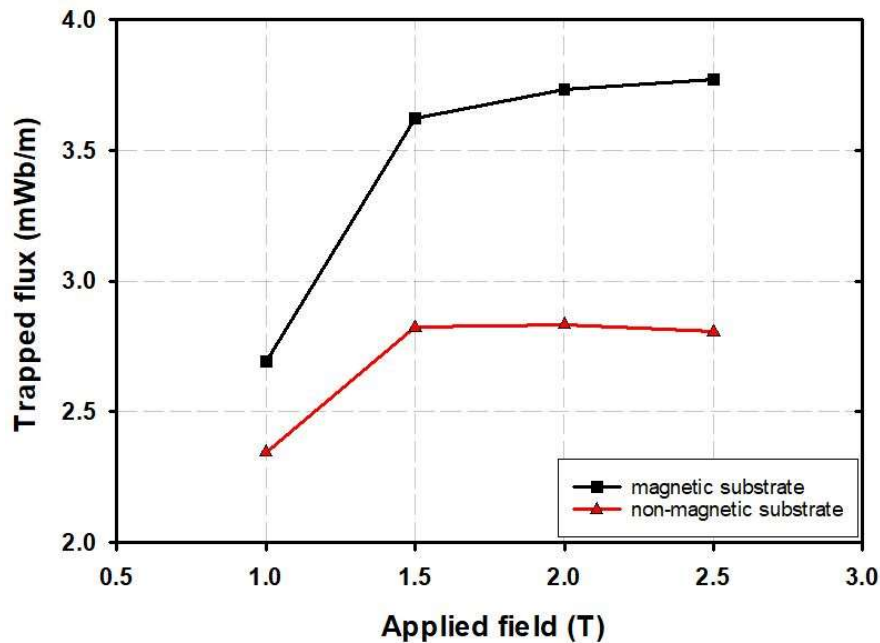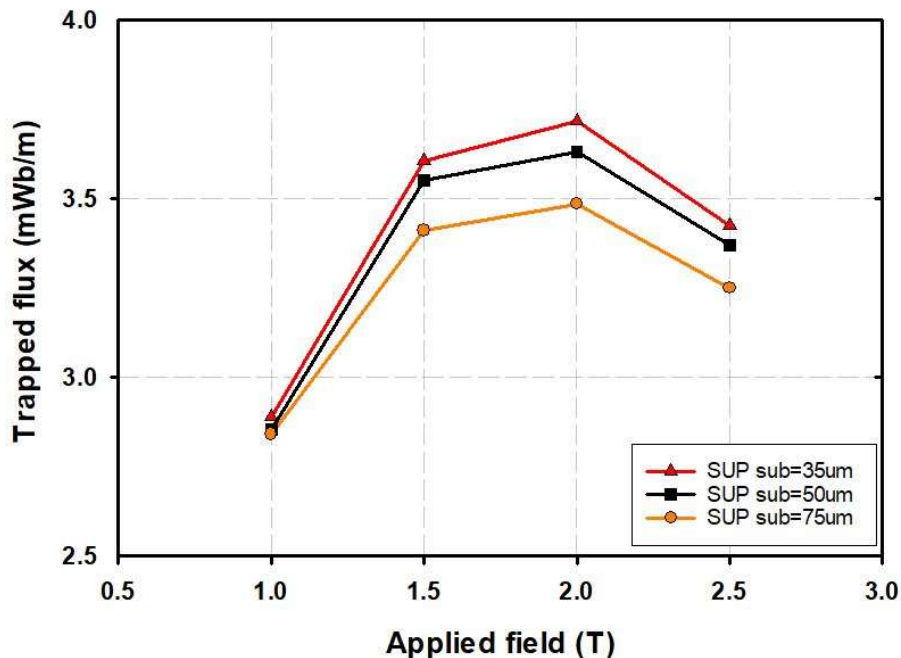**Figure 4.18:** Comparison of total trapped fluxes of a 20-layer SuperPower stack without a magnetic substrate after 10 s with different external magnetic fields.

4.3 Conclusion

In this chapter, the trapped fields of two HTS stacks with and without magnetic substrates were compared in 2D thermal-effective FEM models. The n value in the E-J power law and the B_0 value in the Kim model were chosen to be the variables in two scenarios which were analysed and results presented in section 4.1. The simulation results for both of the stacks illustrated that smaller n values give rise to sharp decreases of trapped field after a single-pulse magnetisation and also result in larger heat dissipation. A short-time quench appeared during the ramp-up duration with current surge for $n = 8$, which highlighted that the selection of the n value should not be too small. Moreover, although the trapped field increased with the increase of the B_0 value, the maximum temperature rise did as well. Hence, the maximum trapped field will be limited by a model with a larger B_0 value. Thus, the definition of $J_c(B)$ in simulations is of significance.

The magnetic properties and thickness of substrates in the stacks was investigated in section 4.2. The trapped field in the centre, the trapped flux for the entire surface and the magnetic field distribution, as well as the temperature variation were all compared. The results showed that a substrate with magnetic properties has better performance with trapping field from the edge to the centre of stacks no matter whether the stack was saturated. The trapped fluxes can be boosted for the stack with magnetic substrate at over-magnetization stage. The remaining internal fields in the magnetic substrate after evacuating the applied field are also capable of assisting the stack to trap more field and fluxes in the middle and edge areas. Therefore, the trapped field and total trapped fluxes will be larger than the stack without a magnetic substrate.

For a stack with a magnetic substrate, the trapped field in the centre region rises with the increase of thickness but the trapped field at the edge is almost constant. In terms of a stack with a non-magnetic substrate, the conclusion is reversed. For both types of substrates, there is no such difference of trapped field and flux for various thicknesses of substrates. However, the dissipated heat increases with the decrease of thickness of a substrate. This indicates that the main aspect depending on the total trapped flux and trapped field is the magnetic properties of the substrate layer instead of its thickness.

Chapter 5   Experiments   of   pulsed-field

magnetisation of HTS stacks

A number of research groups have been investigating trapped field stacks and have achieved great breakthroughs [19, 96, 137, 144-151]. The experimental research on pulsed-field magnetisation of stacks still requires further investigation, especially the mechanical and thermal properties. In this chapter, two different stacks are magnetised (with magnetic and non-magnetic substrates) using the facilities built in our laboratory. The magnetisation circuits are modified, which is supposed to give rise to different pulses with various ramp-down duration times and different trapped field and will be compared in section 5.3.4. Multi-pulse magnetisation will also be tested and compared with the single-pulse magnetisation for the AMSC stack with a magnetic substrate at a lower working temperature in section 5.4. The impact of temperature on the trapped field is also going to be analysed in this chapter.

5.1 Overview of trapped field magnetisation of stacks

HTS tapes can be cut and stacked as HTS stacks to trap magnetic field when the superconducting layer is penetrated by currents, which is similar to HTS bulks. HTS stacks have great potential to replace conventional permanent magnets and be widely used in different applications. Extensive simulated and experimental research has been conducted on HTS bulks and their promising applications including electric machines, NMI/ MRI devices, energy storage flywheels, magnetic bearings, superconducting levitations, etc. [65, 152]. In this chapter, research on the TFM of HTS stacks will be briefly reviewed and summarised.

As mentioned in section 2.4.1, ZFC or FC and PFM are typical magnetisation methods used in the majority of the research conducted on the magnetisation of HTS stacks. The achievements

can be categorised into two areas: 1) alternating the materials or arrangements of the stacks to trap higher field, and 2) improving the magnetisation techniques to provide more compact, stable, cost-effective and efficient magnetisation.

It is known that the commercial tapes produced by different manufacturers vary from each other. Even from the same manufacturer, there are still several options of tapes to choose from. There are various substrates and stabilisers, different widths or thicknesses, different manufacturing techniques and different arrangements or structures of HTS tapes, which give rise to diverse trapped field potential of stacks. The effect of stabilisers on superconducting tape magnetised by a sequence of pulses has been previously investigated. The different materials of stabilisers play different roles in pulse-field magnetisation, which is related with temperature rise as well [96]. Extra solder (like Pb–Sn) for HTS stacks could degrade the superconducting properties but not a lot. However, stacks could be tighter after soldering, which decreases the thickness of stacks. Therefore, the engineering critical current density increases, thereby enhancing the trapped field [151]. Square stacks with a larger width are able to trap more field according to different experimental results [66, 144, 149, 150, 153]. Compared to square stacks, rectangular stacks might not trap more field even with increased size [150]. Increasing the layers or height of the stacks does increases the trapped field and flux in some cases but leads to lower cooling efficiency at the same time. Furthermore, when the height of the sample approaches the width or diameter of the stacked tapes, the trapped field or flux will saturate [66, 137].

Different arrangements of HTS stacks have been tested by field cooling magnetisation methods [145, 154-156]. A more uniform trapped field profile was observed by a criss-cross arranged stack. Three tape segments were placed in an aluminium sample holder of dimensions 36 mm × 36 mm × 15 mm vertically and horizontally in different layers. The maximum or minimum trapped field values were associated with the overlapped regions or the overlapping edges of the superconducting tapes [154, 155]. According to the results, more arrangements have been investigated such as the superconducting tape offcuts from a Roebel cable stacked in different configurations, angled stack, angled stack with ferromagnetic (FM) plate, etc. [145, 156]. These results show that new arrangements can produce more uniform trapped field compared with a straight arrangement, especially the angled stack with FM plate, which can also increase the magnitude of the trapped field. To achieve a higher trapped field, a FM plate with a higher permeability and thinner thickness will be a better choice [145]. The trapped field ability of a superconducting stack achieved a breakthrough of 17.7 T in recent research using a hybrid

stack, which used the SuperPower tape and the American Superconductor (AMSC) tape together. The design took full advantage of the higher current and larger stack size, and the result was even higher than the maximum trapped field of a bulk (17.6 T) [18, 19].

An applied pulsed-field is also a significant factor in the magnetisation of HTS stacks [78, 126]. The applied pulses could be single or multiple. For single-pulse magnetisation, the optimal applied field gives rise to the maximum field or flux trapped afterwards. The stack will be either under-magnetised or over-magnetised when the applied field is lower or higher than the optimal applied field, respectively [126]. There are several multi-pulse techniques including successive pulsed-field application (SPA), iteratively magnetising pulsed-field method with reducing amplitude (IMRA) and multi-pulse technique with step-wise cooling (MPSC). All of these methods can promote the trapped field. MPSC requires a second cool-down step to achieve higher amplitude of successive pulses afterwards. The other two methods do not need to alter the working temperature during the process, which is more accessible. Compared to IMRA, pulses with the same amplitude (SPA) will magnetise a stack more rapidly, which leads to lower trapped field. Moreover, the trapped field can be improved by applying an external field with a smaller amplitude interval or a larger starting amplitude [126].

5.2 Stack geometry and material properties for HTS stacks with and without a magnetic substrate

Two types of tapes were compared and the configurations of the tapes are presented in Figure 3.2 and Table 5.1. For the SuperPower tape (type SCS12050), each layer has the same width (12 mm). However, the width of the stabiliser layer (stainless steel 12 mm) and solder layer (2 mm) in the AMSC (type 8602) tape vary from the other layers (10 mm). Therefore, the width of the YBCO layer in the SuperPower tape is 2 mm wider than that in the AMSC tape. Another aspect that needs to be compared is the substrate layer. The AMSC tape contains a magnetic layer, Ni-5W, which can be affected by the external magnetic fields. However, the substrate in the SuperPower tape is Hastelloy, which is a non-magnetic material. The AMSC tape is approximately 1.5 times thicker than the SuperPower tape, which results in a lower engineering critical current density. The trapped field mechanical limit is determined by the tensile yield strength of the substrates [19, 157]. To take full advantage of the trapped field stacks, it is proposed that the yield stress is the most tolerable stress.

Apart from the buffer layers, all the parameters are based on the real AMSC and SuperPower architecture. The buffer layers are too thin which are ignored in both the AMSC and SuperPower stacks. Furthermore, the tapes layered in the stacks are considered to be cut exactly the same.

Table 5.1: Tape configuration

Manufactory	AMSC	SuperPower
Type	8602	SCS12050
Average width	12 mm	12 mm
YBCO layer thickness/width	1 μm/10 mm	1 μm/12 mm
Silver layer thickness/width	3 μm×2/10 mm	2 μm×2/12 mm
Substrate thickness/width	75 μm/ 10 mm (Ni-5W)	50 μm/ 12 mm (Hastelloy)
Stabilizer thickness/width	75 μm×2/ 12 mm (Stainless steel SUS 316L)	20 μm×2/ 12 mm (Copper)
Solder thickness/width	82 μm×2/2 mm	-
Total thickness	0.232 mm	0.095 mm
Critical current (1 μV/cm)	260 A@77 K, 0T	317 A@77 K, 0T
Yield Strength of substrate	257 MPa (Ni-5at%W)	700 MPa (Hastelloy)
Maximum rated tensile stress (RT)	200 MPa	550 MPa

5.3 Pulse field magnetisation for the HTS stacks with and without a magnetic substrate

5.3.1 Preparation of HTS stacks

Simulations focusing on the magnetic and non-magnetic substrates have been presented and compared in the previous chapter. To validate the simulation results, two stacks manufactured from SuperPower and AMSC tape were tested using the single pulse magnetisation technique. The configurations are the same as the details listed in section 5.2. Both stacks were cut from the commercially available tapes into 12 mm x12 mm squares and stacked together tightly. The comparison of the trapped field of these two types of stacks has not been tested previously. Due to the limitation of the applied voltage source and capacity of capacitance, 5-layer stacks were the best prototypes to be measured in the laboratory.

To ensure that the samples were fixed in a G10 holder, the testing sample was firstly held with Kapton tape and then a hall sensor (connected to a NI card) on a plastic strip board was also secured, as shown in Figure 5.1. The G10 holder was cut with a 12 mm wide gap in the centre
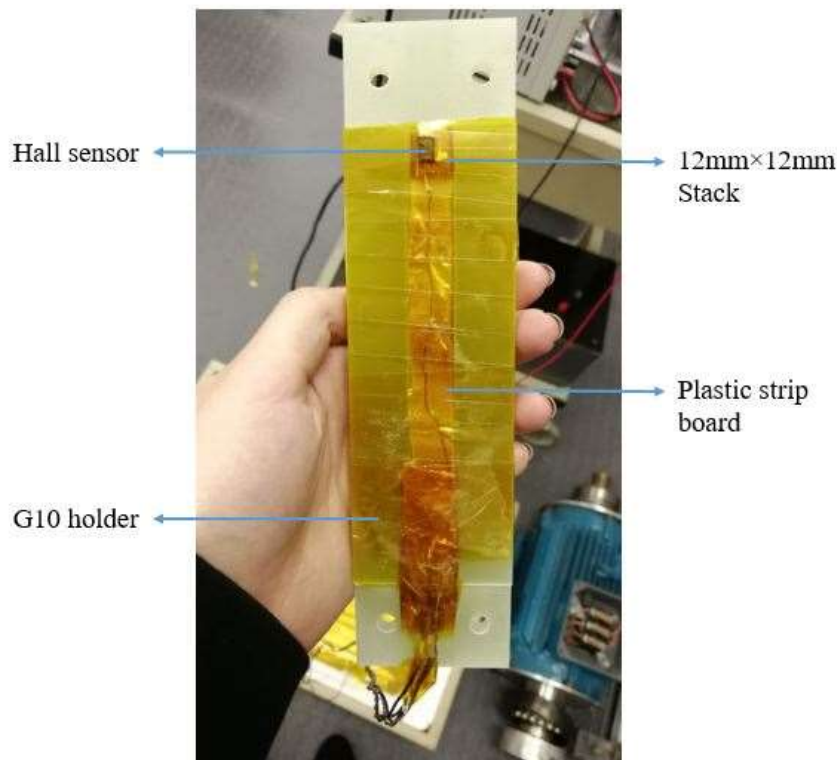
Figure 5.1: Testing stack sample fixed by Kapton tape on a plastic strip board in a G10 holder.

where the plastic strip could fit. The G10 holders were fixed with long screws to minimise movement and dislocation. There is a wide gap between the two copper-made magnetisation coils where the samples can be inserted. The length between the centre and the edge of the coils on the sample holders were measured and marked to ensure that the stacks were tested in the centre of the coils.

5.3.2 Test rig and experimental process

The explanation of the diagram of the test rig in Figure 5.2 was previously discussed in section 2.4.1. The whole systems were built with my colleagues. Figure 5.3 presents the charge part of the experimental system. It includes a power source up to 50 V, a capacitor bank series-connected by three capacitors, an IGBT (insulated-gate bipolar transistor), a diode placed in anti-parallel with the IGBT to bear current in the opposite direction, a switch to control the charging time and a DC power source to apply the control signal for the IGBT. For the discharge part, there is an additional diode to ensure no opposite current can flow back to the capacitor bank and connect to the magnetisation coils.
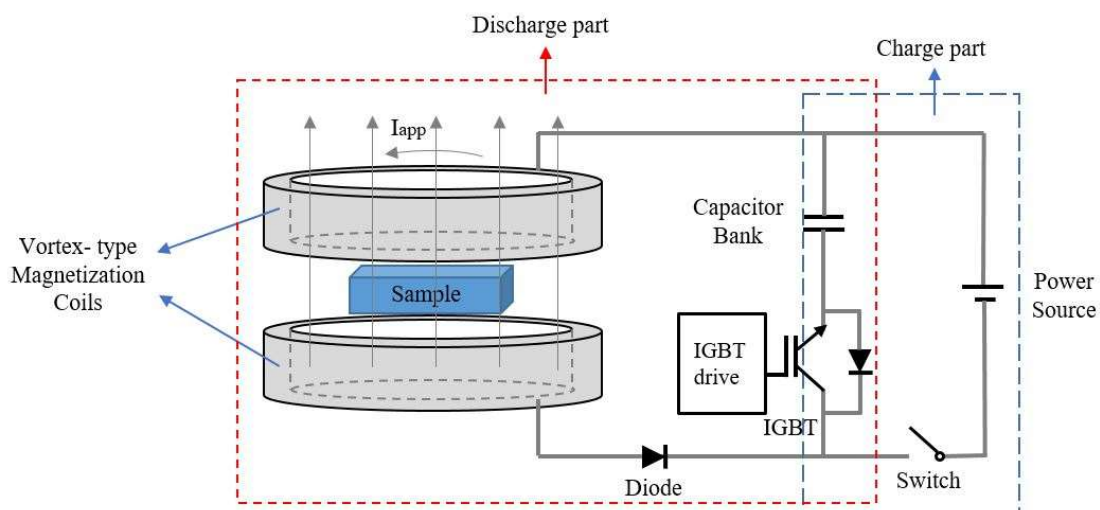
Figure 5.2: Diagram of the experimental test rig for pulse field magnetisation of a sample.

The magnetisation coils used in this research were vortex-type, which can trap more fields compared with a traditional solenoid coil. The two identical copper coils were held by large G10 holders, as shown in Figure 5.4. Some plastic wires were bonded through the holes drilled in the G10 holders for lifting and moving the magnetisation system in and out of the liquid nitrogen tank conveniently.
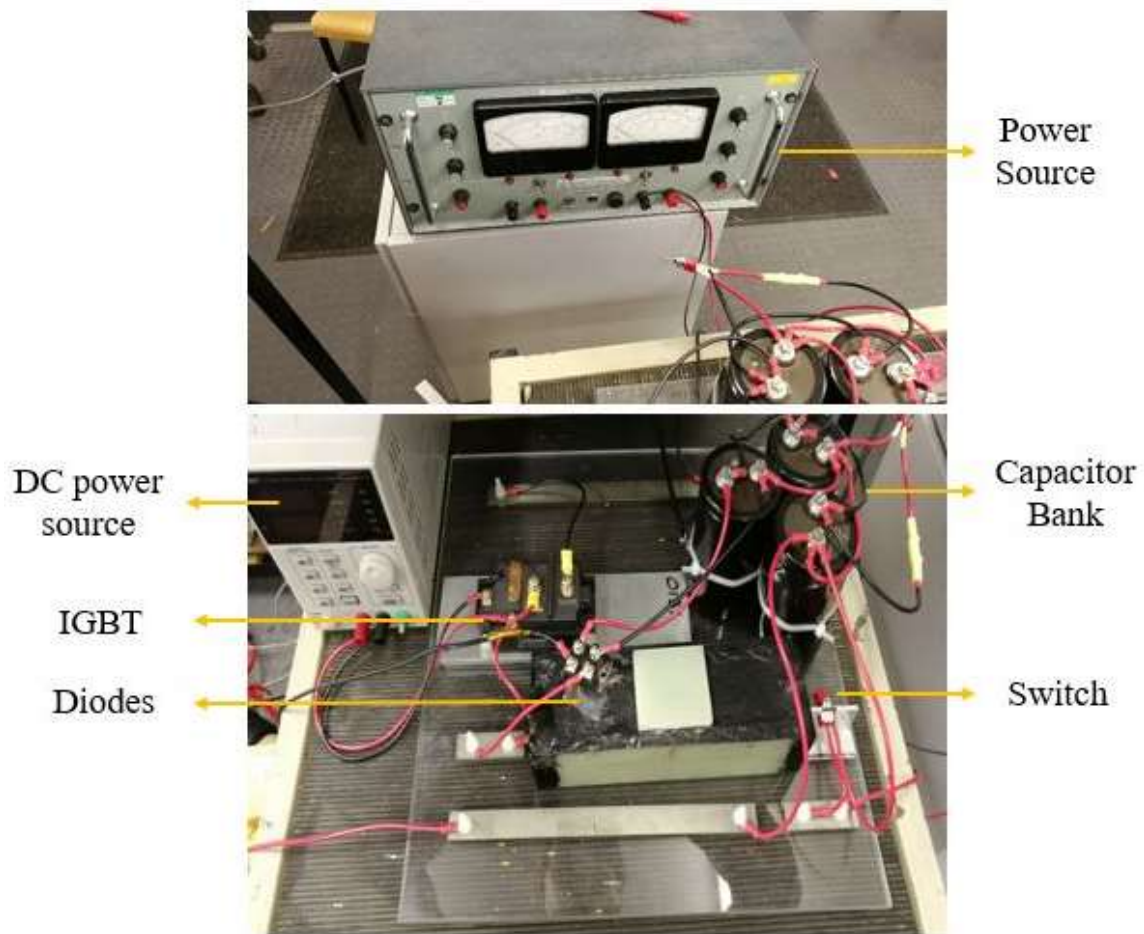
Figure 5.3: Experimental test rig for single pulse magnetisation. Upper picture is the applied source connected with a switch. The below picture is the capacitor banks connected with an IGBT and diodes. There is also an exciting DC power source.

Figure 5.4: Magnetisation copper coils held by G10. Plastic wires are bonded through the holes drilled in the G10 holders for lifting and moving the magnetisation system in and out of the liquid nitrogen tank conveniently.

The experimental process is shown in the flow chart in Table 5.2. The entire process took up to 10 s at a temperature of 77 K. The process starts when the stacks are fully cooled down to 77 K. After each experiment, the test sample needs to be warmed up to room temperature to ensure that the stacks are completely demagnetised before the next test is started. The applied source voltage ranged from 10 V to 50 V, corresponding to a maximum applied field ranging from 0.051 T to 0.283 T. The thickness of the hall sensor is approximately 0.8 mm, which meant that the trapped field was measured 0.8 mm above the centre of the sample stacks.

Table 5.2: Experiment process for single-pulse magnetisation

```
┌─────────────────┐      ┌─────────────────┐      ┌─────────────────┐
│  Put the sample │      │  Cooled down    │      │   Alter the     │
│    into the     │  →   │  to 77 K in the │  →   │   swtich to     │
│  magnetisation  │      │      LN2        │      │  charge mode    │
│     coils       │      │                 │      │                 │
└─────────────────┘      └─────────────────┘      └─────────────────┘
        ↓
┌─────────────────┐      ┌─────────────────┐      ┌─────────────────┐
│   Change the    │      │   Alter the     │      │  Switch on the  │
│    applied      │  →   │   swtich to     │  →   │  control signal │
│    voltage      │      │   discharge     │      │    for IGBT     │
│                 │      │     mode        │      │                 │
└─────────────────┘      └─────────────────┘      └─────────────────┘
        ↓
┌─────────────────┐      ┌─────────────────┐      ┌─────────────────┐
│   Record the    │      │  Switch off the │      │ Stop recording  │
│  results in the │  →   │ control signal  │  →   │  after 10 s and │
│  Labview at the │      │    for IGBT     │      │   save files.   │
│    same time    │      │                 │      │                 │
└─────────────────┘      └─────────────────┘      └─────────────────┘
```
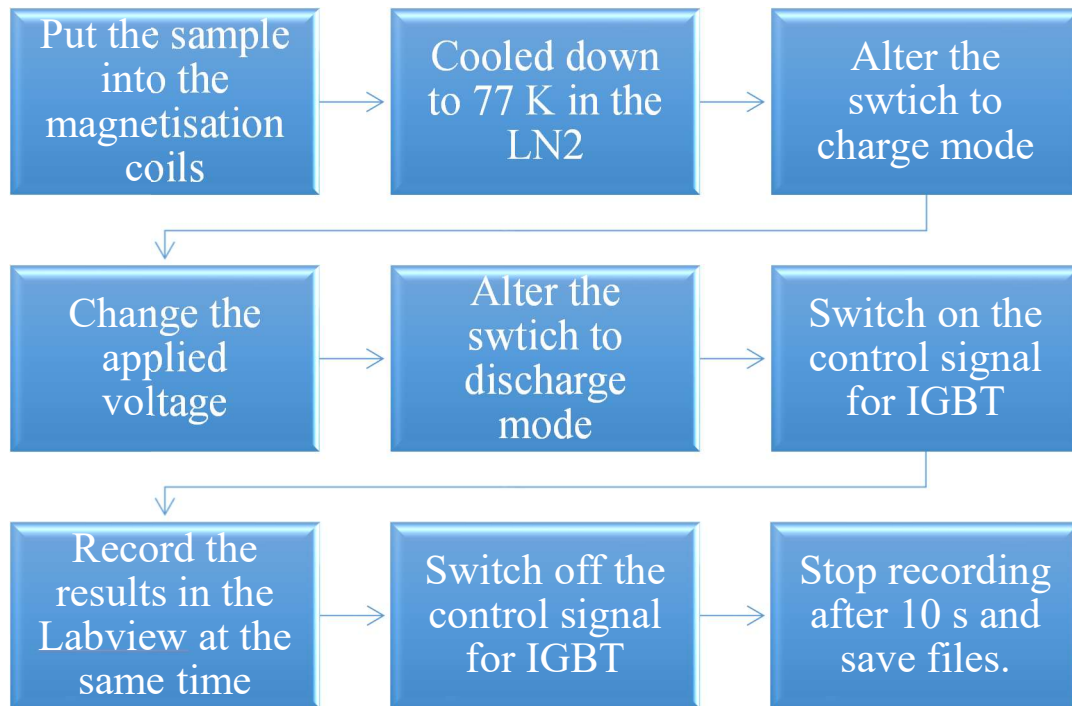
5.3.3 Results and analysis

According to the results presented in Figure 5.5, the two stacks could trap almost the same value of field with a lower applied field of 0.05 T. However, when the applied field was increased, the trapped field of the AMSC stack increased more than that of the SuperPower stack. The AMSC stack saturated when the applied field reached approximately 0.3 T, but the SuperPower stack saturated with an applied field of 0.25 T. This means that the magnetisation speed of the SuperPower stack is faster than the AMSC stack. When the 5-layer AMSC stack was fully magnetised, the trapped field was 0.0378 T in the centre. For the 5-layer SuperPower stack, however, only 0.0291 T was trapped. Therefore, for the same designs of stacks, the AMSC stack can capture more flux in the centre when the same external magnetic field is applied.
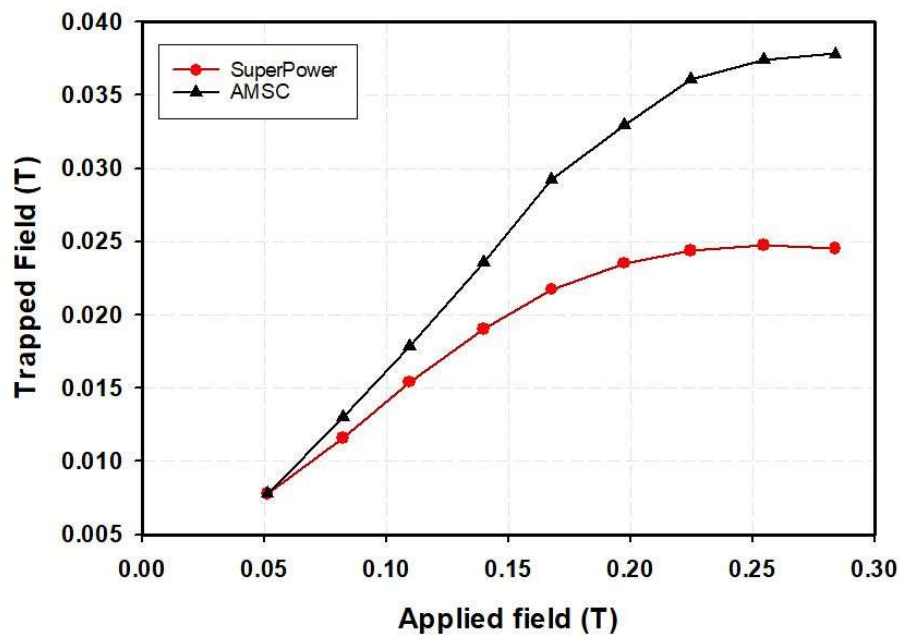
Figure 5.5: Comparison results of trapped field between the 5-layer AMSC stack and the SuperPower stack with an applied field ranging from 0.051 T to 0.283 T.

With a larger thickness and a lower critical current, the critical current density of the AMSC stack is supposed to be lower than the SuperPower stack. The smaller the critical current density, the lower the trapped field [151]. Thus, the critical current and tape thickness may not be the main reasons of this phenomenon. The reason might be associated with the magnetic substrate of the AMSC stack. Applying a higher magnetic field means that the magnetic substrate is penetrated with more flux. Flux will remain in the substrate nickel layer after removing the external magnetic field, which will boost the contiguous superconducting layer to trap more field. The experimental results also confirm the modelling result, which showed that the thickness of the substrate layer cannot affect the trapped field value significantly. However, the magnetic properties of the substrate layer do affect the trapped field value.

Figure 5.6 shows the trapped field measured during a single pulse for the SuperPower stack. The ramp-up time for the different applied voltages was the same whereas the ramp-down time was linear with the applied field. For an applied voltage of 10 V, the ramp-down time of the applied field was approximately 0.01 s. With a 50 V applied voltage, however, the ramp-down time increased to 0.033 s. The larger the applied field, the longer the ramp-down time duration. The trapped field in the stack reached saturation when the applied voltage was over 40 V. The

different ramp-down time durations were caused by the modification of the capacity of the capacitance bank. To determine whether the different ramp-down time durations affected the trapped field, another comparison experiment was conducted, which is presented in the following subsection.
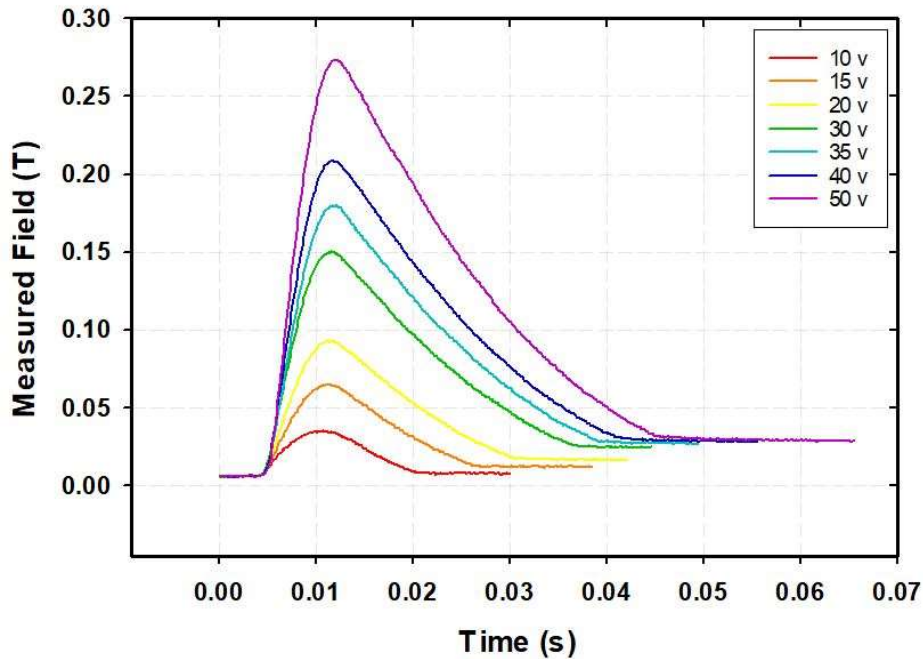
Figure 5.6: Trapped fields of a 5-layer SuperPower stack at 0.8 mm above the centre with different applied voltages over a period of time.

5.3.4 Influence of ramp-down time of pulses

After decreasing the capacity of the capacitor bank, a test was conducted to investigate whether the difference of ramp-down time influenced the final trapped field value in the centre of the stack. Although the same source voltages were applied, the ratios of the voltages and external fields were not identical. Comparison results are presented in Figure 5.7. For the 5-layer SuperPower stack with no magnetic substrate, the trapped field value with a longer ramp-down time is higher than the one with the same ramp-down time. The testing results with different applied voltage for the stack with different ramp-down time were shown in Figure 5.6. When

the applied field was slowly dropped down to zero, the duration of flux within the stack will be longer. As a result, more field can be captured during a longer ramp-down time.

The experimental results prove the theory that the trapped field increases by extending the duration of the pulse [144]. The fact that the stack can trap more field by employing the ZFC magnetisation method compared to the PFM also make sense. Due to the limits of the voltage source, a higher magnetic field could not be generated and therefore, the situation of over-magnetisation was not able to be determined.
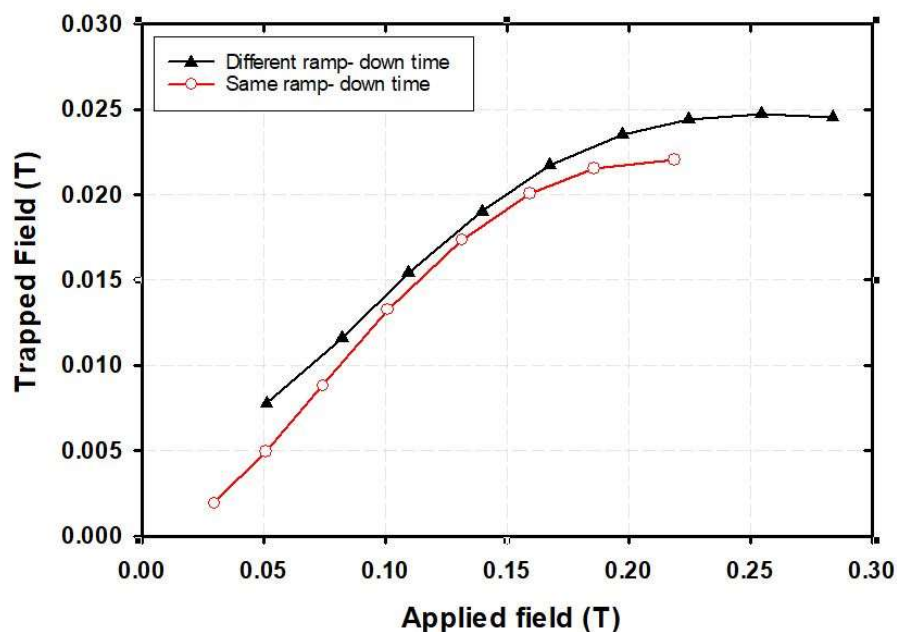
Figure 5.7: Comparison results of trapped field of the 5-layer SuperPower (SUP) stack with different and same ramp-down time with an applied field ranging from 0.03 T to 0.283 T.

Further work needs to be conducted with more hall sensors in an array to measure the profile of the trapped field of the stack and also, thermal sensors to detect the temperature change during the pulsed-field magnetisation. Therefore, the trapped field value at the edge of the stack and the impact of temperature can be investigated.

5.4 Pulse magnetisation for stack with a magnetic substrate

5.4.1 Preparation of AMSC stacks

The sample tested in this subsection was a 20-layer AMSC stack. The type of AMSC tape was 8602, which is the same as the tape discussed in section 5.3. Figure 5.8 (a) shows a comparison between the 20-layer SuperPower stack (left) and the AMSC stack (right). Obviously, the height of a 20-layer AMSC stack is larger than the SuperPower stack due to the higher thicknesses of the substrate and stabiliser layers in the AMSC tape. A brass sample holder (shown in Figure 5.8 (b)) was manufactured with an outer diameter of 31 mm and an inner square of 12.1 mm x 12.1 mm. The sample holder was cut by laser with four round gaps in the corners of the inner square and six gaps on the outer edges to achieve better heat dissipation.

(a)   *(b)*
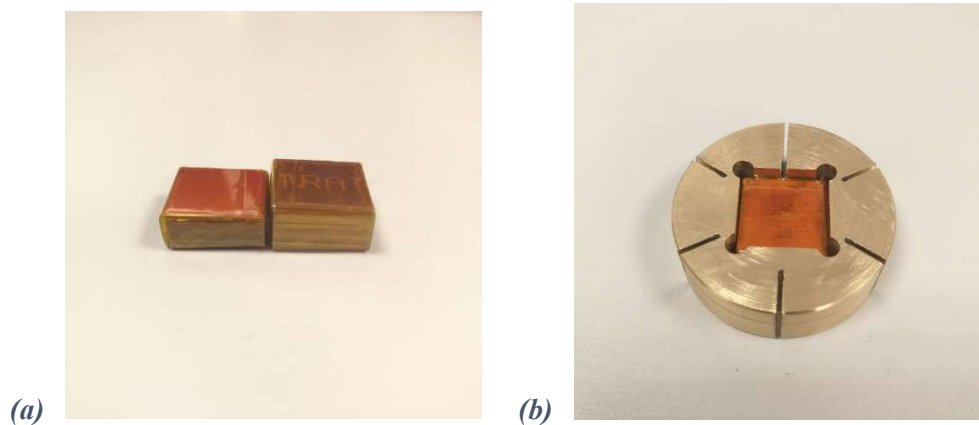
Figure 5.8: (a) 20-layer SuperPower stack (left) compared with a 20-layer AMSC stack (right). Both are coated with Kapton tapes. (b) Testing AMSC stack coated with Kapton tape in a cylinder sample holder made from brass.

5.4.2 Test rig and experimental process

The pulsed-field magnetisation experimental test rig used is in the Department of Engineering, University of Cambridge. The basic scheme is similar to the diagram shown in Figure 5.2. The only difference is the magnetised coil is a solenoid type. The discharged energy from the capacitor banks achieves up to 9 kJ [158]. The applied field has a rise time of approximately 25 ms. The trapped field was measured 0.8 mm (the height of a hall sensor) above an array of five hall sensors, as shown in Figure 5.9 (a). A thermal sensor was connected under the sample

111

stack to monitor the testing temperature. A heater was also installed under the sample holder for demagnetisation. The cooling system consisted of a cold head, vacuum equipment and a bath tank of liquid nitrogen.

(a)

(b)
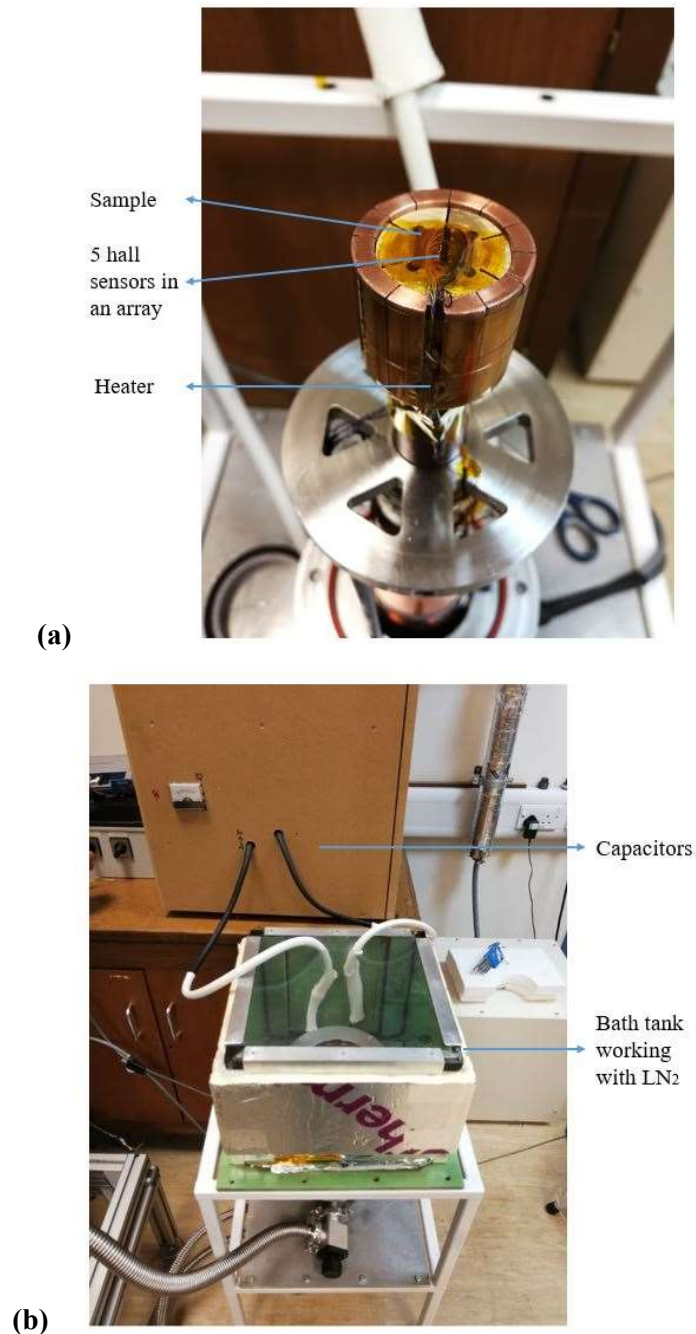
Figure 5.9: (a) 20-layer AMSC stack with the brass sample holder installed in the test rig and an array of five hall sensors stuck with Kapton tape above the stack. (b) Entire experimental test rig tested before cooling. The capacitor banks are in the brown box. The silver tube was connected with the cold head on the left-hand side.

The experimental process is similar to the single pulse one presented in Table 5.2, however, the working temperature was 30 K to 40 K for these tests. The time to cool down and warm up with the vacuum facilities took much longer than using liquid nitrogen. The applied voltages for the tests ranged from 30 V to 130 V, corresponding to a maximum applied external field ranging from 0.69 T to 2.99 T.

5.4.3 Results and analysis

5.4.3.1 Single-pulse magnetisation

A single pulse magnetisation was tested on the 20-layer AMSC stack at 40 K. The applied field ranged from 0.69 T to 1.61 T. The stack was fully magnetised when the magnitude of the applied field increased to approximately 1.15 T which resulted in a trapped field of 0.12 T, as shown in Figure 5.10 and Figure 5.12. After increasing the external field, the trapped field decreased dramatically, as the stack was over magnetised. The whole tendency is almost the same as the results presented in previous work [126]. Figure 5.12 and Figure 5.13 present the magnetic field penetration from the edge of the stack to the centre. Consequently, the trapped field value at the outer edge was higher than that of the centre during the rise of the pulse. The maximum trapped field was in the centre after magnetisation, which corresponds to the theory of Bean's model. Moreover, the noise from the measurement was more severe from the edge to the centre, so the trapped field in the centre was more stable.
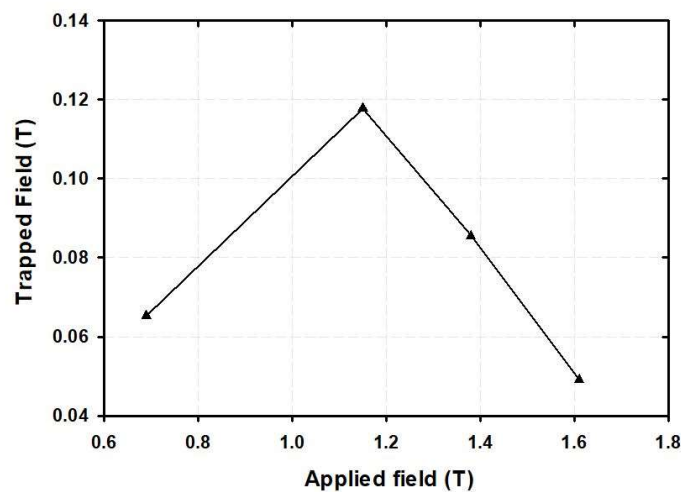
Figure 5.10: Measured trapped field in the centre of a 20-layer AMSC stack at 40 K with an applied single-pulse field ranging from 0.69 T to 1.61 T after 10 s.

The trapped field did not remain steady for several reasons. Firstly, according to the temperature upsurge in Figure 5.11, as the applied field increases, the produced temperature increased as well. After the ramp-up duration, the temperature decreased steadily for the under-magnetised status and steeply after full magnetisation. As mentioned in section 2.4.2.2, increasing temperature results in a decrease in the trapped field.

Compared with the results in section 5.3.3, the negative effect of the temperature rise on the trapped field value is more observable at lower temperatures. Secondly, during the single-pulse test, the stack was coated with Kapton tape, which is a thermal insulating film. The heat was not easily dissipated and therefore, the cool down process to 40 K always took several hours (although we always waited for at least 20 minutes after the monitored temperature reached 40 K). There is still the possibility that the working temperature for the entire testing stack might not be at 40 K precisely. Higher temperatures generally result in a lower trapper field value [144]. Furthermore, the middle sensor in the array of five sensors was not in the centre during the test according to the test results shown in Figure 5.13. There may be inaccuracy for the centre trapped field selected. Lastly, there is noise in the results, as Figure 5.12 shows, which may lead to offset and imprecise measurement results.
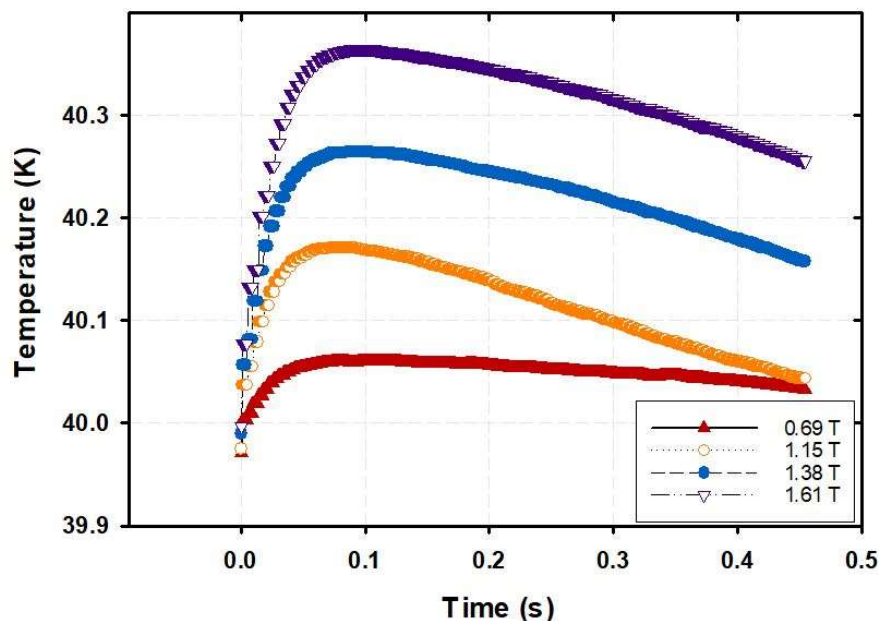
Figure 5.11: Temperature change of a 20-layer AMSC stack tested at 40K with an applied single-pulse field during a period of 0.5 s.
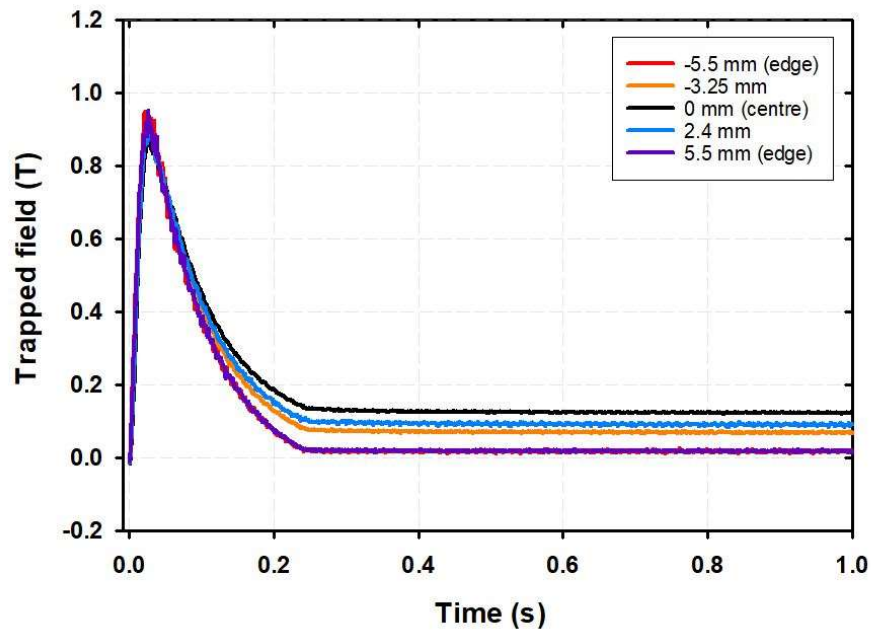
(a)
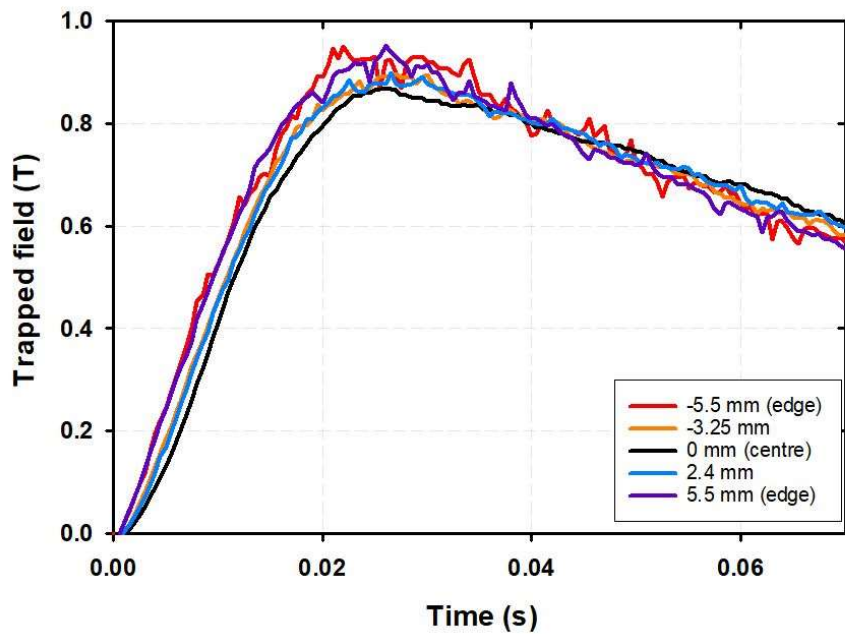
(b)

Figure 5.12: Trapped fields of a 20-layer AMSC stack with an applied field of 1.15 T measured during a time scale of (a) 1 s and (b) 0.07 s.
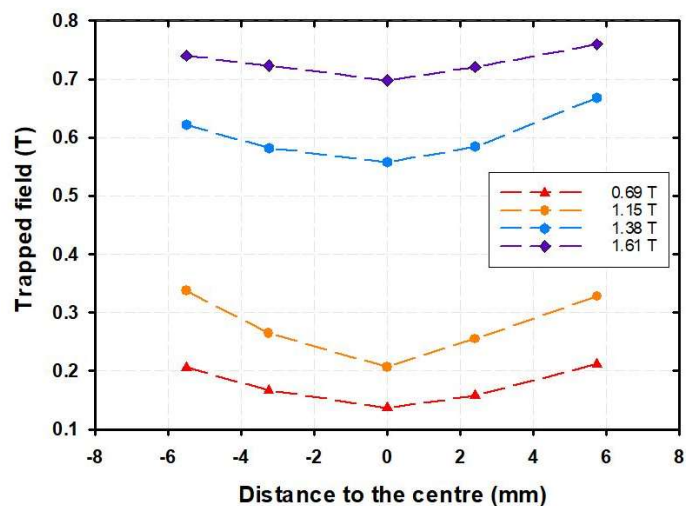
(a)
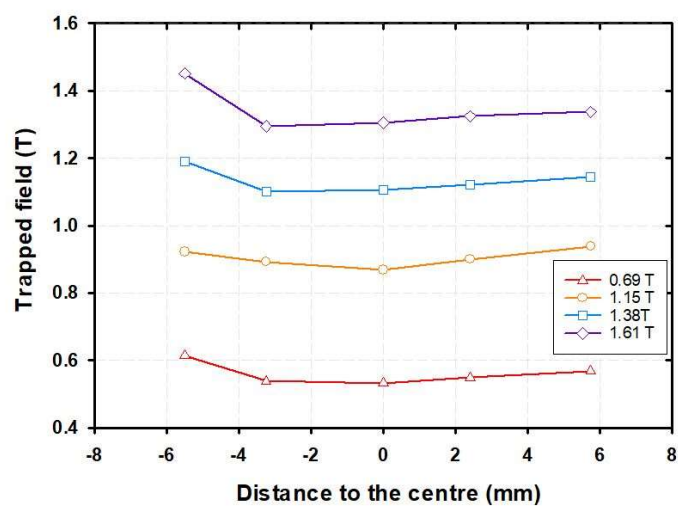
(b)
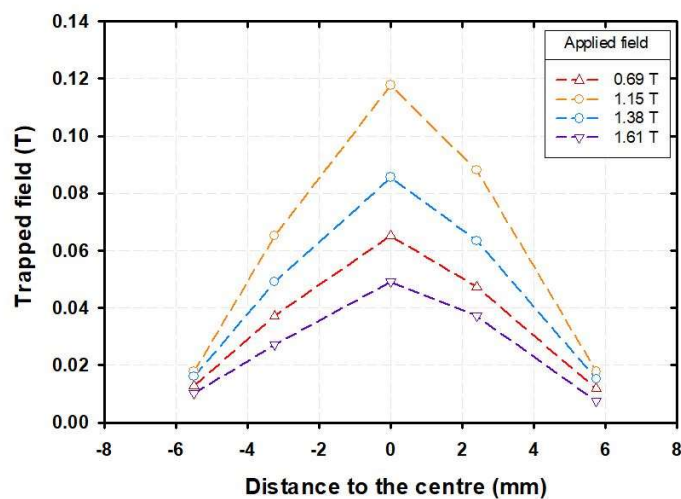
(c)

Figure 5.13: Trapped field profiles measured 0.8 mm above a 20-layer AMSC stack by an array of five sensors at (a) 0.005 s (during the rise time) (b) 0.025 s (pulse peak) and (c) 10 s (end of test).

116

5.4.3.2 Multi-pulse magnetisation

The multi-pulse magnetisations were tested at 30 K. Each trapped field was measured after 10 s. The next pulse was applied 30 s after the previous pulse. Incorporating the lessons from the single-pulse experiment, the Kapton tape was removed and the tapes were stacked with a bonding agent. In addition, the sample holder was also removed to ensure the temperature cooled down to 30 K more swiftly. The other processes were the same as the single-pulse test.

The applied pulses were iteratively magnetising pulsed field with reducing amplitude (IMRA) starting with 1.38 T and ending with 0.69 T. As Figure 5.14 presents, the trapped field increased with the first three pulses from 0.2335 T to 0.2408 T. After which the stack saturated and the trapped field reduced to 0.2407 T after the final pulse was applied. This result verified that the IMRA method is an effective way to enhance the trapped field of a HTS stack. On top of that, the trapped field increased significantly from 0.0858 T at 40 K to 0.2335 T at 30 K with an applied field of 1.38 T, which also indicated that the reduced temperature was able to increase the trapped field. The temperature cool-down and warm-up duration still took a long time. Regarding to previous experimental research, the trapped field of a 100-layer stack for pulse magnetization yielded to 1.56 T 0.8 mm above the surface of the stack and over 2 T estimated at the surface at 10 K using the MPSC technique [151]. As a result, the trapped field of the 20-layer AMSC stack was within our expectation.
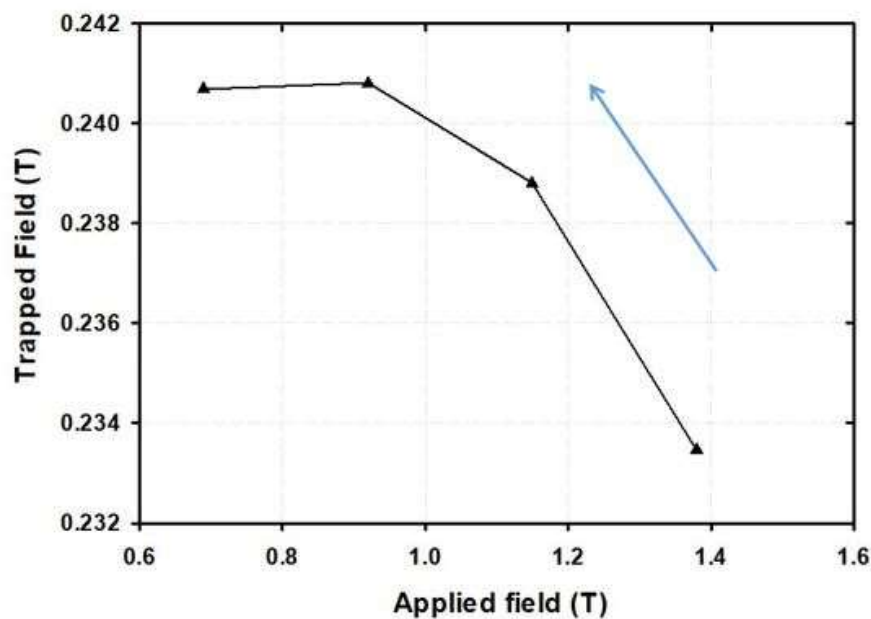
Figure 5.14: Measured trapped field of a 20-layer AMSC stack tested at 30 K with an applied multi-pulse field from 1.38 T to 0.69 T with declining intervals of 0.23 T.

5.5 Conclusion

In this chapter, experiments focused on the trapped field magnetisation of stacks. Two different types of tapes from different manufacturers were compared in section 5.2. One was the AMSC tape with a magnetic substrate and the other was the SuperPower tape without a magnetic substrate. The two 5-layer stacks made from the two tapes were compared for single pulse magnetisation at 77 K in section 5.3. The AMSC stack showed better performance on trapping field when the same pulse and external magnetic field was applied. Section 5.3.4 presented the single magnetisation pulse with equal and various ramp-down times, which were applied to the SuperPower stack. The results illustrated that the longer the ramp-down time the higher the trapped field. Furthermore, section 5.4 presented the results of single-pulse and multi-pulse magnetisation at a lower working temperature with different facilities, which were conducted on a 20-layer AMSC stack. There was a saturation point for the trapped field of the stack where the magnitude of the trapped field was the largest. Under or over that point the trapped field went down. The temperature increased with growing applied magnetic field, which was not beneficial to the trapped field and degraded the trapped field for over-magnetisation, which was more obvious at lower working temperatures. It is more stable to acquire higher trapped field results in the centre of the stack instead of the edge. Finally, the IMRA scheme has proved to be an effective way to increase the final trapped field. Overall, although the trapped field or size of the testing sample is not appropriate for using in a real HTS machine, the maximum trapped field of the AMSC stack for PFM was within our expectation. In terms of an electric machine design, more layers of stacks need to be tested with higher excited magnetic fields and more pulses can be applied to the stack.

To sum up, according to the findings of my research and previous research from other groups, an optimal HTS stack should have following features:

a) The substrates of the HTS tapes should better have magnetism. The magnetic substrate is able to enhance the total trapped fluxes when the stack is over magnetized and trapped more fields after the excitation process.

b) The thickness of the stacks could be thinner, which increase the engineering critical current density of the HTS stack, thus improving the trapped field.

c) Larger resistivity of metallic stabilizers of HTS tapes may be more suitable for application in TFMs to reduce the heat generation.

d) Compared to rectangular stacks, square stacks might trap more field even with smaller size.

e) The larger the widths of the stack, the better the final trapped fields.

f) The height or layers of the stacks could approach the width or diameter of the stacked tapes.

g) To achieve more uniform trapped fields, the overlapped angled stacks with FM plate underneath might be an excellent choice.

Chapter 6   AC loss mitigation

To fulfil the requirements for fully HTS rotating machines, the armature windings can be replaced with HTS coils. However, when an alternating current (AC) or an AC electromagnetic field is applied, the HTS coils produce some electromagnetic energy losses, which are referred to as AC loss. AC loss is one of the obstacles in the development of HTS rotating machines, which needs to be minimised. This chapter, therefore, investigates and discusses the reduction of AC loss with a multi-filament superconductor. The AC loss reduction methods are investigated by experimental and simulated approaches.

6.1 Overview of AC losses of multi-filament superconductors

The striation process is a very effective way to reduce the hysteresis loss within a superconductor. There are various techniques to achieve striation: laser scribing (used the most), chemical etching, mechanical scratching of the buffer layers, lift-off process with a photoresist mask technique, dry etching, inkjet printing or the combination of laser scribing and chemical etching [159]. Characteristics of magnetisation and transport AC losses of multi-filament tapes or coils have been previously discussed and presented in the literature and will be briefly summarised below.

As mentioned in Section 2.5, magnetisation and transport losses are two of the main issues that need to be further investigated for multi-filament superconductors. A great number of research groups, as well as manufacturers have focused on investigating the magnetisation AC losses and transverse resistivity of striated tapes [159-173]. It has been confirmed that striation is an effective way to reduce hysteretic AC losses. However, the coupling loss becomes important when the number of filaments is increased. Furthermore, the effects of inhomogeneity on the current carrying capability increases with decreasing filament width [166].

The total magnetisation loss in a sub-divided tape is the sum of the losses dissipated in an individual filament [159-168]. The superconductor can experience full filament uncoupling to full coupling within a specific frequency range [159]. However, the striation process lowers the critical current densities of individual filaments, as well as the n-value, and striated tapes are vulnerable to localised defects [159, 161, 162], which can impede the flow of current through a filament. Therefore, uniformity of the properties of individual filaments is extremely important [174]. This issue can be overcome either by covering the filaments with a thick normal metal layer of low resistivity or by building a network of superconducting bridges in such a way that allows current sharing between the filaments [161]. The latter method has been investigated by M. Majoros et $al.$ who compared non-striated and striated RABiTS (Rolling Assisted Biaxially Textured Substrates) coated conductors with different kinds of well-defined inter-filament bridging (designed to aid current sharing between filaments), unbridged filaments and a monolayer. Conclusions were drawn that striated samples with no filament bridges had the lowest AC losses, which was about a factor of two lower compared with the losses in the non-striated samples. Nevertheless, the AC losses of the samples with multiple bridges were higher than the losses of the samples with unbridged filaments or with only one or two bridges, which was due to significant filament coupling [160].

The decrease of magnetisation losses in striated tapes (with N filaments) exhibits an approximately 1/N characteristic [162]. Research on transverse resistance has been conducted to understand how the coupling currents flow inside the coated conductor. Furthermore, a conclusion has been proposed that the coupling current prevalently flows in the metallic substrate rather than in and out of the filaments [159, 168]. There are several approaches to reducing the coupling loss such as oxidising the samples so that the barrier/interface resistance between the filaments and substrate is significantly increased [159, 164], or using a conductor on a round core (CORC) due to the short twist pitch of the CORC cable, etc. [168].

Although lots of results have been gained from straight tape 'in-field' scenarios, the transport AC loss of YBCO CC coils is an aspect that cannot be ignored with applied current. M. Majoros et $al.$ gave further explanations on the screening current coupled in both the striated and monolayer samples [175]. They compared the transport AC loss between striated and non-striated YBCO CC tapes and concluded that the frequency dependence for the transport loss is rather weak and mainly determined by the losses in the substrate and Ni layers, up to currents of approximately 50% of the critical current [175]. A magnetic screening method has been

suggested as a possible way to decouple the filaments electromagnetically in order to reduce the transport AC loss [176].

The transport AC loss of multi-filamentary YBCO coils, however, have not been investigated both experimentally and in simulations. Therefore, the properties of the transport AC losses of striated and non-striated coils was investigated using both experimental and finite element methods of an axial symmetrical model combining the methods presented by Z. Hong in [54] and M. Zhang in [55].

In this chapter, the measurements of critical current, as well as the AC transport losses of two coils wound using multi-filamentary YBCO CC and normal non-striated YBCO CC (manufactured by SuperPower) are present in Section 6.2. The width and thickness of both of the tapes is the same. Experimental results are also compared with simulated results. The results presented in Sections 6.2 and 6.3 have been previously published in [177].

6.2 Experiment results of the AC loss comparison between multifilament and non-striated YBCO coils

6.2.1 Sample preparation

Two sample coils wound by me using YBCO CCs were built, as shown in Figure 6.1. The current contacts were made by copper and soldered with tapes. They were drilled with holes and nailed with G10 sample holders. The connecting yellow wires were soldered with the superconducting tapes and connected with NI SCXI card to collect measuring results.

Figure 6.1 Multi-filament sample coil (left) and non-striated sample coil (right) wounded by YBCO coated conductors supplied by the SuperPower.

The tapes used were supplied by SuperPower. The width and the length of the two (striated and non-striated) tapes were identical with a width and length of 4 mm and 2.76 m, respectively. The tapes consisted of a 50 μm Hastelloy substrate and a 2 μm silver protective layer. The coils were insulated by Kapton tapes for each layer.

The commercial multi-filament tape used has four filaments with a 0.03 mm gap per filament. The measurements were taken using two G10 sample holders, which have an outer and inner diameter of 8.9 cm and 7 cm, respectively. Both coils are wound with 9.5 turns. Further details of the coils are provided in Table 6.1.

Table 6.1: Tape configurations for striated and non-striated coils

	Striated coil	Non-striated coil
Wire Type	SCS4050-AP	SCS4050-AP-i
Tape width (mm)	4	4
Total tape length (m)	2.76	2.76
Number of filaments	4	-
Filament width(mm)	0.978	-
Tape I_c (A)	90	103
Number of Turns	9.5	9.5
Coil radius (mm)	44.5	44.5
Frequency range (Hz)	70-300	70-300
Coil I_c (A)	66	71

6.2.2 Test rig and experiment process

The experimental method used was the electrical method [178]. The test rig was based on the four-probe method, which has been previously established and explained by J. Zhu [179]. The schematic diagram for testing the critical current and the AC losses is presented in Figure 6.2 and Figure 6.3, respectively. Furthermore, the measurement system panel in LabVIEW is shown in Figure 6.4.

A sinusoidal signal waveform was supplied by a 20-kW power amplifier, which was connected to a transformer. A Rogowski coil was used to measure the applied current from the secondary side of the transformer. To get a pure resistive voltage, a cancellation coil was connected in series with the measured superconducting coil and the secondary side of the transformer, to cancel the inductive voltage produced due to a time varying applied transport current.

The source voltage of the testing coil can be expressed by:

$$V_s = RI + j\omega LI \qquad (6.1)$$

where the inductive part of the voltage ($j\omega LI$) should be canceled by adjusting the mutual inductance of the secondary side of the compensation coil. The voltage of the secondary coil is $V_c = j\omega MI$. As long as M equals to L, the pure resistive loss voltage V_{rms} shown in Figure 6.3 is acquired:

$$V_{rms} = V_s - V_c = RI + j\omega(L - M)I = RI \tag{6.2}$$

The self-field AC transport loss of the superconducting coil per unit length per cycle can be calculated by:

$$Q = \frac{V_{rms}I_{rms}}{fl} \tag{6.3}$$

where V_{rms} and I_{rms} are the RMS values of pure resistive loss voltage and the in-phase AC transport current of the superconductor between two voltage taps, respectively; f is the frequency; and, l is the length between the two voltage taps.
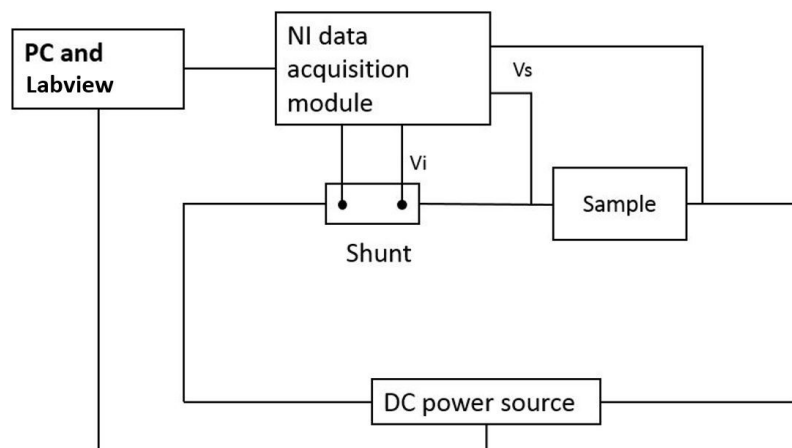
Figure 6.2 Schematic diagram for measuring the critical current.
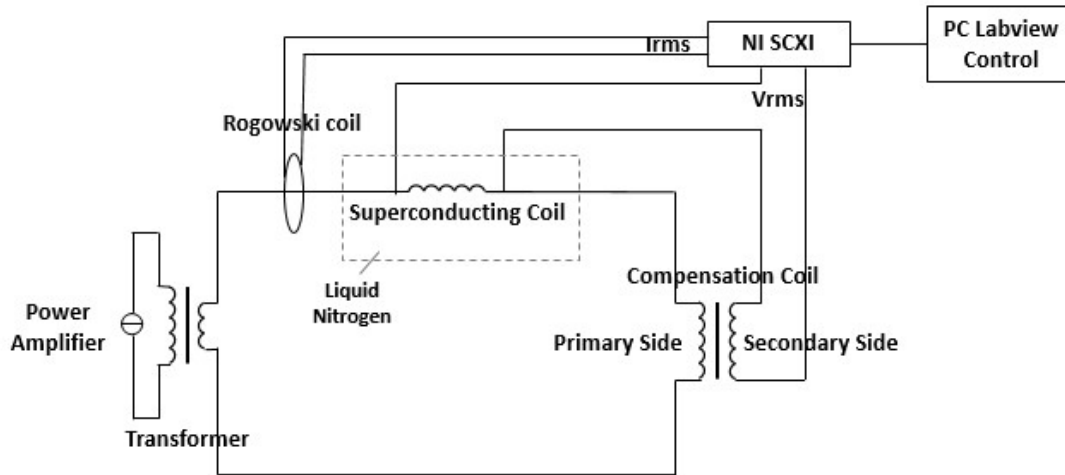
Figure 6.3 Schematic diagram for measuring the transport AC loss.
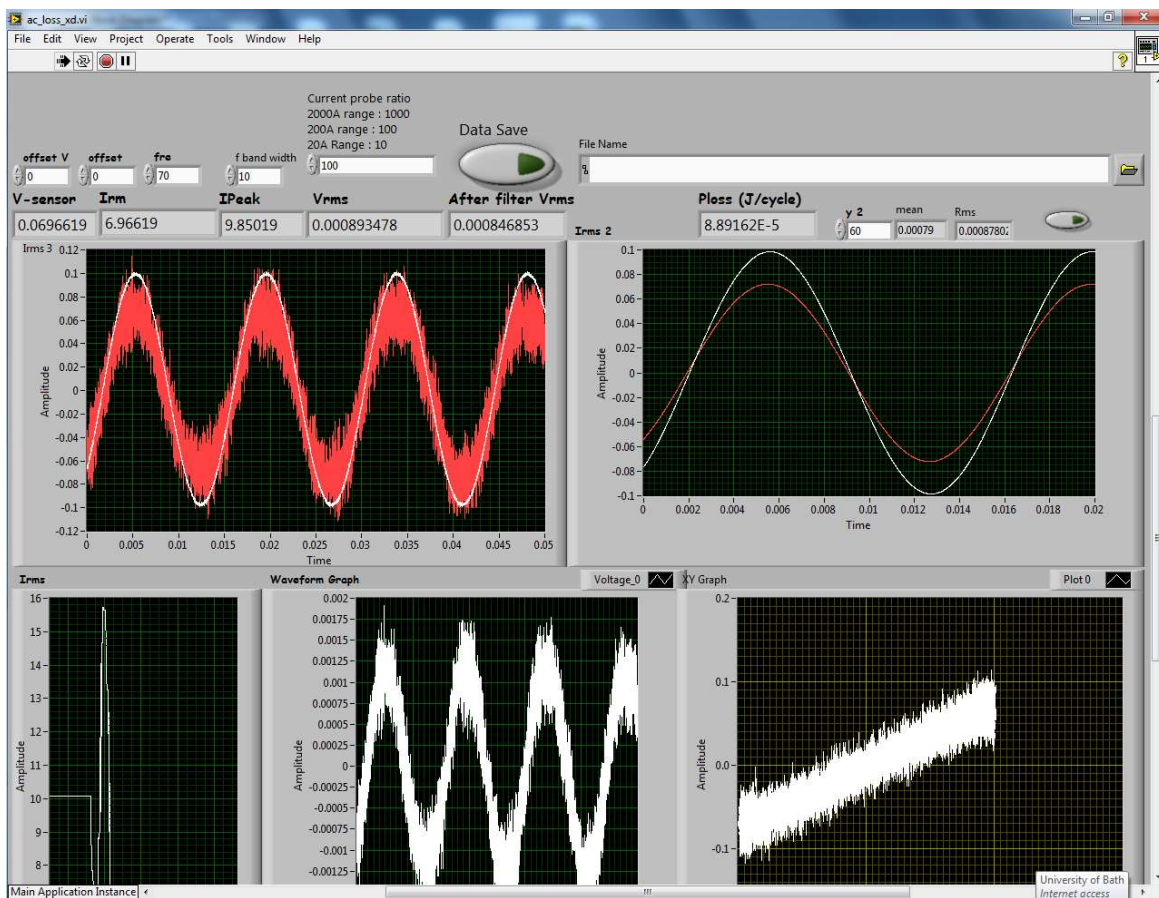
Figure 6.4 Measurement system panel in LabVIEW.

6.2.3 Critical current measurement

Figure 6.5 presents the results for the DC current and voltage characteristics of the striated and non-striated coils. The results were processed in MATLAB to cancel the noise from measurement and produce smoother graphs. The coil with no strips had the higher critical current, which was approximately 71 A. Due to the removal of some superconducting material, the critical current of the multi-filament coil was approximately 66 A, which is about a 7% degradation compared with the non-striated coil. In regard to the filament width, the cut groove is relatively thin (0.03 mm), whereas the critical current still decreases a lot for a 9.5-turn coil. The *n* values were calculated using MATLAB, which were 18 and 24 for the multi-filamentary and non-striated coils, respectively. The results indicate that the striation process lowers the critical current densities of individual filaments, as well as the *n*-value [162].
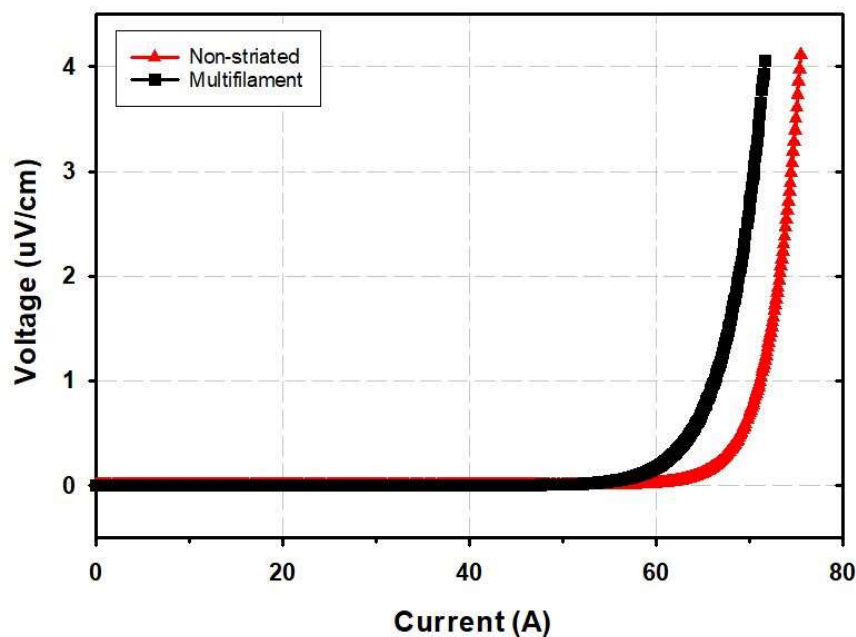
Figure 6.5 Critical currents of the multi-filament and non-striated coils after being processed in MATLAB.

6.2.4 AC loss measurement

The experimental measurement results of the transport AC losses for the multi-filament and non-striated coils are presented in Figure 6.6. Both coils were applied with the same current and in the same frequency range of 70 Hz to 300 Hz. The current range for all the tests was from 10 A to 50 A. The RMS current could not exceed 50 A due to the upper limits of the internal oscillator output of the power amplifier used in the lab during the experiments. Compared to the non-striated coil, the characteristics of independent frequency of the multi-filament coil is slightly better at the lower frequency range.

For comparison, only two sets of results were used (120 Hz and 220 Hz) for better observation. With the same applied current, there was no noticeable difference between the multi-filamentary and non-striated coils in the experimental results presented in Figure 6.7 (a). However, the transport AC loss of the multi-filamentary coil was slightly lower than the non-striated coil.

According to the results presented in [159, 162, 164-166, 168], a larger thickness of grooves or an increased number of filaments for the same width of tape leads to lower AC losses. The groove of the multi-filamentary tape used in the experiments was only 0.03 mm thick, which is relatively thin. Moreover, there were only four filaments in the tape. Furthermore, the current applied to the coils was not large and hence, the reduction of the transport AC loss for the multi-filamentary coil was not much lower than the non-striated coil. Furthermore, the coupling loss originating from the metallic connections among the filaments could increase the total AC losses in the multi-filament coils [159, 169].

The contribution of the eddy current losses generated in the Hastelloy substrate cannot be neglected either [170]. Aside from sacrificing mechanical stability by reducing the thickness, the eddy currents cannot be reduced. The comparison results of the transport AC losses plotted against the normalised current (divided by I_c) are shown in Figure 6.7 (b). It is more obvious to see the difference between the two measured coils. To get the same normalised current, more current flows in the non-striated coil, which gives rise to a larger transport AC loss. The reduction in the multi-filamentary coil is approximately 25% for the same normalised current, which is an excellent feature.

(a)

(b)
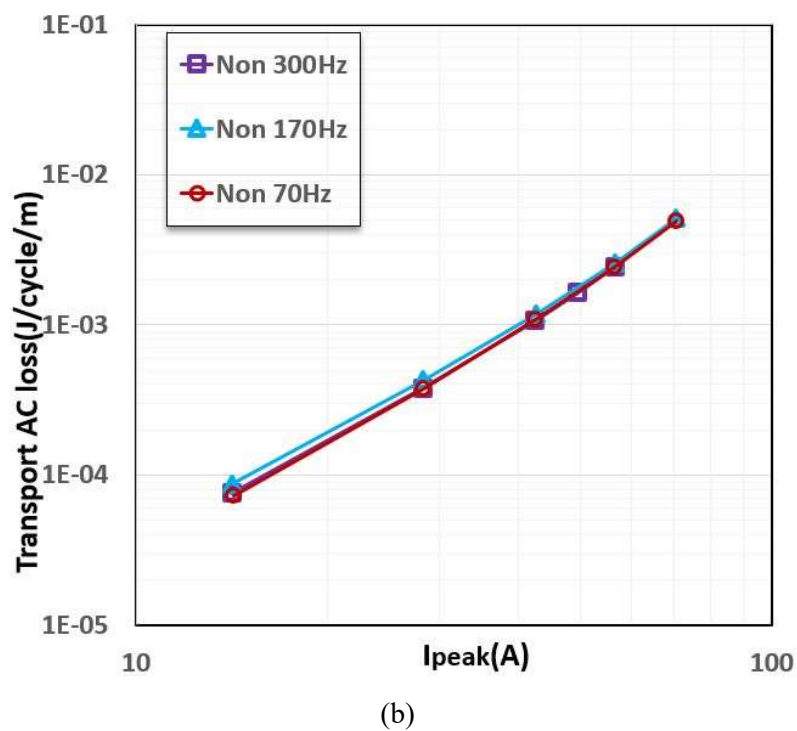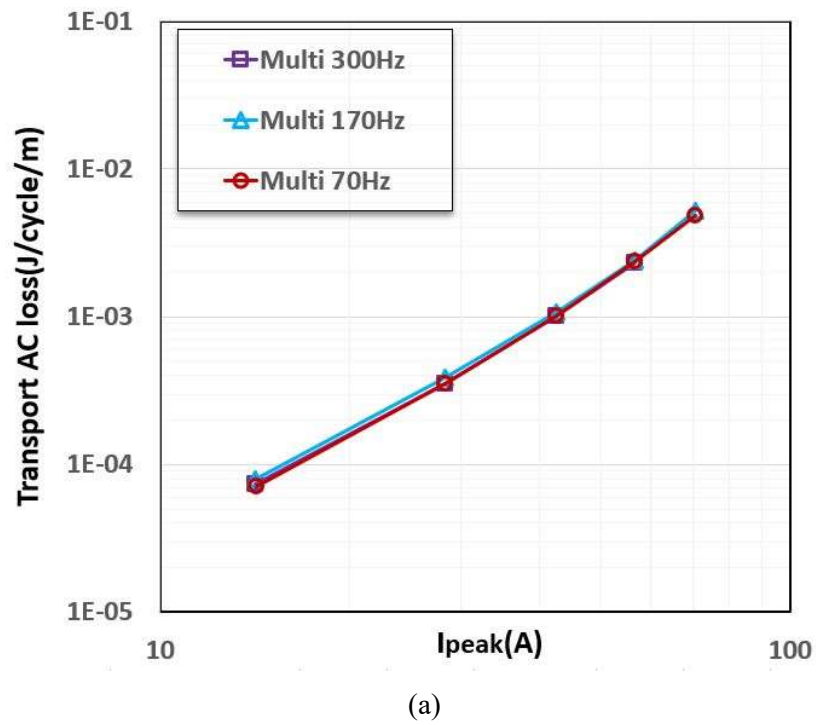
Figure 6.6 Transport AC loss of (a) multi-filament and (b) non-striated coils with various applied currents measured in the frequency range of 70 Hz to 300 Hz.
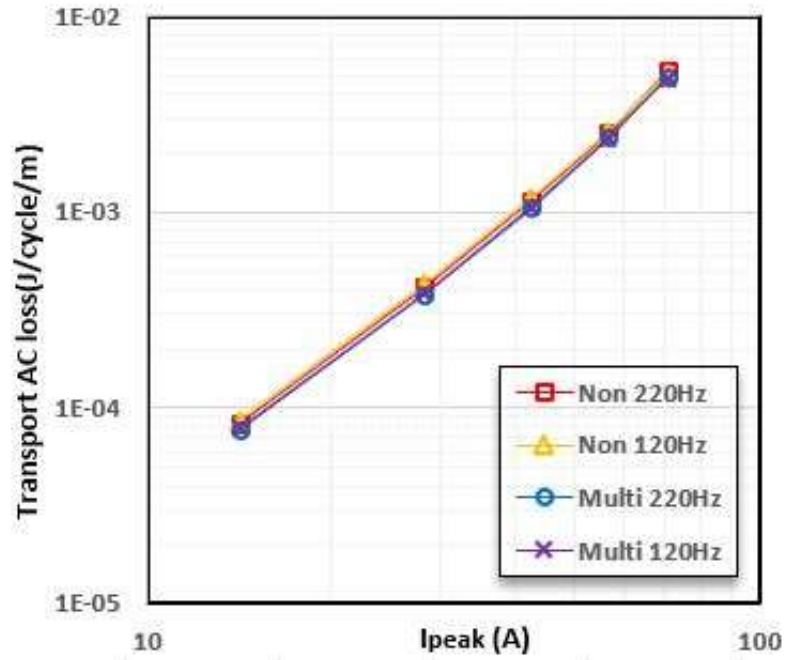
(a)
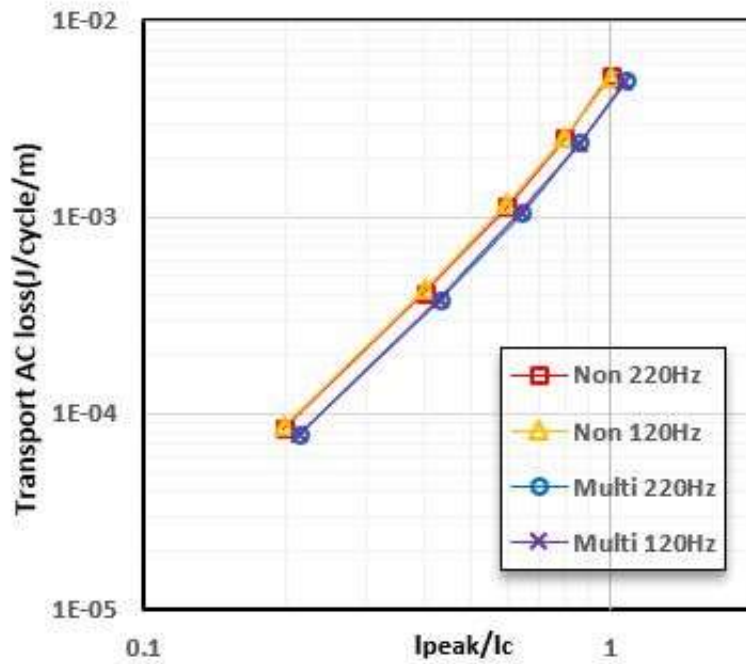
(b)

Figure 6.7 Comparison of the transport AC loss with (a) applied current and (b) normalised current of the multi-filamentary and non-striated coils derived from experiments in the frequency range of 120 Hz to 220 Hz.

6.3 Simulation results of AC loss comparison

6.3.1 Geometry, parameters and mesh

Figure 6.8 presents the cross-sections of the 2D cylindrical-axial axisymmetric models of the multi-filament and non-striated coils built in COMSOL. The models were simulated using the *H*-formulation analysis method. The detailed formulations used in the models are listed in Section 2.3.2.1 Table 3.1.

Table 6.2: Governing equations of 2D cylindrical-axial models using H-formulation

Cartesian model

Faraday's law	$\begin{bmatrix} -\dfrac{\partial E_\theta}{\partial z} \\ \dfrac{1}{r}\dfrac{\partial(rE_\theta)}{\partial r} \end{bmatrix} = -\mu_0\mu_r \begin{bmatrix} \dfrac{dH_r}{dt} \\ \dfrac{dH_z}{dt} \end{bmatrix}$
Ampere's law	$J_\theta = \dfrac{\partial H_r}{\partial z} - \dfrac{\partial H_z}{\partial r}$
E-J power law	$E_\theta = E_0 \left(\dfrac{J_\theta}{J_c}\right)^n$
Partial differential equation (PDE)	$\begin{bmatrix} -\dfrac{\partial\left(E_0\left(\dfrac{\frac{\partial H_r}{\partial z}-\frac{\partial H_z}{\partial r}}{J_c}\right)^n\right)}{\partial z} \\ \dfrac{\partial\left(E_0\left(\dfrac{\frac{\partial H_r}{\partial z}-\frac{\partial H_z}{\partial r}}{J_c}\right)^n\right)}{\partial r} \end{bmatrix} = -\mu \begin{bmatrix} \dfrac{dH_r}{dt} \\ \dfrac{dH_z}{dt} \end{bmatrix}$
Dirichlet boundary condition	$\begin{cases} H_r = F_r(t) \\ H_z = F_z(t) \end{cases}$

The equation used to define the relationship between the current density and magnetic field is:

$$J_c(B_\perp, B_\parallel) = J_{c0}(T)\left(1 + \frac{\sqrt{B_r^2 + k_0^2 B_z^2}}{B_0}\right)^{-\beta}$$

(6.4)

where B_r and B_z are the magnetic field perpendicular and parallel to the z-axis of the coil cross-section, respectively.

The values of the parameters used to model the coils are listed in Table 6.3. Most of the parameters correspond to the real coils. However, it not easy to simulate half a turn of a coil. Therefore, the turns computed in the models was 10.

The equation to calculate the transport AC loss Q (J/cycle) in the simulation work [180] is:

$$Q = \int_t \left[\sum_1^N 2\pi r \int_S E_\theta \cdot J_\theta \, dS\right] dt$$

(6.5)

where S is the cross-section of a single turn, and N denotes the total turns; E_θ and J_θ are the magnetic field and current density of the θ-axis, respectively; and, r is the radius of the Nth turn.
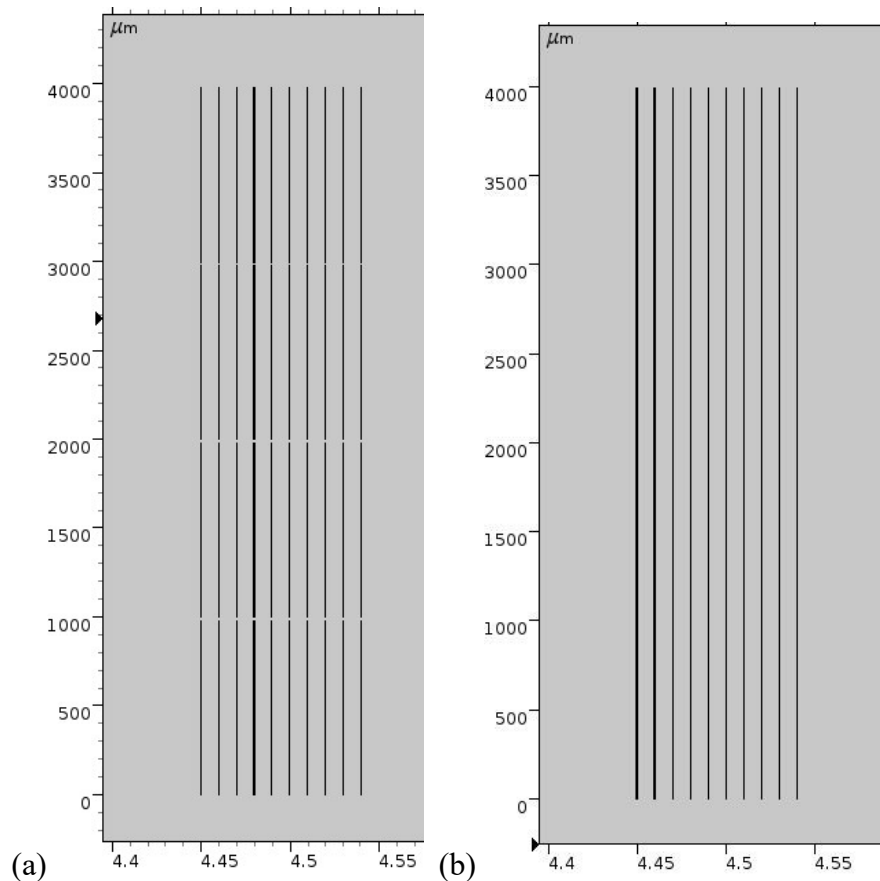
Figure 6.8 Cross-section of the 2D axial symmetrical model of (a) multi-filament coil and (b) non-striated coil with 10 turns each. The units for each axis are *μm*.

Table 6.3: Coils configuration description and values of parameters used in the modelling

Parameter	Description	Multi-filament	Non-striated
μ_0	Vacuum permeability	$4\pi\times10^{-7}$ H/m	$4\pi\times10^{-7}$ H/m
n	n-value in E-J power law	18	24
E_0	Electric field constant in E-J power law	1 μV/cm	1 μV/cm
I_c	Critical current of the tape	90 A	103 A
f	Frequency	70-300Hz	70-300Hz
k	Anisotropy parameter	1.1	1.1
B_0	Parameters to determine the rapidity of the J_c reduction with the magnetic field	0.07168	0.07168
β	Parameters to determine the rapidity of the J_c reduction with the magnetic field	0.7	0.7
N	Number of turns	10	10
r	Coil inner radius	44.5mm	44.5mm

In the models, appropriate settings for the boundary conditions are essential. Therefore, Dirichlet boundary conditions were applied to the boundaries of the superconductor and a square boundary selected for the air sub-domain. A pointwise constraint was utilised to apply the transport current. The width of the non-striated coil was divided into 80 elements. Since there were four filaments in the striated tape, each filament was divided into 20 elements. The mapped square elements were also converted to triangle elements. The air domain was at least 100 times larger than sample domain and was meshed with free triangular elements. The mesh contained 10614 domain elements and 1736 boundary elements for the striated coil, and 9924 domain elements and 1676 boundary elements for the non-striated coil, respectively.

6.3.2 Critical current modelling results

Figure 6.9 shows the simulation results for the models applied with continued DC current. The critical current results for the multi-filament and non-striated coils were 70 A and 73 A, respectively. The simulation results are higher than the experimental results. The main reason for this is the coil turns. In the manufactured coils, the turns of both coils are 9.5, which is less than the turns used in the simulation (10 turns). Also, the critical current of the tape might have degraded due to oxidisation. However, 90 A and 103 A were adopted for the critical currents of the two tapes in the models for the multi-filament and non-striated coils, respectively, which may have led to higher critical currents for the coils.
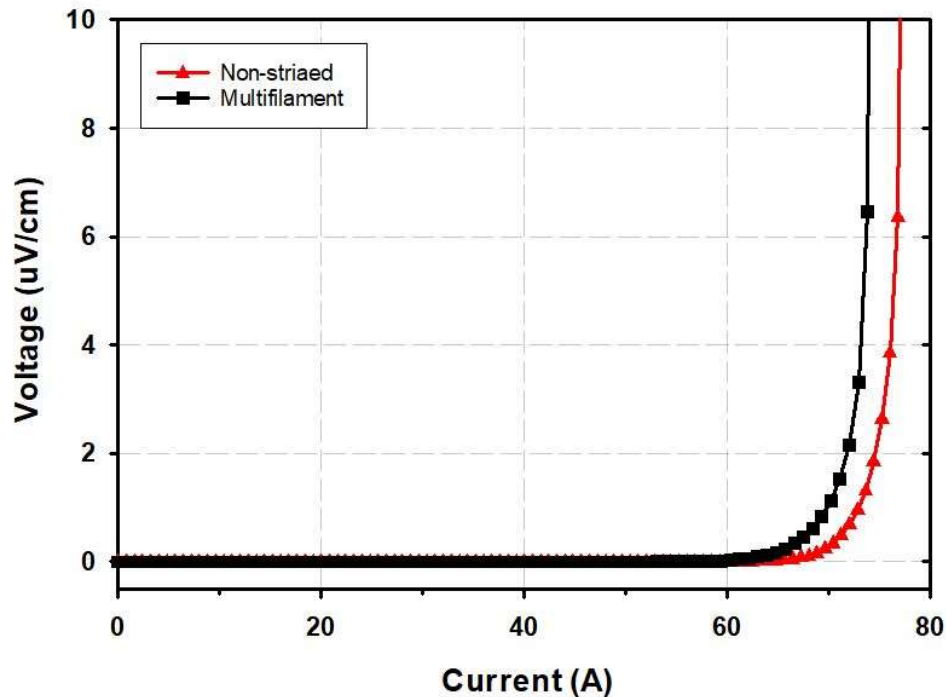
Figure 6.9 Simulation results of the critical current of the multi-filament and the non-striated coils.

6.3.3 AC loss modelling results

In Figure 6.10, the simulated results are compared at a frequency of 170 Hz. To compare the simulation results with the measured results, the transport AC loss Q is divided by the total length of the coils. As can be seen in Figure 6.10, the multi-filamentary coil has the lower transport AC loss (the same normalised current was applied to both coils). The lessening of the transport AC loss can reach to 25%. Compared with the experimental results, the simulation results illustrate a better transport AC loss reduction. For both coils, the simulated results are lower than the experimental results. The main reason for this is the fact that the metallic part in the substrate or stabiliser of the coated conductor was ignored in the simulations. Therefore, the eddy current loss and coupling loss generated within the metallic parts were ignored as well. In other words, the coupling losses and eddy current losses are essential to be included and investigated in simulations.
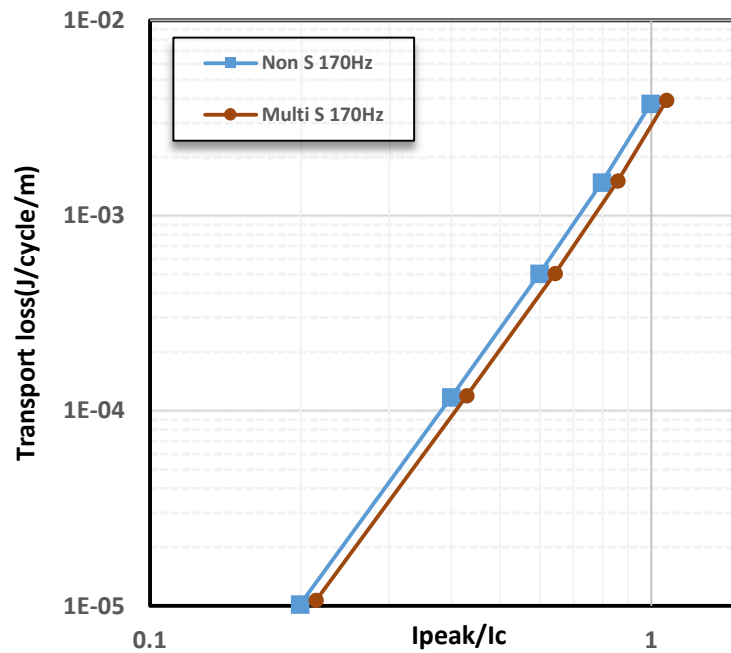
Figure 6.10 Comparison of the transport AC loss with normalised current of the multi-filamentary and non-striated coils derived from simulation at 170 Hz.

6.4 Conclusion

AC losses are one of the vital issues for not only HTS rotating machine design but also other in-situ applications. Although many researchers have focused on this topic and accelerated the progress of the industry, further investigation is still required, especially, with regards to AC losses mitigation.

One effective method of lessening the AC losses was investigated in this chapter, which was the striation approach. In section 6.1, previous work on AC transport and magnetisation losses was briefly summarised and concluded. A multi-filament coil was wound and compared with a normal non-striated coil, to study the effects of the striation process on the transport AC losses. Section 6.2 introduced the experimental results for two coils, where the critical current and transporting AC losses were compared. 2D axial symmetrical models of a multi-filament coil and a non-striated coil were built in COMSOL and investigated using the finite element method with *H*-formulation analysis in section 6.3. Furthermore, the critical current and AC losses were also compared. Both methodologies confirmed that striating HTS tape into multi-filaments can reduce the transport AC loss of coils effectively.

Chapter 7 Conclusion

7.1 Thesis summary

This thesis presented a study of PFM of HTS stacks and the reduction of AC losses by means of simulation and experimental methods. Two technical issues were addressed: how the magnetisation of HTS stacks by PFM is achieved, and how the current carrying capacity and impact of AC losses on HTS windings are affected. The first issue determines the performance of TFM for permanent magnets in HTS machine rotor designs. The second issue relates to HTS machine stator designs and the cryogenic design, as well as the system efficiency.

Numerical FEM implementations according to Maxwell's equations were introduced in Chapter 3. An exhaustive description of the 2D thermal-coupled *H*-formulation model for a HTS stack with Cartesian coordinates was presented in section 3.1. The structure of the stacks based on commercial AMSC (with magnetic substrate) and SuperPower (without magnetic substrate) tapes were simulated with actual thicknesses and materials in each layer. The layouts and detailed governing equations, based on Faraday's Law, Ampere's law and the E-J power law, and corresponding boundary conditions of the *H*-formulation and *T-A* formulation models of the HTS stacks, were described in sections 3.1.1 and 3.2. As the most important part in the PFM simulations, the thermal-coupled modelling was also discussed in section 3.1.2. The proposed 2D *H*-formulation model was validated by experimental work and presented in section 3.1.3.

To confirm the proposed thin line approximation method (*T-A* formulation) model, the ZFC results using both the *H*-formulation and *T-A* formulation models were compared in section 3.3. The results matched excellently for the SuperPower stack. In sections 3.4 and 3.5, the *T-A* formulation with updated thermal model was proposed and compared with the validated *H*-formulation model. The simulation time was dramatically reduced with the *T-A* formulation model compared with the *H*-formulation model. However, the distribution and final trapped

field results between the *T-A* formulation model and *H*-formulation were not matched perfectly for laminated-structure model. The *T-A* formulation model could be an efficient time-saving tool to solve the problems with the superconducting layer involved and qualitative simulation for PFM of HTS stacks. However, further investigation for the thermal-coupled *T-A* formulation model is still required. These methodologies were the basis for the simulations and numerical work presented in this thesis.

Chapter 4 presented the simulation results about the PFM of HTS stacks. In order to understand the relationship between the simulated parameters, the temperature and trapped fields of stacks (stacks with and without magnetic substrates) were compared with a different exponent parameter n value in the E-J power law and the flux density constant B_0 parameter in the Kim model. Results illustrated a large variation of trapped field and temperature variation with different simulated parameters selected. Furthermore, the magnetic properties of the substrate layers were analysed for two different stacks with the same structures of stabilisers in section 4.2.1. The stacks simulated with a magnetic substrate could trap more magnetic flux from the centre to the edge. In addition, the thicknesses of different substrates were also studied in section 4.2.2. The results showed that the impact of substrate thickness is not as obvious as the high magnetism of a substrate layer. This indicated a way to select the most appropriate tape used for HTS TFM, to achieve higher trapped field.

In Chapter 5, the PFM of HTS stacks was investigated by experimental work. Two 5-layer stacks (with and without a magnetic substrate) were magnetised by vortex-type copper coils using PFM at 77 K. The experimental results presented in section 5.3.3 confirmed the assumption that magnetic substrates can enhance the trapped field with an applied external magnetic field. Moreover, a test with different pulse durations was conducted and presented in section 5.3.4. Results showed that the trapped field was strengthened when the pulsed field with a longer ramp-down time was applied. To determine the influence of temperature and the distribution of magnetic fields, the HTS stack was magnetised by a single pulse and also multi pulses at lower working temperatures in section 5.4. It was more apparent that the detriment of temperature is inevitable at lower temperatures and the trapped field of HTS stacks can be maximised by applying iteratively magnetising pulsed fields with reducing amplitude. The suggestion for building optimal HTS stacks was proposed at the end of this chapter.

Chapter 6 presented an investigation into the mitigation of AC losses. A multi-filament coil was wound and compared with a normal non-striated coil, to study the effects of the striation

process on the transport AC loss, which was presented in section 6.2. Critical currents and the transport AC loss were measured using a four-point method and a compensation method. The multi-filament coils reduced the AC transport loss but resulted in a lower current carrying capacity. In section 6.3, 2D axisymmetric al models of a multi-filament coil and a non-striated coil were built in COMSOL and investigated using FEM with *H*-formulation analysis. It was found that the critical current of the simulated results for the 10-turns coil was higher than that of the experimental results with a 9.5-turns coil. The same conclusion was addressed for the transport AC losses estimation compared to the experiment. The reduction of the transport AC loss of multi-filament coil can reach to 25%. It was determined that a multi-filament coil is an appropriate way to reduce the transport AC loss and increase the efficiency.

7.2 Future work

Although most of the targets were achieved during this PhD research project, there remain challenges that require further investigation. Therefore, continuing from the contributions of this thesis, further work can be stated as:

- ➢ Modelling techniques:
  1. The proposed thermal-coupled *T-A* formulation model needs further investigation on the effects of laminated structure on the trapped field results to remove the discrepancy between the temperature involved *H*-formulation model and the *T-A* formulation model.
  2. For the simulations, the simulation results can be more accurate when more experimental data is included such as the relationship between the critical current, and the magnitude and angle of the magnetic fields.
  3. The temperature boundary conditions and temperature cooling system in the simulations needs to be improved. The influence of temperature and the corresponding thermal-effect parameters on the PFM of HTS stacks needs to be investigated, since this research only focused on temperatures of 30 K and 77 K. Furthermore, the effects of the tape layers on the trapped fields of the HTS stacks (with and without magnetic substrates) should be studied. With different thicknesses of HTS stacks, the performance of TFM will vary.

4. Multi-pulse field magnetisation can be further investigated for stacks with magnetic substrate at various temperature.

➢ Experimental techniques:

1. The temperature monitoring system and the cooling system for lower temperature testing used in the PFM experiments could be improved to be more sensitive and accurate. The capacities of the capacitors used to provide the energy for the PFM circuit could be enlarged, to potentially achieve a higher exciting magnetic field. Furthermore, stacks with and without magnetic substrates can be compared with the same stabilisers. The thickness of stacks and different working temperatures can also be taken into consideration and investigated.

2. A striated Roebel cable can be investigated for potential use as a HTS winding in an electric machine, since a Roebel cable is able to achieve large current density and striation can reduce the AC losses. A group has presently been working on the AC losses of the striated Roebel cable [121, 181]. However, whether it is suitable for use as a HTS winding in an electric machine has not, as yet, been determined.

3. The results achieved in this research are theoretical. Therefore, in terms of practical applications, HTS stacks and windings need to be further analysed for the application in an electric machine. In terms of the HTS stacks, more layers of stacks should be tested as field poles in HTS machines. The magnetic fields and potential trapped fields for HTS stacks at different angels need to be tested. As for HTS windings, more turns of striated coils need to be investigated at a lower temperature. It is also essential for HTS machines to find a suitable working temperature to maximise the benefits of fully HTS machines.

Reference

[1]   B. A. Glowacki, "Superconductivity and Superconductors," in *Kirk-Othmer Encyclopedia of Chemical Technology*: John Wiley & Sons, Inc., 2000.

[2]   F. London and H. London, "The Electromagnetic Equations of the Supraconductor," *Proceedings of the Royal Society of London. Series A, Mathematical and Physical Sciences (1934-1990),* vol. 149, no. 866, pp. 71-88, 1935, doi: 10.1098/rspa.1935.0048.

[3]   Y. Wang, *Fundamental elements of applied superconductivity in electrical engineering*. John Wiley & Sons, 2013.

[4]   V. L. G. a. L. D. Landau, *Zh. Eksp. i Teor. Fiz.,* vol. 20, p. 1064, 1950.

[5]   J. Bardeen, L. N. Cooper, and J. R. Schrieffer, "Microscopic theory of superconductivity," *Physical Review,* vol. 106, no. 1, pp. 162-164, 1957, doi: 10.1103/PhysRev.106.162.

[6]   A. V. Narlikar, SpringerLink, and Link, *High Temperature Superconductivity 2*. Berlin, Heidelberg: Berlin, Heidelberg : Springer Berlin Heidelberg : Imprint: Springer, 2004.

[7]   A. P. Malozemoff *et al.*, "Low-cost YBCO coated conductor technology," *Superconductor Science and Technology,* vol. 13, no. 5, pp. 473-476, 2000/05/01 2000, doi: 10.1088/0953-2048/13/5/308.

[8]   S. Kalsi, *Applications of high temperature superconductors to electric power equipment*. Hoboken, N. J. : Wiley, 2011.

[9]   X. Xuming *et al.*, "High Throughput Processing of Long-Length IBAD MgO and Epi-Buffer Templates at SuperPower," *IEEE Transactions on Applied Superconductivity,* vol. 17, no. 2, pp. 3375-3378, 2007, doi: 10.1109/TASC.2007.899450.

[10]   J. D. Weiss, T. Mulder, H. J. ten Kate, and D. C. van der Laan, "Introduction of CORC®wires: highly flexible, round high-temperature superconducting wires for magnet and power transmission applications," *Superconductor Science and Technology,* vol. 30, no. 1, p. 014002, 2016/11/02 2016, doi: 10.1088/0953-2048/30/1/014002.

[11]   P. Bruzzone *et al.*, "High temperature superconductors for fusion magnets," *Nuclear Fusion,* vol. 58, no. 10, p. 103001, 2018/08/22 2018, doi: 10.1088/1741-4326/aad835.

[12]   D. Zhou, M. Izumi, M. Miki, B. Felder, T. Ida, and M. Kitano, "An overview of rotating machine systems with high-temperature bulk superconductors," vol. 25, ed, 2012, p. 103001.

[13]   Q. Sun, D. Xing, Q. Yang, H. Zhang, and J. Patel, "A New Design of Fuzzy Logic Control for SMES and Battery Hybrid Storage System," *Energy Procedia,* vol. 105, pp. 4575-4580, 2017/05/01/ 2017.

[14]   A. Usoskin, V. V. Rao, R. Dietrich, A. Rutt, and K. Schlenga, "Fault current limiters and fault current switches based on wide HTS tapes: low cryo-consumption, new applications," *IOP Conference Series: Materials Science and Engineering,* vol. 171, p. 012119, 2017/02 2017, doi: 10.1088/1757-899x/171/1/012119.

[15]   Y. Terao, M. Sekino, and H. Ohsaki, "Electromagnetic Design of 10 MW Class Fully Superconducting Wind Turbine Generators," *IEEE Transactions on Applied*

Superconductivity, vol. 22, no. 3, pp. 5201904-5201904, 2012, doi: 10.1109/TASC.2011.2177628.

[16] Z. Huang, M. Zhang, W. Wang, and T. A. Coombs, "Trial Test of a Bulk-Type Fully HTS Synchronous Motor," *IEEE Transactions on Applied Superconductivity,* vol. 24, no. 3, pp. 1-5, 2014, doi: 10.1109/TASC.2013.2296142.

[17] D. Sekiguchi *et al.*, "Trial Test of Fully HTS Induction/Synchronous Machine for Next Generation Electric Vehicle," *IEEE Transactions on Applied Superconductivity,* vol. 22, no. 3, pp. 5200904-5200904, 2012, doi: 10.1109/TASC.2011.2176094.

[18] J. H. Durrell *et al.*, "Atrapped field of 17.6 t in melt-processed, bulk gd-ba-cu-o reinforced with shrink-fit steel," *Superconductor Science and Technology,* vol. 27, no. 8, p. 082001, 2014, doi: 10.1088/0953-2048/27/8/082001.

[19] P. Anup *et al.*, "A trapped field of 17.7 T in a stack of high temperature superconducting tape," *Superconductor Science and Technology,* vol. 31, no. 9, p. 09LT01, 2018.

[20] M. Zhang, F. Eastham, and W. Yuan, "Design and Modeling of 2G HTS Armature Winding for Electric Aircraft Propulsion Applications," *Applied Superconductivity, IEEE Transactions on,* vol. 26, no. 3, pp. 1-5, 2016, doi: 10.1109/TASC.2016.2539548.

[21] J. R. Hull and M. Murakami, "Applications of bulk high-temperature Superconductors," *Proceedings of the IEEE,* vol. 92, no. 10, pp. 1705-1718, 2004, doi: 10.1109/JPROC.2004.833796.

[22] A. A. Golubov, "Handbook of Applied Superconductivity," *IOP Publishing,* vol. 1, no. ch. A1: The evolution of superconducting theories, pp. 3–36, 1998.

[23] C. P. Poole, "Superconductivity 2nd ed.," *Elsevier Ltd,* 2007.

[24] G. F. a. L. Schultz, "Concise Encyclopedia of Magnetic and Superconducting Materials, 2nd ed," *Elsevier Ltd,* no. Superconducting Permanent Magnets: Principles and Results, pp. 1166–1174, 2005.

[25] A. K. Saxena, *High-Temperature Superconductors*, 2nd ed. ed. Berlin, Heidelberg: Berlin, Heidelberg : Springer Berlin Heidelberg : Imprint: Springer, 2012.

[26] D. A. Cardwell, "Processing and properties of large grain (RE)BCO," *Materials Science & Engineering B,* vol. 53, no. 1-2, pp. 1-10, 1998, doi: 10.1016/S0921-5107(97)00293-6.

[27] A. C. Rose-Innes, *Introduction to Superconductivity*, 2 ed. Elsevier Science, 1978.

[28] L. David, G. Alex, D. M. Feldmann, and P. Anatoly, "High-Tc superconducting materials for electric power applications," *Nature,* vol. 414, no. 6861, p. 368, 2001, doi: 10.1038/35104654.

[29] J. Yuan, V. Stanev, C. Gao, I. Takeuchi, and K. Jin, "Recent advances in high-throughput superconductivity research," *Superconductor Science and Technology,* vol. 32, no. 12, p. 123001, 2019/11/13 2019, doi: 10.1088/1361-6668/ab51b1.

[30] D. Larbalestier, A. Gurevich, D. M. Feldmann, and A. Polyanskii, "High-Tc superconducting materials for electric power applications," in *Materials For Sustainable Energy: A Collection of Peer-Reviewed Research and Review Articles from Nature Publishing Group*: World Scientific, 2011, pp. 311-320.

[31] J. Nagamatsu, N. Nakagawa, T. Muranaka, Y. Zenitani, and J. Akimitsu, "Superconductivity at 39 K in magnesium diboride," *nature,* vol. 410, no. 6824, p. 63, 2001.

[32] I. Pallecchi, M. Eisterer, A. Malagoli, and M. Putti, "Application potential of Fe-based superconductors," *Superconductor Science and Technology,* vol. 28, no. 11, p. 114005, 2015/10/07 2015, doi: 10.1088/0953-2048/28/11/114005.

[33] R. Abd-Shukor and F. A. Sc, "High Temperature Superconductors: Materials, Mechanisms and Applications," 2009.

[34] W. Carr Jr, *AC loss and macroscopic theory of superconductors*. CRC Press, 2001.

[35]   C. P. Bean, "Magnetization of hard superconductors," *Physical review letters,* vol. 8, no. 6, p. 250, 1962.

[36]   C. P. Bean, "Magnetization of high-field superconductors," *Reviews of modern physics,* vol. 36, no. 1, p. 31, 1964.

[37]   J. Rhyner, "Magnetic properties and AC-losses of superconductors with power law current-voltage characteristics," *Physica C,* vol. 212, pp. 292–300, 1993.

[38]   S. S. e. al., "Comparison of numerical methods for modeling of superconductors," *IEEE Trans. Mag.,* vol. 38, no. 2, pp. 849–852, March 2002.

[39]   C. F. H. Y. B. Kim, and A. R. Strnad, "Critical persistent currents in hard superconductors," *Phys.Rev. Lett.,* vol. 9, no. 7, pp. 306–309, 1963.

[40]   P. W. Anderson, "Theory of flux creep in hard superconductors," *Phys.Rev. Lett.,* vol. 9, no. 7, pp. 309–311, 1963.

[41]   Q. Jiang, M. Majoros, Z. Hong, A. M. Campbell, and T. A. Coombs, "Design and AC loss analysis of a superconducting synchronous motor," *Superconductor Science and Technology,* vol. 19, no. 11, p. 1164, 2006.

[42]   F. Sirois and F. Grilli, "Potential and limits of numerical modelling for supporting the development of HTS devices," *Superconductor Science and Technology,* vol. 28, no. 4, p. 043002, 2015.

[43]   F. Grilli, F. Sirois, V. M. R. Zermeño, and M. Vojenčiak, "Self-Consistent Modeling of the Ic of HTS Devices: How Accurate do Models Really Need to Be?," *IEEE Transactions on Applied Superconductivity,* vol. 24, no. 6, pp. 1-8, 2014, doi: 10.1109/TASC.2014.2326925.

[44]   F. Grilli, E. Pardo, A. Stenvall, D. N. Nguyen, W. Yuan, and F. Gömöry, "Computation of Losses in HTS Under the Action of Varying Magnetic Fields and Currents," *IEEE Transactions on Applied Superconductivity,* vol. 24, no. 1, pp. 78-110, 2014, doi: 10.1109/TASC.2013.2259827.

[45]   F. Gömöry, J. Šouc, M. Vojenčiak, and B. Klinčok, "Phenomenological description of flux pinning in non-uniform high-temperature superconductors in magnetic fields lower than the self-field," *Superconductor Science and Technology,* vol. 20, no. 9, pp. S271-S277, 2007/08/23 2007, doi: 10.1088/0953-2048/20/9/s23.

[46]   Z. Huiming, "Study of Second Generation High Temperature Superconducting Coils for Energy Storage System," Thesis no. The University of Bath, 2016.

[47]   M. Zhang, "Study of second generation high temperature superconducting coils," no. Department of Engineering, University of Cambridge, July 2013.

[48]   J. K. Sykulski, R. L. Stoll, A. E. Mahdi, and C. P. Please, "Modelling HTc superconductors for AC power loss estimation," *IEEE Transactions on Magnetics,* vol. 33, no. 2, pp. 1568-1571, 1997, doi: 10.1109/20.582565.

[49]   E. Vinot, G. Meunier, and P. Tixador, "Different formulations to model superconductors," *IEEE Transactions on Magnetics,* vol. 36, no. 4, pp. 1226-1229, 2000, doi: 10.1109/20.877661.

[50]   A. M. Campbell, "A new method of determining the critical state in superconductors," *Superconductor Science and Technology,* vol. 20, no. 3, pp. 292-295, 2007, doi: 10.1088/0953-2048/20/3/031.

[51]   H. Zhang, M. Zhang, and W. Yuan, "An efficient 3D finite element method model based on the *T-A* formulation for superconducting coated conductors," *Superconductor Science and Technology,* vol. 30, no. 2, 2017, doi: 10.1088/1361-6668/30/2/024005.

[52]   F. Liang *et al.*, "A finite element model for simulating second generation high temperature superconducting coils/stacks with large number of turns," *Journal of Applied Physics,* vol. 122, no. 4, 2017, doi: 10.1063/1.4995802.

[53] Z. Hong, A. M. Campbell, and T. A. Coombs, "Numerical solution of critical state in superconductivity by finite element software," *Superconductor Science and Technology,* vol. 19, no. 12, pp. 1246-1252, 2006, doi: 10.1088/0953-2048/19/12/004.

[54] Z. Hong, Q. Jiang, R. Pei, A. M. Campbell, and T. A. Coombs, "A numerical method to estimate AC loss in superconducting coated conductors by finite element modelling," *Superconductor Science and Technology,* vol. 20, no. 4, p. 331, 2007.

[55] M. Zhang, J.-H. Kim, S. Pamidi, M. Chudy, W. Yuan, and T. A. Coombs, "Study of second generation, high-temperature superconducting coils: Determination of critical current," *Journal of Applied Physics,* vol. 111, no. 8, 2012, doi: 10.1063/1.3698317.

[56] M. D. Ainslie, T. J. Flack, and A. M. Campbell, "Calculating transport AC losses in stacks of high temperature superconductor coated conductors with magnetic substrates using FEM," *Physica C: Superconductivity,* vol. 472, no. 1, pp. 50-56, 2012/01/01/ 2012, doi: https://doi.org/10.1016/j.physc.2011.10.008.

[57] V. M. R. Zermeno, A. B. Abrahamsen, N. Mijatovic, B. B. Jensen, and M. P. Sørensen, "Calculation of alternating current losses in stacks and coils made of second generation high temperature superconducting tapes for large scale applications," *Journal of Applied Physics,* vol. 114, no. 17, 2013, doi: 10.1063/1.4827375.

[58] A. Stenvall, V. Lahtinen, and M. Lyly, "An h -formulation-based three-dimensional hysteresis loss modelling tool in a simulation including time varying applied field and transport current: the fundamental problem and its solution," *Superconductor Science and Technology,* vol. 27, no. 10, p. 104004, 2014, doi: 10.1088/0953-2048/27/10/104004.

[59] K. Kajikawa, T. Hayashi, R. Yoshida, M. Iwakuma, and K. Funaki, "Numerical evaluation of AC losses in HTS wires with 2D FEM formulated by self magnetic field," *IEEE Transactions on Applied Superconductivity,* vol. 13, no. 2, pp. 3630-3633, 2003, doi: 10.1109/TASC.2003.812415.

[60] S. Zixuan Zhu, S. Yawei Wang, S. Venuturumilli, S. Jie Sheng, S. Min Zhang, and S. Weijia Yuan, "Influence of Harmonic Current on Magnetization Loss of a Triaxial CORC REBCO Cable for Hybrid Electric Aircraft," *Applied Superconductivity, IEEE Transactions on,* vol. 28, no. 4, pp. 1-5, 2018, doi: 10.1109/TASC.2018.2813001.

[61] Z. Zhu, Y. Wang, D. Xing, X. Pei, M. Zhang, and W. Yuan, "Quench of a Single-Layer ReBCO CORC Cable With Non-Uniform Terminal Contact Resistance," *IEEE Transactions on Applied Superconductivity,* vol. 29, no. 5, pp. 1-5, 2019, doi: 10.1109/TASC.2019.2900383.

[62] O. Bíró, "Edge element formulations of eddy current problems," *Computer Methods in Applied Mechanics and Engineering,* vol. 169, no. 3, pp. 391-405, 1999/02/12/ 1999, doi: https://doi.org/10.1016/S0045-7825(98)00165-0.

[63] C. Navau, N. Del-Valle, and A. Sanchez, "Macroscopic Modeling of Magnetization and Levitation of Hard Type-II Superconductors: The Critical-State Model," *IEEE Transactions on Applied Superconductivity,* vol. 23, no. 1, pp. 8201023-8201023, 2013, doi: 10.1109/TASC.2012.2232916.

[64] H. Fujishiro and T. Naito, "Simulation of temperature and magnetic field distribution in superconducting bulk during pulsed field magnetization," *Superconductor Science and Technology,* vol. 23, no. 10, p. 105021, 2010, doi: 10.1088/0953-2048/23/10/105021.

[65] M. D. Ainslie and H. Fujishiro, "Modelling of bulk superconductor magnetization," vol. 28, ed, 2015, p. 053002.

[66] A. Patel, S. C. Hopkins, and B. A. Glowacki, "Trapped fields up to 2 t in a 12 mm square stack of commercial superconducting tape using pulsed field magnetization,"

Superconductor Science and Technology, vol. 26, no. 3, p. 032001, 2013, doi: 10.1088/0953-2048/26/3/032001.

[67]   H. Fujishiro, T. Tateiwa, A. Fujiwara, T. Oka, and H. Hayashi, "Higher trapped field over 5 T on HTSC bulk by modified pulse field magnetizing," *Physica C: Superconductivity and its applications,* vol. 445-448, pp. 334-338, 2006, doi: 10.1016/j.physc.2006.04.077.

[68]   K. Kajikawa *et al.*, "Finite element analysis of pulsed field magnetization process in a cylindrical bulk superconductor," *Physica C: Superconductivity and its applications,* vol. 468, no. 15, pp. 1494-1497, 2008, doi: 10.1016/j.physc.2008.05.062.

[69]   H. Kamijo and H. Fujimoto, "Repeated pulsed-field magnetization with temperature control in a high-Tc bulk superconductor," *Applied Superconductivity, IEEE Transactions on,* vol. 11, no. 1, pp. 1816-1819, 2001, doi: 10.1109/77.920200.

[70]   F. Hiroyuki, T. Tatsuya, and H. Takuya, "Enhancement of Trapped Field and Total Trapped Flux on High Temperature Bulk Superconductor by a New Pulse-Field Magnetization Method," *Japanese Journal of Applied Physics,* vol. 46, no. 7R, p. 4108, 2007.

[71]   H. Fujishiro, T. Hiyama, T. Naito, Y. Yanagi, and Y. Itoh, "Enhancement of trapped field and total trapped flux on gdbacuo bulk by the mmpsc+imra method," *Superconductor Science and Technology,* vol. 22, no. 9, p. 095006, 2009, doi: 10.1088/0953-2048/22/9/095006.

[72]   H. Fujishiro, T. Naito, K. Kakehata, Y. Yanagi, and Y. Itoh, "Estimation of temperature rise from trapped field gradient on superconducting bulk magnetized by multi-pulse technique," *Superconductor Science and Technology,* vol. 23, no. 2, p. 025013, 2010, doi: 10.1088/0953-2048/23/2/025013.

[73]   A. Patel and B. A. Glowacki, "Enhanced trapped field achieved in a superconducting bulk using high thermal conductivity structures following simulated pulsed field magnetization," *Superconductor Science and Technology,* vol. 25, no. 12, p. 125015, 2012.

[74]   M. Sander, U. Sutter, R. Koch, and M. Kläser, "Pulsed magnetization of HTS bulk parts at T <77 K," *Superconductor Science and Technology,* vol. 13, no. 6, p. 841, 2000.

[75]   H. Ikuta, H. Ishihara, Y. Yanagi, Y. Itoh, and U. Mizutani, "Extracting the utmost from the high performance of Sm–Ba–Cu–O bulk superconductors by pulse field magnetization," *Superconductor Science and Technology,* vol. 15, no. 4, pp. 606-612, 2002/03/18 2002, doi: 10.1088/0953-2048/15/4/321.

[76]   T. Ida *et al.*, "Magnetization properties for Gd–Ba–Cu–O bulk superconductors with a couple of pulsed-field vortex-type coils," *Physica C: Superconductivity and its applications,* vol. 412, pp. 638-645, 2004, doi: 10.1016/j.physc.2003.12.082.

[77]   Y. Kimura, "Practical technique of pulsed field magnetization for bulk hts application," *Journal of Physics: Conference Series,* vol. 97, no. 1, p. 012295, 2008, doi: 10.1088/1742-6596/97/1/012295.

[78]   S. Zou, V. M. R. Zermeno, and F. Grilli, "Simulation of Stacks of High-Temperature Superconducting Coated Conductors Magnetized by Pulsed Field Magnetization Using Controlled Magnetic Density Distribution Coils," *Applied Superconductivity, IEEE Transactions on,* vol. 26, no. 3, pp. 1-5, 2016, doi: 10.1109/TASC.2016.2520210.

[79]   H. Fujishiro, T. Naito, and M. Oyama, "Mechanism of magnetic flux trapping on superconducting bulk magnetized by pulsed field using a vortex-type coil," *Superconductor Science and Technology,* vol. 24, no. 7, p. 075015, 2011, doi: 10.1088/0953-2048/24/7/075015.

[80]   K. Yamaguchi, Y. Kimura, M. Izumi, S. Nariki, N. Sakai, and I. Hirabayashi, "Pulsed field magnetization properties for a large single-grain Gd-Ba-Cu-O high-temperature

superconductor bulk with a diameter of 140 mm by using a new type of pulsed copper split coil," *Journal of Physics: Conference Series,* vol. 97, p. 012278, 2008/02/01 2008, doi: 10.1088/1742-6596/97/1/012278.

[81] S. Bræck, D. V. Shantsev, T. H. Johansen, and Y. M. Galperin, "Superconducting trapped-field magnets: Temperature and field distributions during pulsed-field activation," *Journal of Applied Physics,* vol. 92, no. 10, pp. 6235-6240, 2002, doi: 10.1063/1.1515098.

[82] H. Ohsaki, S. Matsumura, S. Kawamoto, and R. Shiraishi, "Numerical simulation of pulsed field magnetisation of cryocooler-cooled bulk superconductor " *AIP Conference Proceedings,* vol. 985, no. 1, pp. 999-1006, 2008, doi: 10.1063/1.2908700.

[83] M. D. Ainslie *et al.*, "Enhanced trapped field performance of bulk high-temperature superconductors using split coil, pulsed field magnetization with an iron yoke," *Superconductor Science and Technology,* vol. 29, no. 7, p. 074003, 2016, doi: 10.1088/0953-2048/29/7/074003.

[84] F. Hiroyuki, O. Tetsuo, Y. Kazuya, and N. Koshichi, "Time evolution and spatial distribution of temperature in YBCO bulk superconductor after pulse field magnetizing," *Superconductor Science and Technology,* vol. 16, no. 7, p. 809, 2003.

[85] T. Masaru and M. Masato, "High-temperature superconductor bulk magnets that can trap magnetic fields of over 17 tesla at 29 K," *Nature,* vol. 421, no. 6922, p. 517, 2003, doi: 10.1038/nature01350.

[86] H. Matsuzaki, "An Axial Gap-Type HTS Bulk Synchronous Motor Excited by Pulsed-Field Magnetization With Vortex-Type Armature Copper Windings," *IEEE Transactions on Applied Superconductivity,* vol. 15, no. 2, pp. 2222-2226, 2005, doi: 10.1109/TASC.2005.849617.

[87] F. Hiroyuki, K. Masahiko, T. Tatsuya, and O. Tetsuo, "Trapped Field over 4 Tesla on GdBaCuO Bulk by Pulse Field Method and Magnetizing Mechanism," *Journal of Physics: Conference Series,* vol. 43, no. 1, p. 405, 2006.

[88] Nkawasaki *et al.*, *Magnetizing technique for permanent magnets by intense static fields generated by HTS bulk magnets: Numerical Analysis.* 2012.

[89] K. Yokoyama, A. Katsuki, A. Miura, and T. Oka, "Comparison of Trapped Field Characteristic of Bulk Magnet System Using Various Type Refrigerators," *Journal of Physics: Conference Series,* vol. 1054, p. 012072, 2018/07 2018, doi: 10.1088/1742-6596/1054/1/012072.

[90] H. Fujishiro *et al.*, "Simulation studies of mechanical stresses in REBaCuO superconducting ring bulks with infinite and finite height reinforced by metal ring during field-cooled magnetization," *Superconductor Science and Technology,* vol. 30, no. 8, p. 085008, 2017/07/07 2017, doi: 10.1088/1361-6668/aa76a2.

[91] S. Fukada, S. B. Kim, T. Nakagawa, R. Nomura, and H. Ueda, "Numerical study to obtain the improved field homogeneity of HTS bulk magnet with enlarged inner diameter for compact NMR," *Journal of Physics: Conference Series,* vol. 871, p. 012088, 2017/07 2017, doi: 10.1088/1742-6596/871/1/012088.

[92] S. Nariki, N. Sakai, and M. Murakami, "Melt-processed Gd–Ba–Cu–O superconductor with trapped field of 3 T at 77 K," *Superconductor Science and Technology,* vol. 18, no. 2, p. S126, 2005.

[93] S. Gruss *et al.*, "Superconducting bulk magnets: Very high trapped fields and cracking," *APPLIED PHYSICS LETTERS,* vol. 79, no. 19, 2001.

[94] L. Dominic and S. Kamel, "Enhancements in Current Density and Mechanical Properties of Y-Ba-Cu-O/Ag Composites," *Japanese Journal of Applied Physics,* vol. 29, no. 11A, p. L2017, 1990.

[95] A. Patel, S. Hahn, J. Voccio, A. Baskys, S. C. Hopkins, and B. A. Glowacki, "Magnetic levitation using a stack of high temperature superconducting tape annuli," *Superconductor Science and Technology,* vol. 30, no. 2, p. 024007, 2017.

[96] A. G. Page *et al.*, "The effect of stabilizer on the trapped field of stacks of superconducting tape magnetized by a pulsed field," *Superconductor Science and Technology,* vol. 28, no. 8, p. 085009, 2015, doi: 10.1088/0953-2048/28/8/085009.

[97] V. Climente-Alarcon, A. Patel, A. Baskys, and B. A. Glowacki, "Design considerations for electric motors using stacks of high temperature superconducting tape as permanent magnets," *IOP Conference Series: Materials Science and Engineering,* vol. 502, p. 012182, 2019/04/15 2019, doi: 10.1088/1757-899x/502/1/012182.

[98] B. B. Jensen, N. Mijatovic, and A. B. Abrahamsen, "Development of superconducting wind turbine generators," *Journal of Renewable and Sustainable Energy,* vol. 5, no. 2, p. 023137, 2013, doi: 10.1063/1.4801449.

[99] S. S. Kalsi, B. B. Gamble, G. Snitchler, and S. O. Ige, "The status of HTS ship propulsion motor developments," in *2006 IEEE Power Engineering Society General Meeting*, 18-22 June 2006 2006, p. 5 pp., doi: 10.1109/PES.2006.1709643.

[100] S. S. Kalsi, *Applications of high temperature superconductors to electric power equipment*. John Wiley & Sons, 2011.

[101] Y. Itoh *et al.*, "A construction of high temperature superconducting motor using YBCO bulk magnets," *Physica C: Superconductivity,* vol. 235-240, pp. 3445-3446, 1994/12/01/ 1994, doi: https://doi.org/10.1016/0921-4534(94)91249-1.

[102] Y. Itoh *et al.*, "High-Temperature Superconducting Motor Using Y-Ba-Cu-O Bulk Magnets," *Japanese Journal of Applied Physics,* vol. 34, no. Part 1, No. 10, pp. 5574-5578, 1995/10/15 1995, doi: 10.1143/jjap.34.5574.

[103] Q. Jiang, M. Majoros, Z. Hong, A. M. Campbell, and T. A. Coombs, "Design and AC loss analysis of a superconducting synchronous motor," *Superconductor Science and Technology,* vol. 19, no. 11, pp. 1164-1168, 2006/10/04 2006, doi: 10.1088/0953-2048/19/11/012.

[104] M. Miki *et al.*, "Development of a synchronous motor with Gd–Ba–Cu–O bulk superconductors as pole-field magnets for propulsion system," *Superconductor Science and Technology,* vol. 19, no. 7, pp. S494-S499, 2006/04/21 2006, doi: 10.1088/0953-2048/19/7/s14.

[105] Y. Jiang, R. Pei, Z. Hong, J. Song, F. Fang, and T. A. Coombs, "Design and control of a superconducting permanent magnet synchronous motor," *Superconductor Science and Technology,* vol. 20, no. 7, pp. 585-591, 2007/05/23 2007, doi: 10.1088/0953-2048/20/7/001.

[106] H. Sugimoto *et al.*, "Development and test of an axial flux type PM synchronous motor with liquid nitrogen cooled HTS armature windings," *Journal of Physics: Conference Series,* vol. 97, p. 012203, 2008/02/01 2008, doi: 10.1088/1742-6596/97/1/012203.

[107] W. Xian, W. Yuan, and T. A. Coombs, "Numerical assessment of efficiency and control stability of an HTS synchronous motor," *Journal of Physics: Conference Series,* vol. 234, no. 3, p. 032063, 2010/06/01 2010, doi: 10.1088/1742-6596/234/3/032063.

[108] W. Xian, Y. Yan, W. Yuan, R. Pei, and T. A. Coombs, "Pulsed Field Magnetization of a High Temperature Superconducting Motor," *IEEE Transactions on Applied Superconductivity,* vol. 21, no. 3, pp. 1171-1174, 2011, doi: 10.1109/TASC.2010.2092745.

[109] Z. Huang *et al.*, "Control and Operation of a High Temperature Superconducting Synchronous Motor," *IEEE Transactions on Applied Superconductivity,* vol. 23, no. 3, pp. 5200204-5200204, 2013, doi: 10.1109/TASC.2012.2233262.

[110] T. Qu *et al.*, "Development and testing of a 2.5 kW synchronous generator with a high temperature superconducting stator and permanent magnet rotor," *Superconductor Science and Technology,* vol. 27, no. 4, p. 044026, 2014/03/18 2014, doi: 10.1088/0953-2048/27/4/044026.

[111] P. Song, T. M. Qu, L. F. Lai, M. S. Wu, X. Y. Yu, and Z. Han, "Thermal analysis for the HTS stator consisting of HTS armature windings and an iron core for a 2.5 kW HTS generator," *Superconductor Science and Technology,* vol. 29, no. 5, p. 054007, 2016/03/18 2016, doi: 10.1088/0953-2048/29/5/054007.

[112] B. Dolisy, S. Mezani, T. Lubin, and J. Lévêque, "Fabrication and test of an axial-field HTS rotating machine with integrated magnetic coupling," *Superconductor Science and Technology,* vol. 30, no. 3, p. 035015, 2017/02/01 2017, doi: 10.1088/1361-6668/aa5295.

[113] M. Saruwatari *et al.*, "Design Study of 15-MW Fully Superconducting Generators for Offshore Wind Turbine," *IEEE Transactions on Applied Superconductivity,* vol. 26, no. 4, pp. 1-5, 2016, doi: 10.1109/TASC.2016.2535315.

[114] F. Lin, R. Qu, and D. Li, "A Novel Fully Superconducting Geared Machine," *IEEE Transactions on Applied Superconductivity,* vol. 26, no. 7, pp. 1-5, 2016, doi: 10.1109/TASC.2016.2594872.

[115] M. Hirakawa, S. Inadama, K. Kikukawa, E. Suzuki, and H. Nakasima, "Developments of superconducting motor with YBCO bulk magnets," *Physica C: Superconductivity,* vol. 392-396, pp. 773-776, 2003/10/01/ 2003, doi: https://doi.org/10.1016/S0921-4534(03)01213-9.

[116] S. P. Ashworth and F. Grilli, "A strategy for the reduction of ac losses in YBCO coated conductors," *Superconductor Science and Technology,* vol. 19, no. 2, pp. 227-232, 2006/01/17 2006, doi: 10.1088/0953-2048/19/2/013.

[117] D. N. Nguyen, S. P. Ashworth, and J. O. Willis, "Experimental and finite-element method studies of the effects of ferromagnetic substrate on the total ac loss in a rolling-assisted biaxially textured substrate YBa 2 Cu 3 O 7 tape exposed to a parallel ac magnetic field," *Journal of Applied Physics,* vol. 106, no. 9, 2009, doi: 10.1063/1.3255998.

[118] E. H. Brandt and M. Indenbom, "Type-II-superconductor strip with current in a perpendicular magnetic field," *Physical Review, B: Condensed Matter,* vol. 48, no. 17, 1993, doi: 10.1103/PhysRevB.48.12893.

[119] N. Amemiya, T. Tsukamoto, M. Nii, T. Komeda, T. Nakamura, and Z. Jiang, "Alternating current loss characteristics of a roebel cable consisting of coated conductors and a three-dimensional structure," *Superconductor Science and Technology,* vol. 27, no. 3, p. 035007, 2014, doi: 10.1088/0953-2048/27/3/035007.

[120] Z. Jiang, M. Staines, R. A. Badcock, N. J. Long, and N. Amemiya, "Transport ac loss measurement of a five strand ybco roebel cable," *Superconductor Science and Technology,* vol. 22, no. 9, p. 095002, 2009, doi: 10.1088/0953-2048/22/9/095002.

[121] S. Terzieva *et al.*, "Investigation of the effect of striated strands on the ac losses of 2g roebel cables," *Superconductor Science and Technology,* vol. 24, no. 4, p. 045001, 2011, doi: 10.1088/0953-2048/24/4/045001.

[122] M. Takayasu, L. Chiesa, L. Bromberg, and J. V. Minervini, "HTS twisted stacked-tape cable conductor," *Superconductor Science and Technology,* vol. 25, no. 1, p. 014011, 2011/12/02 2011, doi: 10.1088/0953-2048/25/1/014011.

[123] D. Uglietti, "A review of commercial high temperature superconducting materials for large magnets: from wires and tapes to cables and conductors," *Superconductor Science and Technology,* vol. 32, no. 5, p. 053001, 2019/04/09 2019, doi: 10.1088/1361-6668/ab06a2.

[124] N. Amemiya, F. Kimura, and T. Ito, "Total AC Loss in Twisted Multifilamentary Coated Conductors Carrying AC Transport Current in AC Transverse Magnetic Field," *IEEE Transactions on Applied Superconductivity,* vol. 17, no. 2, pp. 3183-3186, 2007, doi: 10.1109/TASC.2007.899577.

[125] M. Ainslie, "Transport AC loss in high temperature superconducting coils" King's College University of Cambridge, 2012.

[126] S. Zou, V. M. R. Zermeno, A. Baskys, A. Patel, F. Grilli, and B. A. Glowacki, "Simulation and experiments of stacks of high temperature superconducting coated conductors magnetized by pulsed field magnetization with multi-pulse technique," *Superconductor Science and Technology,* vol. 30, no. 1, 2017, doi: 10.1088/0953-2048/30/1/014010.

[127] F. Grilli, "Finite-Element Method Modeling of Superconductors: From 2-D to 3-D," *IEEE Transactions on Applied Superconductivity,* vol. 15, no. 1, pp. 17-26, 2005, doi: 10.1109/TASC.2004.839774.

[128] F. Grilli, S. P. Ashworth, and L. Civale, "Interaction of magnetic field and magnetic history in high-temperature superconductors," *Journal of Applied Physics,* vol. 102, no. 7, 2007, doi: 10.1063/1.2785959.

[129] F. Roy, B. Dutoit, F. Grilli, and F. Sirois, "Magneto-thermal modeling of second-generation HTS for resistive fault current limiter design purposes," *IEEE Transactions on Applied Superconductivity,* vol. 18, no. 1, pp. 29-35, 2008.

[130] W. Chan, P. J. Masson, C. A. Luongo, and J. Schwartz, "Influence of Inter-Layer Contact Resistances on Quench Propagation in YBa2Cu3Ox Coated Conductors," *IEEE Transactions on Applied Superconductivity,* vol. 19, no. 3, pp. 2490-2495, 2009, doi: 10.1109/TASC.2009.2018514.

[131] F. Liang, W. Yuan, C. A. Baldan, M. Zhang, and J. S. Lamas, "Modeling and Experiment of the Current Limiting Performance of a Resistive Superconducting Fault Current Limiter in the Experimental System," *J. Supercond. Nov. Magn,* vol. 28, no. 9, pp. 2669-2681, 2015/09/01 2015, doi: 10.1007/s10948-015-3102-x.

[132] S. C. Wimbush and N. M. Strickland, "A Public Database of High-Temperature Superconductor Critical Current Data," *IEEE Transactions on Applied Superconductivity,* vol. 27, no. 4, pp. 1-5, 2017, doi: 10.1109/TASC.2016.2628700.

[133] N. M. Strickland, C. Hoffmann, and S. C. Wimbush, "A 1 kA-class cryogen-free critical current characterization system for superconducting coated conductors," *Review of Scientific Instruments,* vol. 85, no. 11, 2014, doi: 10.1063/1.4902139.

[134] Y. Wang, J. Zheng, Z. Zhu, M. Zhang, and W. Yuan, "Quench behavior of high temperature superconductor (RE) Ba 2 Cu 3 O x CORC cable," *Journal of Physics D: Applied Physics,* 2019.

[135] A. Alvarez, P. Suarez, B. Perez, and L. Garcia, "Coated Superconducting Tape Model Based on the Distribution of Currents Between the Tape Layers: Computing Implementation," *IEEE Transactions on Applied Superconductivity,* vol. 28, no. 4, pp. 1-5, 2018, doi: 10.1109/TASC.2018.2797178.

[136] S. Zou, V. M. R. Zermeno, and F. Grilli, "Influence of Parameters on the Simulation of HTS Bulks Magnetized by Pulsed Field Magnetization," *Applied Superconductivity, IEEE Transactions on,* vol. 26, no. 4, pp. 1-5, 2016, doi: 10.1109/TASC.2016.2535379.

[137] A. Patel and B. A. Glowacki, "Optimisation of composite superconducting bulks made from (RE)BCO coated conductor stacks using pulsed field magnetization modelling," *Journal of Physics: Conference Series,* vol. 507, no. 2, p. 022024, 2014.

[138] S. Zou, V. M. Zermeño, and F. Grilli, "Influence of parameters on the simulation of HTS bulks magnetized by pulsed field magnetization," *IEEE Transactions on Applied Superconductivity,* vol. 26, no. 4, pp. 1-5, 2016.

[139] D. Xing, "AC Loss Comparison Between Multifilament and Nonstriated YBCO Coils Designed for HTS Propulsion Motors," *IEEE Transactions on Applied Superconductivity,* vol. 27, no. 4, Part 2, pp. 1-6, 2017, doi: 10.1109/TASC.2017.2669156.

[140] M. Zhang, K. Matsuda, and T. A. Coombs, "New application of temperature-dependent modelling of high temperature superconductors: Quench propagation and pulse magnetization," *Journal of Applied Physics,* vol. 112, no. 4, p. 043912, 2012, doi: 10.1063/1.4747925.

[141] J. Duron, F. Grilli, B. Dutoit, and S. Stavrev, "Modelling the E–J relation of high-Tc superconductors in an arbitrary current range," *Physica C: Superconductivity,* vol. 401, no. 1, pp. 231-235, 2004/01/15/ 2004, doi: https://doi.org/10.1016/j.physc.2003.09.044.

[142] U. Gaitzsch *et al.*, "Highly alloyed Ni–W substrates for low AC loss applications," *Superconductor Science and Technology,* vol. 26, no. 8, p. 085024, 2013/07/11 2013, doi: 10.1088/0953-2048/26/8/085024.

[143] F. Grilli, S. P. Ashworth, and L. Civale, "Interaction of magnetic field and magnetic history in high-temperature superconductors," *Journal of Applied Physics,* vol. 102, no. 7, p. 073909, 2007, doi: 10.1063/1.2785959.

[144] A. Baskys, K. Filar, A. Patel, and B. Glowacki, "A trapped field of 13.4 T in a stack of HTS tapes with 30 \mu m substrate," 2017.

[145] T. B. Mitchell-Williams *et al.*, "Uniform trapped fields produced by stacks of HTS coated conductor tape," *Superconductor Science and Technology,* vol. 29, no. 8, p. 085008, 2016.

[146] A. Baskys, A. Patel, S. C. Hopkins, and B. A. Glowacki, "Modeling of Trapped Fields by Stacked (RE)BCO Tape Using Angular Transversal Field Dependence," *Applied Superconductivity, IEEE Transactions on,* vol. 26, no. 3, pp. 1-4, 2016, doi: 10.1109/TASC.2016.2528992.

[147] K. Selva, L. Xiao-Fen, and G. Majkic, "Trapped Field and Flux Creep in Stacked (Gd,Y) \hbox\hbox\hbox Superconductor Tape Arrays," *IEEE Transactions on Applied Superconductivity,* vol. 25, no. 3, pp. 1-5, 2015, doi: 10.1109/TASC.2014.2367159.

[148] I. Rudnev, D. Abin, M. Osipov, S. Pokrovskiy, Y. Ermolaev, and N. Mineev, "Magnetic Properties of the Stack of HTSC Tapes in a Wide Temperature Range," *Physics Procedia,* vol. 65, pp. 141-144, 2015/01/01/ 2015, doi: https://doi.org/10.1016/j.phpro.2015.05.086.

[149] A. Patel, A. Usoskin, A. Baskys, S. C. Hopkins, and B. A. Glowacki, "Trapped Field Profiles for 40-mm Wide Superconducting Tape Pieces," *J. Supercond. Nov. Magn,* vol. 28, no. 2, pp. 397-401, 2015// 2015, doi: 10.1007/s10948-014-2665-2.

[150] A. Patel, A. Baskys, S. C. Hopkins, V. Kalitka, A. Molodyk, and B. A. Glowacki, "Pulsed-field magnetization of superconducting tape stacks for motor applications," *IEEE Transactions on Applied Superconductivity,* vol. 25, no. 3, 2015, doi: 10.1109/TASC.2015.2389142.

[151] A. Baskys, A. Patel, S. C. Hopkins, V. Kalitka, A. Molodyk, and B. A. Glowacki, "Self-Supporting Stacks of Commercial Superconducting Tape Trapping Fields up to 1.6 T Using Pulsed Field Magnetization," *Applied Superconductivity, IEEE Transactions on,* vol. 25, no. 3, pp. 1-4, 2015, doi: 10.1109/TASC.2014.2360871.

[152] H. Maeda and Y. Yanagisawa, "Recent Developments in High-Temperature Superconducting Magnet Technology (Review)," *Applied Superconductivity, IEEE Transactions on,* vol. 24, no. 3, pp. 1-12, 2014, doi: 10.1109/TASC.2013.2287707.

[153] A. Patel, K. Filar, V. I. Nizhankovskii, S. C. Hopkins, and B. A. Glowacki, "Trapped fields greater than 7 T in a 12 mm square stack of commercial high-temperature superconducting tape," *Applied Physics Letters,* vol. 102, no. 10, 2013, doi: 10.1063/1.4795016.

[154] S. Kavita and M. Goran, "Trapped magnetic field profiles of arrays of (Gd,Y)Ba 2 Cu 3 O x superconductor tape in different stacking configurations," *Superconductor Science and Technology,* vol. 26, no. 11, p. 115006, 2013.

[155] S. Kavita, L. Xiao-Fen, M. Goran, and M. Philippe, "Assessment of critical factors affecting the performance of trapped field magnets using thin film superconductor tapes," *IOP Conference Series: Materials Science and Engineering,* vol. 102, no. 1, p. 012031, 2015.

[156] T. B. Mitchell-Williams *et al.*, "Toward Uniform Trapped Field Magnets Using a Stack of Roebel Cable Offcuts," *IEEE Transactions on Applied Superconductivity,* vol. 26, no. 3, pp. 1-4, 2016, doi: 10.1109/TASC.2016.2518994.

[157] N. Cheggour, J. Ekin, Y.-Y. Xie, V. Selvamanickam, C. Thieme, and D. Verebelyi, "Enhancement of the irreversible axial-strain limit of Y-Ba-Cu-O-coated conductors with the addition of a Cu layer," *Applied Physics Letters,* vol. 87, no. 21, p. 212505, 2005.

[158] A. R. Difan Zhou *et al.*, "Full Magnetization of Bulk (RE)Ba2Cu3O7−δ Magnets With Various Rare-Earth Elements Using Pulsed Fields at 77 K," *Applied Superconductivity, IEEE Transactions on,* vol. 27, no. 4, pp. 1-4, 2017, doi: 10.1109/TASC.2016.2638200.

[159] E. Demencik *et al.*, "AC Loss and Coupling Currents in YBCO Coated Conductors With Varying Number of Filaments," *Applied Superconductivity, IEEE Transactions on,* vol. 24, no. 6, pp. 1-8, 2014, doi: 10.1109/TASC.2014.2338320.

[160] M. Majoros, B. A. Glowacki, A. M. Campbell, G. A. Levin, P. N. Barnes, and M. Polak, "AC losses in striated YBCO coated conductors," *Applied Superconductivity, IEEE Transactions on,* vol. 15, no. 2, pp. 2819-2822, 2005, doi: 10.1109/TASC.2005.848234.

[161] M. Polak *et al.*, "Coupling losses and transverse resistivity of multifilament YBCO coated superconductors," *Journal of Physics: Conference Series,* vol. 43, no. 1, p. 591, 2006.

[162] O. Tsukamoto and M. Ciszek, "Ac magnetization losses in striated ybco-123/hastelloy coated conductors," *Superconductor Science and Technology,* vol. 20, no. 10, pp. 974-979, 2007, doi: 10.1088/0953-2048/20/10/014.

[163] T. Uno, T. Ojima, S. Mitsui, T. Takao, and O. Tsukamoto, "AC Magnetization Losses in Copper-Stabilized YBCO Coated Conductors Subjected to Repeated Mechanical Stresses," *Applied Superconductivity, IEEE Transactions on,* vol. 21, no. 3, pp. 3257-3260, 2011, doi: 10.1109/TASC.2010.2089593.

[164] G. A. Levin, J. Murphy, T. J. Haugan, J. Scouc, J. Kovac, and P. Kovac, "AC Losses of Copper Stabilized Multifilament YBCO Coated Conductors," *Applied Superconductivity, IEEE Transactions on,* vol. 23, no. 3, pp. 6600604-6600604, 2013, doi: 10.1109/TASC.2012.2232337.

[165] J. Šouc *et al.*, "Low ac loss cable produced from transposed striated cc tapes," *Superconductor Science and Technology,* vol. 26, no. 7, p. 075020, 2013, doi: 10.1088/0953-2048/26/7/075020.

[166] R. Nast *et al.*, "Influence of laser striations on the properties of coated conductors," *Journal of Physics: Conference Series,* vol. 507, no. 2, p. 022023, 2014, doi: 10.1088/1742-6596/507/2/022023.

[167] E. Demencik *et al.*, "AC magnetization loss and transverse resistivity of striated YBCO coated conductors," *IEEE Transactions on Applied Superconductivity,* vol. 25, no. 3, 2015, doi: 10.1109/TASC.2014.2381561.

[168]   M. Vojenčiak *et al.*, "Magnetization ac loss reduction in HTS CORC®cables made of striated coated conductors," *Superconductor Science and Technology,* vol. 28, no. 10, p. 104006, 2015, doi: 10.1088/0953-2048/28/10/104006.

[169]   M. Wang *et al.*, "An effective way to reduce AC loss of second-generation high temperature superconductors," *Superconductor Science and Technology,* vol. 32, no. 1, p. 01LT01, 2018/11/16 2018, doi: 10.1088/1361-6668/aaee05.

[170]   Y. Nikulshin, Y. Yeshurun, and S. Wolfus, "Effect of magnetic sheath on filament AC losses and current distribution in MgB2 superconducting wires: numerical analysis," *Superconductor Science and Technology,* vol. 32, no. 7, p. 075007, 2019/06/06 2019, doi: 10.1088/1361-6668/ab13d9.

[171]   M. Osipov *et al.*, "Investigation of the hysteresis losses in CC tapes after laser filamentation," *Journal of Physics: Conference Series,* vol. 747, p. 012044, 2016/09 2016, doi: 10.1088/1742-6596/747/1/012044.

[172]   G. Francesco and K. Anna, "How filaments can reduce AC losses in HTS coated conductors: a review," *Superconductor Science and Technology,* vol. 29, no. 8, p. 083002, 2016.

[173]   X. Cai, I. Kesgin, and V. Selvamanickam, "Reel-to-Reel Selective Electroplating of Cu Stabilizer for Multifilamentary Coated Conductors," *IEEE Transactions on Applied Superconductivity,* vol. 25, no. 3, pp. 1-4, 2015, doi: 10.1109/TASC.2014.2369964.

[174]   M. Polak, J. Kvitkovic, P. Mozola, P. N. Barnes, and G. A. Levin, "Characterization of Individual Filaments in a Multifilamentary YBCO Coated Conductor," *Applied Superconductivity, IEEE Transactions on,* vol. 17, no. 2, pp. 3163-3166, 2007, doi: 10.1109/TASC.2007.898266.

[175]   M. Majoros, "Transport ac losses in striated ybco coated conductors," *Journal of Physics: Conference Series,* vol. 43, no. 1, pp. 564-567, 2006, doi: 10.1088/1742-6596/43/1/139.

[176]   M. Majoros, M. D. Sumption, and E. W. Collings, "Transport AC Loss Reduction in Striated YBCO Coated Conductors by Magnetic Screening," *Applied Superconductivity, IEEE Transactions on,* vol. 19, no. 3, pp. 3352-3355, 2009, doi: 10.1109/TASC.2009.2019583.

[177]   D. Xing *et al.*, "AC Loss Comparison Between Multifilament and Nonstriated YBCO Coils Designed for HTS Propulsion Motors," *IEEE Transactions on Applied Superconductivity,* vol. 27, no. 4, pp. 1-5, 2017, doi: 10.1109/TASC.2017.2669156.

[178]   B. S. Kim, W. Zhou, Y. D. Shah, C. Zhou, N. Işık, and M. Grayson, "Generalized four-point characterization method using capacitive and ohmic contacts," *Review of Scientific Instruments,* vol. 83, no. 2, p. 024703, 2012, doi: 10.1063/1.3677331.

[179]   Z. Jiahui, Z. Zhenyu, Z. Huiming, Z. Min, Q. Ming, and Y. Weijia, "Electric Measurement of the Critical Current, AC Loss, and Current Distribution of a Prototype HTS Cable," *Applied Superconductivity, IEEE Transactions on,* vol. 24, no. 3, pp. 1-4, 2014, doi: 10.1109/TASC.2013.2284295.

[180]   M. Zhang, J. Kvitkovic, J.-H. Kim, C. H. Kim, S. V. Pamidi, and T. A. Coombs, "Alternating current loss of second-generation high-temperature superconducting coils with magnetic and non-magnetic substrate," *Applied Physics Letters,* vol. 101, no. 10, p. 102602, 2012, doi: 10.1063/1.4749275.

[181]   L. Ji-Kwang *et al.*, "Reduction Effect on Magnetization Loss in the Stacked Conductor With Striated and Transposed YBCC Coated Conductor," *Applied Superconductivity, IEEE Transactions on,* vol. 19, no. 3, pp. 3340-3343, 2009, doi: 10.1109/TASC.2009.2017845.